Forming of deep-parts in AA5383 alloy : experimental and numerical approach

Rou Du

École doctorale n° 432 : Sciences des Métiers de l'ingénieur

Doctorat

T H È S E

pour obtenir le grade de docteur délivré par

l'École Nationale Supérieure d'Arts et Métiers

Spécialité " Mécanique-Procédés de fabrication "

présentée et soutenue publiquement par

Rou DU

Le 27 Septembre 2019

Forming of deep-parts in AA5383 alloy: Experimental and numerical approach

Directeur de thèse : **Philippe DAL SANTO**
Co-encadrement de la thèse : **Charles MAREAU, Yessine AYED**

Jury
Mme Anne Marie HABRAKEN, Directrice de recherches FNRS, ArGEnCo, Université de Liège   Président
Mme Sandrine THUILLIER, Professeur des Universités, IRDL, Université Bretagne Sud   Rapporteur
M. Abel CHEROUAT, Professeur des Universités, Institut Charles Delaunay, U.T. de Troyes   Rapporteur
M. Arnaud DELAMEZIERE, Professeur de Institut Supérieur d'Ingénierie de la Conception, LEM3   Examinateur
M. Yessine AYED, Maître de conférences, LAMPA, ENSAM Angers   Examinateur
M. Charles MAREAU, Maître de conférences, LAMPA, ENSAM Angers   Examinateur
M. Philippe DAL SANTO, Professeur des Universités, LAMPA, ENSAM Angers   Examinateur
Mme Eliane GIRAUD, Maître de Conférences   Invité

T
H
È
S
E

Arts et Métiers ParisTech – Campus d'Angers
Laboratoire Angevin de Mécanique, Procédés et innovAtion (LAMPA)

ACKNOWLEDGEMENTS

Content List

List of Figures

List of Tables

List of notations

Symbols	Description	Units
α	Parameter of the Arrhenius model	[-]
β	Parameter of the Arrhenius model	[-]
$\hat{\beta}$	Parameter of the composite model	[-]
$\dot{\gamma}$ or $\Delta\gamma$	Plastic multiplier	[-]
$\boldsymbol{\varepsilon}$	Total strain tensor	[-]
$\boldsymbol{\varepsilon}^e$	Elastic strain tensor	[-]
$\boldsymbol{\varepsilon}^P$	Plastic strain tensor	[-]
ε	Logarithmic strain	[-]
$\overline{\varepsilon}^P$	Equivalent plastic strain	[-]
$\overline{\varepsilon}_f^P$	Equivalent fracture strain	[-]
$\dot{\overline{\varepsilon}}^P$	Equivalent plastic strain rate	[s^{-1}]
$\dot{\boldsymbol{\varepsilon}}^{'}$	Plastic strain rate tensor	[s^{-1}]
η	Stress triaxiality	[-]
θ	Lode angle	[°]
$\overline{\theta}$	Lode angle parameter	[-]
λ , μ	*Lamé*'s first and second parameter	[Pa]
ν	Poisson's ratio	[-]
ξ	Normalized third stress invariant	[-]
ρ	Dislocation density	[-]
$\boldsymbol{\sigma}$	Stress tensor	[MPa]
σ	Axial Cauchy stress	[MPa]
$\overline{\sigma}$	Equivalent stress	[MPa]
σ_m	Mean stress	[MPa]
$\boldsymbol{\sigma}^{'}$	Effective stress tensor	[MPa]
σ_n	Normal stress	[MPa]
τ	Shear stress	[MPa]
ϕ	Plastic flow potential	[-]
Φ	Yield function	[-]
$\mathbb{C}$	Elastic stiffness tensor	[1/MPa]
a	Parameter of the BBC2003 yield criterion	[-]
$\hat{A}$	Parameter of the Arrhenius model	[-]

A	Parameter of the modified Mohr-Coulomb criterion	[MPa]
$\hat{b}$	Burger's vector	[-]
b	Parameter of the composite model	[-]
C_C	Critical value for ductile fracture criteria	[-]
c_1, c_2, c_3	Parameters of the modified Mohr-Coulomb criterion	[-]
D	Damage state variable	[-]
$\dot{D}$	Damage evolution	[s^{-1}]
D_1, D_2	Parameters of the modified Mohr-Coulomb criterion	[-]
E	Young's modulus	[GPa]
F	Parameter of the Hill48 yield criterion	[-]
F_D	Damage dissipative potential	[-]
G	Parameter of the Hill48 yield criterion	[-]
H	Parameter of the Hill48 yield criterion	[-]
J_3	Third deviatoric stress invariant	[MPa]
k	Integer parameter of the BBC2003 yield criterion	[-]
K	Parameter of the composite model	[MPa]
L	Parameter of the Hill48 yield criterion	[-]
m	Parameter of the composite model	[-]
$\hat{M}$	Parameter of the Hill48 yield criterion	[-]
M	Parameter of the BBC2003 yield criterion	[-]
n	Parameter of the Arrhenius model	[-]
$\hat{n}$	Parameter of the composite model	[-]
n'	Parameter of the modified Mohr-Coulomb criterion	[-]
$\boldsymbol{n}$	Flow direction	[-]
$\hat{N}$	Parameter of the Hill48 yield criterion	[-]
N	Parameter of the BBC2003 yield criterion	[-]
p	Hydrostatic pressure	[MPa]
P	Parameter of the BBC2003 yield criterion	[-]
$\hat{P}$	Forming pressure	[MPa]
$\hat{Q}$	Activation energy	[kJ mol^{-1}]
Q	Parameter of the BBC2003 yield criterion	[-]
r_0, r_{45}, r_{90}	Lankford coefficient	[-]
r_b	Biaxial r-value	[-]
R	Universal gas constant	[kJ mol^{-1} K^{-1}]

$\hat{R}$	Parameter of the BBC2003 yield criterion	[-]
S	Parameter of the BBC2003 yield criterion	[-]
T	Testing temperature	[K]
$\hat{T}$	Parameter of the BBC2003 yield criterion	[-]
T_{ref}	Reference temperature	[K]
T_m	Melting temperature	[-]
$Y, Y_0, Y_{45}, Y_{90}, Y_b$	Yield stress	[MPa]
Z	Zener-Hollomon Parameter	[-]
Z'	Modified Zener-Hollomon Parameter	[-]

Chapter I.   General introduction

I.1 Background and motivation

Due to the concerns of environmental protection and stringent requirements of greenhouse gas emissions, weight reduction is a major issue for transportation. Application of lightweight material, such as aluminum, magnesium alloys or composites is an efficient strategy that can help to meet the climate challenge. Among the family of lightweight material, aluminum alloys have been extensively used in the automotive and aircraft industry due to the advantages of low density, high strength to weight ratio, good corrosion resistance and a reasonably low cost [1].

(a)   (b)

Figure I-1 Example of a deep-drawing part in aluminum alloys for (a) aeronautic and (b) automotive application

Major challenge of application of aluminum alloys in automotive and aeronautic industries lies in the ability to form deep-drawing shapes, as illustrated in Figure I-1. Superplastic Forming (SPF) is widely used to produce this type of parts as shown in Figure I-2 [2-6]. SPF consists in applying, on a flange, a gas pressure at a predefined strain rate to realize the deformed shape [7]. Amongst the advantages of such process are: functions integration, high formability and surface quality. The most critical issue of this process is the inherent high forming time due to the applying of low strain rates to avoid void growth and premature failure.
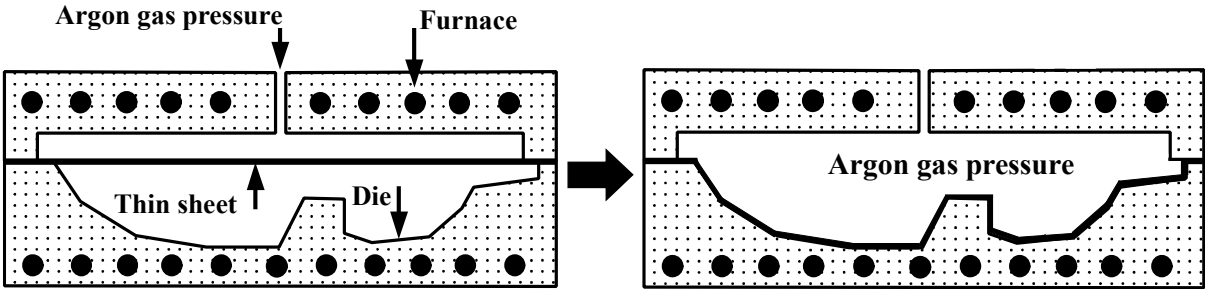
Figure I-2 Principle of Superplastic Forming (SPF) [7]

I.2 Thesis objective

The present dissertation focuses on hot forming strategies to produce deep drawing parts from AA5XXX aluminum thin sheets. The main objective is to reduce the forming time without sacrificing the part integrity. Different approaches can be considered:

- A modification of the alloy characteristics to extend its superplastic field range in terms of temperature and strain rate.
- A pre-deformation of the sheet using hot stamping process before the superplastic operation.
- The use of another forming technique like incremental sheet forming.

The first approach lies in the modification (i.e. the refining) of the granular structure of the alloy before the forming. Decrease in grain size eases superplastic deformation which can thus be activated for lower temperatures and higher strain rates. These new thermomechanical conditions allow decreasing significantly the forming time. Constrained Groove Pressing, a severe plastic deformation technique for the thin sheet, has been recently developed to refine the initial microstructure [8]. The second approach consists in chaining two processes [9, 10], shown in Figure I-3. A first hot deep-drawing operation allows obtaining a preformed geometry with low curvature. This operation is then followed by a superplastic operation which completes the part shape realizing the localized details. For the first operation, the deformation is realized by the mechanical action of a punch, whereas, for the second operation, the deformation is realized by applying a controlled gas pressure. This leads to a change in strain rate (from high rate to low one), which allows reducing the process time. The third approach consists in using Incremental Sheet Forming process to produce complex deep parts. This technique has numerous advantages compared to superplastic forming: in particular, the absence of die and a forming at room temperature. However, some surface defects can be generated depending on the manufacturing conditions (ex.: toolpath, speed rate, tool rotation…) [11].

(a)   (b)   (c)
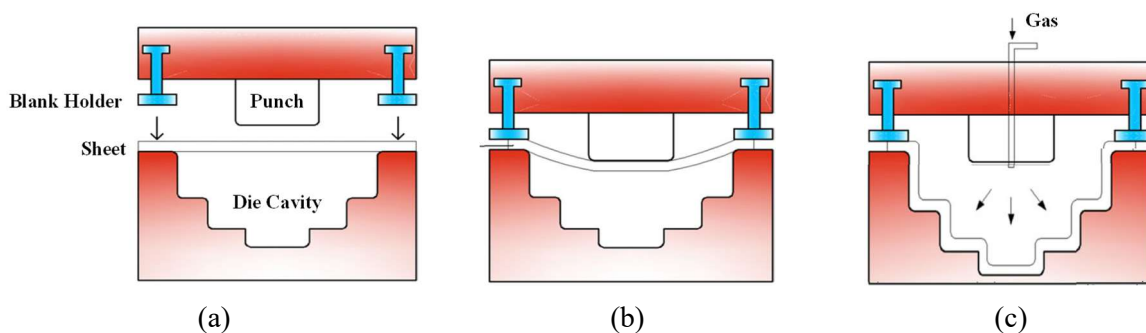
Figure I-3 Principle of the complex parts forming using combined process (warm deep-drawing followed by superplastic forming) [10]

In the present study, the second approach using the gas quick plastic forming as the pre-forming step is carried out to form complex deep parts in AA5383 alloy. The main scientific issues of this research work are summarized as follows:

2

(1) To understand the influence of the thermomechanical history of the alloy on its superplastic behavior.

(2) To propose a rheological model describing the behavior of the alloy for a wide range of thermomechanical conditions.

(3) To complete the previous model by including uncoupled damage predicting the failure behavior of the alloy under all its loading conditions.

(4) To develop a numerical tool allowing the chaining of the concerned processes.

I.3 Outline of the present thesis

The outline of this document is shown in Figure I-4. The work performed during the PhD dissertation is introduced in Chapter I. Next, chapter II presents the literature review about current research statement, including hot forming techniques, constitutive model, damage model and some properties for 5xxx aluminum alloys. In chapter III, our researched material AA5383 alloy is characterized, including microstructural and mechanical approaches. The mechanical experiments consist of flow behavior, yield function and damage analysis. Chapter IV focuses on material identification and numerical implementation of the studied models. Based on the experimental results, the behavior laws are presented. The BBC2003 yield criterion with a composite hardening model is employed to describe the mechanical response. Their implementation, in the finite element code ABAQUS©, is realized through a user defined subroutine (UMAT). The damage behavior is described by the modified Mohr Coulomb criterion. The fracture model parameters are identified from the loading paths extracted from numerical simulations with shell elements. The influence of temperature, strain rate and stress triaxiality are investigated. Hot forming simulations and corresponding experiments are carried out in Chapter V. The forming strategies are evaluated and the comparison between the experimental and numerical results is discussed. Lastly, the main conclusions and perspectives are presented.

Chapter I: Introduction

Specific objectives

Chapter II: Literature Review

To experimentally characterize the microstructure and mechanical behavior of material in the studied forming conditions.

Chapter III: Material Characterization

Based on the experimental data, to develop and implement a constitutive model and a damage model that accurately predict the material hot deformation behavior.

Chapter IV: Parameters identification and Numerical implementation

To perform complex forming simulations with identified models and validate the numerical results with corresponding experiments

Chapter V: Forming simulation and experimental validation

Conclusions and perspective

Figure I-4 Summarized structure of the information presented in this document

Chapter II.　　Literature review

In this chapter, the sheet metal forming techniques, which are commonly used in industry, are first presented. Specific care is taken to discuss the advantages and disadvantages of each of these forming techniques. Then, the constitutive models for metallic alloys in the hot temperature deformation range are described. Also, since another important issue for metal forming is the accurate prediction of ductile fracture, a brief overview of ductile fracture and damage criteria is given. Two different types of approaches are considered: the uncoupled approach and the coupled approach. The last section focuses on the specific features of the behavior of AA5xxx aluminum alloys at elevated temperatures.

II.1　Hot forming in the industry

The need for light metallic alloys in the automotive and aerospace industry has recently increased for both structural and body parts. Wrought aluminum alloys are the most popular raw material for panel structures. Generally, both non-heat treatable AA5xxx, and heat treatable AA6xxx, AA7xxx and AA2xxx are widely used for automotive and aircraft applications, as shown in Figure II-1.

It should be noticed that the workability of an alloy determines its application. For high strength aluminum alloys, which have similar strength levels to conventional mild steel, the ductility is poor at room temperature. These alloys are therefore unable to sustain large deformations and are poor candidates for the manufacturing of complex shaped parts. To circumvent the difficulties, some advanced forming techniques have been developed. The commonly used sheet metal forming techniques for wrought aluminum alloys and the strategies to improve the forming efficiency are discussed in this section.

(a)　　　　　　　　　　　　　　　　(b)
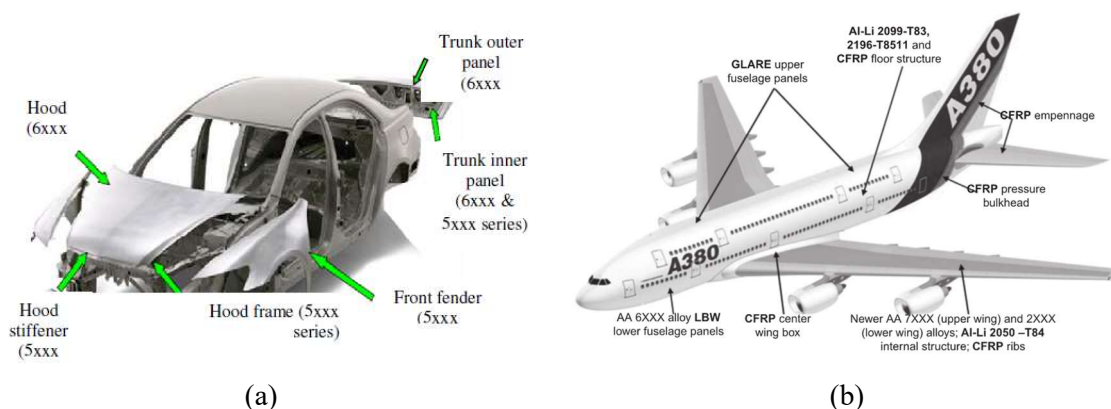
Figure II-1 Application of aluminum alloy panel structures in (a) automobile [12] and (b) aircraft [13]

To solve the problem of ductility and provide the possibility of manufacturing complex-shaped components, aluminum alloys are often formed at elevated temperatures. The ductility is increased and the strength is reduced with increasing forming temperature. Different elevated temperature forming techniques have been extensively investigated and used for industrial applications. The classification map of different forming techniques according to the approximate temperature and strain rate is shown in Figure II-2 [14]. For aluminum alloys, the elevated temperature forming techniques can be further divided into warm and hot forming conditions with traditional forming processes. Generally, warm forming refers to the case when the temperature is comprised between 0.3 times of the melting temperature and the recrystallization temperature [15]. For hot forming techniques, the temperature is selected to be above the recrystallization temperature and below the solidus temperature. The specific case of semi-solid forming (i.e. above the solidus temperature) is not considered in this review.
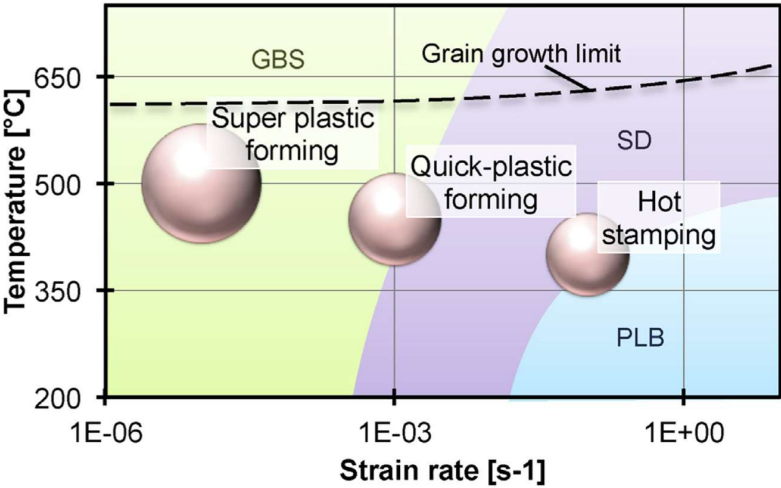
Figure II-2 Classifications of elevated temperature forming techniques [14]

II.1.1   Stamping

The most commonly used sheet metal forming technique is stamping of sheet alloys at warm temperature using conventional rigid dies. Based on the die temperature, the process can be divided into isothermal and non-isothermal conditions. The typical non-isothermal warm stamping forming process is shown in Figure II-3. The blank sheet is heated to an elevated temperature by an external furnace while the die is kept at room temperature by cooling water. The warm stamping process has some advantages, including higher material ductility and forming limit (shown in Figure II-4) [16], less spring back effect compared to cold stamping [17], increase of drawability due to non-uniform temperature distribution [18], higher manufacturing efficiency compared to warm hydro-forming and warm incremental forming. However, there are some limitations for warm stamping forming, such as the fact that it is not suitable for high-strength heat treatable aluminum alloys and the need for high-temperature lubricants.
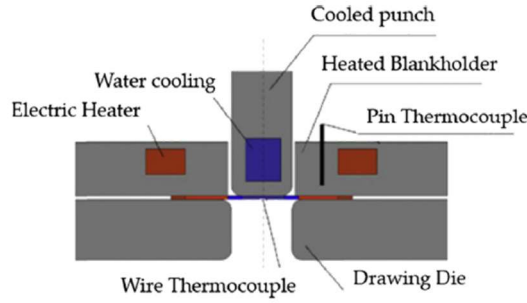
Figure II-3 Schematic of non-isothermal warm stamping [19]

(a)

(b)
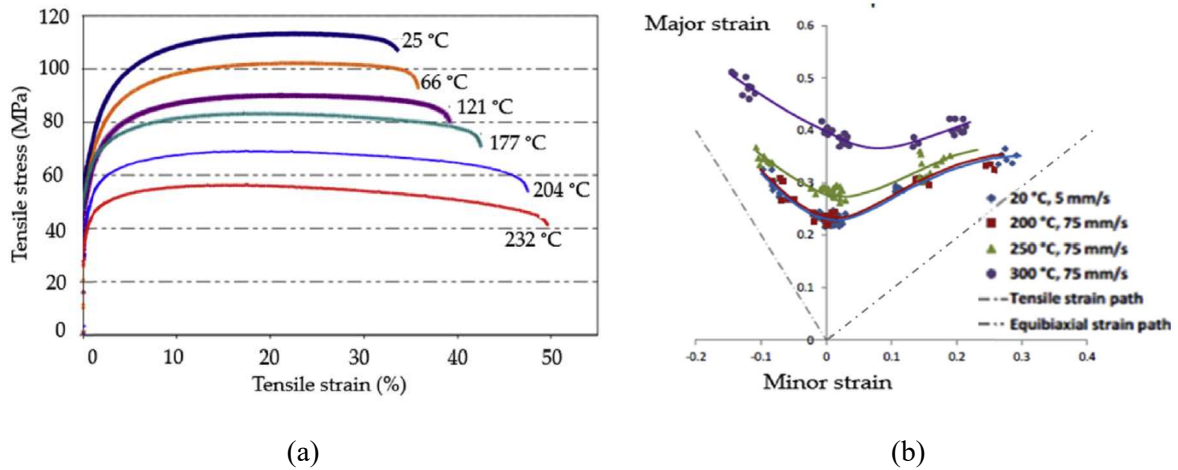
Figure II-4 (a) Improved uniaxial ductility of warm forming [16]; (b) Improved forming limits in warm forming conditions [20]

To extend the applications of aluminum alloys in the transportation industry, hot stamping has been developed to form high-strength heat treatable aluminum alloys at higher temperatures than conventional warm stamping forming. Two typical hot stamping techniques exist: the Hot Form and Quench technique proposed by Lin et al. [21] and the hot stamping process proposed by Maeno et al. [22]. For the Hot Form and Quench process, the blank is firstly heated to its solution heat treatment temperature which is kept constant for a specific time to dissolve the coarse precipitates within the α-Al matrix. The blank is then quickly stamped and quenched by holding it with the cold dies for a short period of time. The high cooling rate obtained with quenching allows preventing the formation of a coarse secondary phase at grain boundaries. The hot stamped part can be artificially aged to achieve higher strength to meet the design requirement of vehicle manufacturers. For the other typical hot stamping forming technique of Maeno et al. [22], the process uses a T4 condition and a quick heating below the solution treatment temperature. The following steps are stamping and artificial aging. Aluminum alloy aircraft parts with a high strength and dimensional accuracy can be successfully produced with this process.

II.1.2 Hydroforming

Sheet hydroforming is a metal forming technology originating from the hydroforming technology which was first developed in the 1990s [23]. A typical forming method in sheet hydroforming techniques is hydrodynamic deep drawing, shown in Figure II-5. In this forming process, oil or any other pressuring liquid media are used to press the sheet metal tightly onto the punch where it is drawn into the die by a rigid punch. The liquid medium in the die cavity can reduce the friction between the sheet metal and die, leading to a higher drawing ratio value of the sheet metal. The quality of the part can also be improved.

There are some advantages of sheet hydroforming:

- Friction at the flange can be reduced due to fluid lubrication
- Draw-ability can be significantly increased
- Reduced surface defects of the formed parts due to the liquid pressure medium
- Fewer dies are used thus reducing the tool cost

Despite the above advantages, some drawbacks also exist for sheet hydroforming. The manufacturing efficiency is low, especially for the automotive industry and the manufacturing cost per part is high when compared to conventional stamping forming processes. Even though the shape distortion and spring back can be eliminated with sheet hydroforming, an additional heat treatment process is needed to restore the component strength, resulting in an additional cost.

For the warm sheet hydroforming technique, the blank is simultaneously heated with forming dies using an external furnace [24] or heating bands [25]. In comparison with cold hydroforming, warm hydroforming uses the improved formability of aluminum alloys at elevated temperatures, which is especially effective for high strength aluminum alloys, like AA6xxx and AA7xxx with poor formability at room temperature [26]. It should be noticed that for warm hydroforming, the forming temperature depends on the pressurizing medium sustainable temperature. The conventional oil medium temperature is below 300°C, which means that sheet hydroforming is not suitable for the hot forming temperatures.
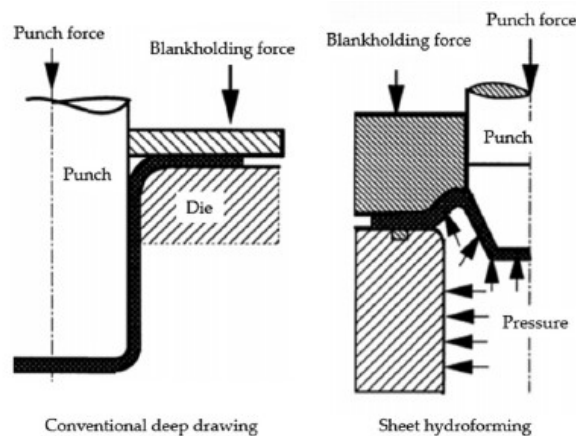
Figure II-5 Comparisons between conventional deep drawing and sheet hydroforming [23]

II.1.3 Incremental forming

Incremental forming was first introduced by Matsubara in 1993 [27]. The process can be divided into different types according to the tool configuration [28], shown in Figure II-6. Single point incremental forming is the most commonly used technique. During the process, the blank holder is used to clamp and hold the blank sheet in position. The rotating single point forming tool is utilized to progressively form the sheet into a component and its path is generated by a computer numerically controlled (CNC) machining center. During the incremental forming process, no backup die is used to support the bottom surface of the deformed sheet. The advantages of incremental forming are listed below [29, 30]:

- Forming operations can be performed by a conventional CNC machine, and hydraulic pressure is not required
- The shape design is efficiently changed by using the programming of CNC machine
- No male or female dies are required
- Formability can be increased due to low forming load

Besides those advantages, there exist some concerns about this forming technique: (1) low production efficiency; (2) thinning of the formed sheet and (3) limited geometry accuracy due to both accumulated step change errors and spring back. Hot incremental forming is an improvement of the conventional incremental forming technique. Various kinds of heating methods have been used to heat the alloys during forming operations. Ji and Park [29] used hot air blowers to heat an AZ31 sheet blank, Duflou et al. [30] utilized a laser-assisted local heating method for a Ti6Al4V sheet during the single point incremental forming. Fan et al. [31] adopted the electrical heating method to heat the blank with the aid of an external electrical power supply and material resistance. The above heating strategies can also be combined to increase the heating efficiency.
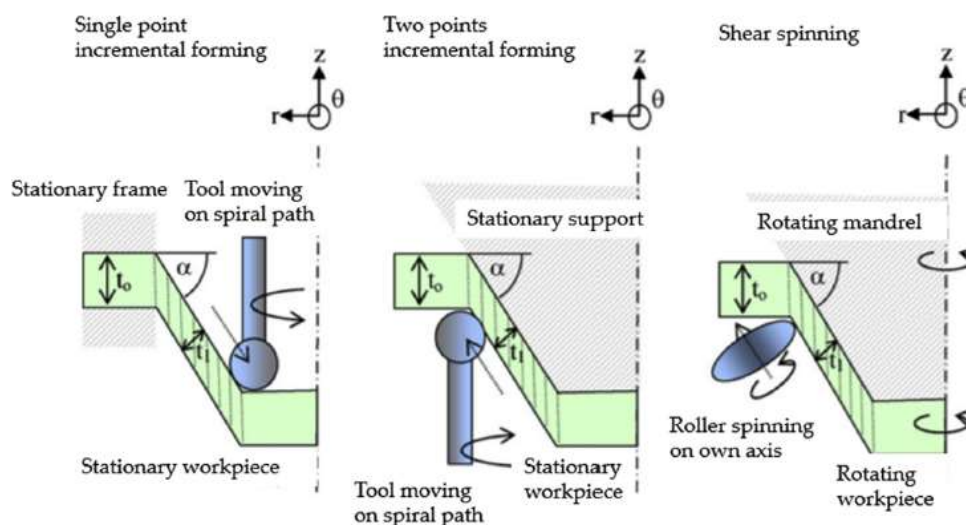
Figure II-6 Schematics of incremental sheet forming with various tooling configuration [28]

II.1.4 Superplastic forming

Superplastic deformation leads to neck-free elongations which can exceed several hundred percent in some metallic materials, as illustrated in Figure II-7. This specific behavior is obtained by changing the accommodation mechanism compared to plastic deformation.
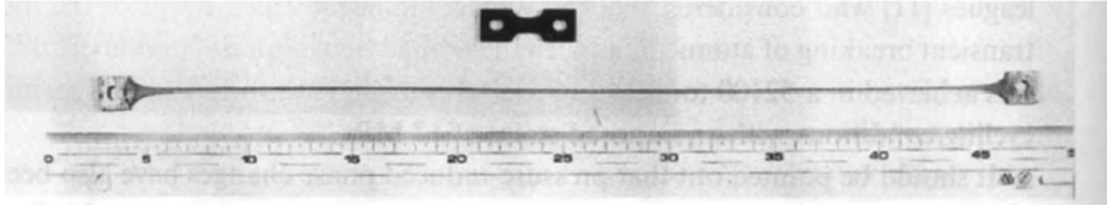
Figure II-7 Superplastic deformation in a Cu-Al alloy [32]

As shown in Figure II-8, during superplastic deformation, original grain shape and size are kept constant but neighbor grains keep changing and dislocation density does not change. In other words, superplastic deformation: (i) doesn't involve appreciable dislocation activity, (ii) maintains the identity of individual grains with no massive recrystallization, (iii) maintains the grains shape during the deformation, (iv) exhibits a dependence to the texture present prior to deformation, (v) activates specific mechanisms (Grain Boundary Sliding and diffusive flow).
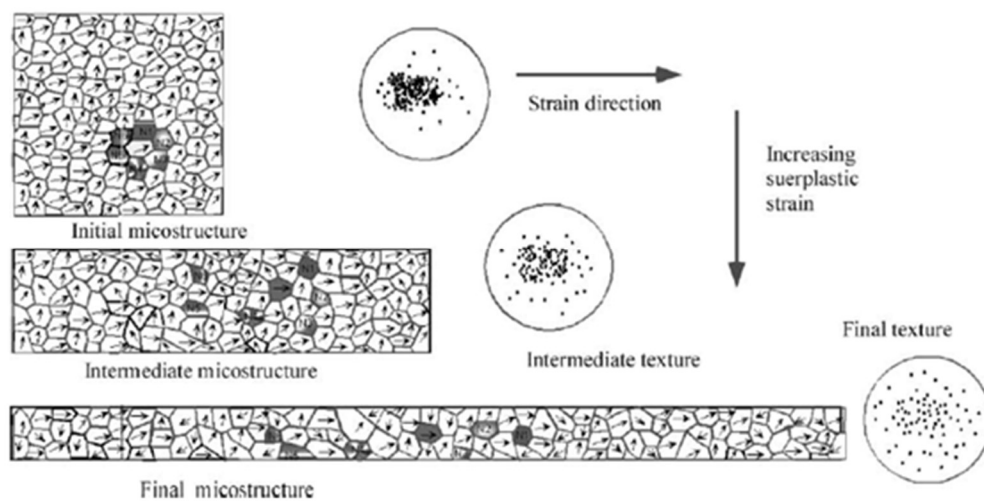
Figure II-8 Evolution of microstructure and texture during superplastic deformation[33]

Superplastic forming (SPF) technique for metals and alloys was first closely studied by Backofen, Turner and Avery at MIT in 1964 [34]. Generally, superplastic forming takes place at high temperatures and low forming strain rates, which allows the forming of more complex parts than traditional forming methods. There are three primary requirements for superplasticity: (1) an ultra-fine grain size less than 10μm; (2) a forming temperature greater than 0.5 T_m where T_m is the melting temperature of the material; (3) an important strain-rate sensitivity around 0.5. This forming technique has attracted a great attention

in the industry, mostly for the fabrication of complex shaped components in the aerospace and automobile industries. The advantages of superplastic forming are [35]:

- Close dimensional accuracy
- Excellent surface finish
- Ability to produce complex shaped products in one operation, eliminating unnecessary joints and rivets.
- Reduction of residual stresses, the absence of spring back
- Excellent mechanical properties due to having been formed from ultra-fine equiaxed grains
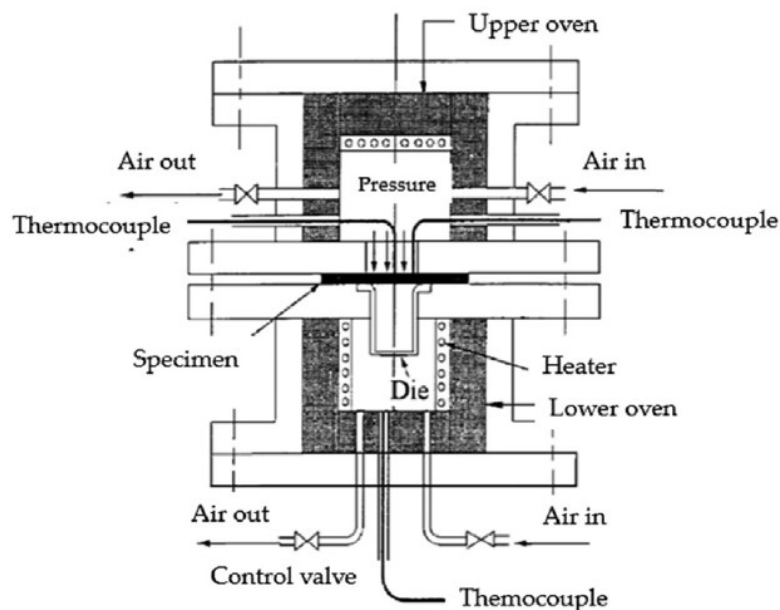
Figure II-9 Schematic of superplastic forming [36]

A typical SPF device is presented in Figure II-9. The superplastic alloy sheet is placed between the upper and lower ovens and the gas is introduced. There is no punch for this process since gas pressure alone is responsible for forming the sheet into the designed shape. The pressure during forming is slowly increased to maintain the optimum strain rate, which is a necessary condition to have a high value of strain rate sensitivity. This is important to reach the maximum elongation and to form complex shaped products having excellent dimensional accuracy and mechanical properties.

The major limitation of SPF is the high forming cycle time due to the low forming strain rate. A decrease in grain size can ease superplastic deformation which can thus be activated for lower temperatures and higher strain rates [37]. These new thermomechanical conditions can allow decreasing the forming time significantly. The complexity of this approach is the ability to modify the grain size of the received material. This is generally obtained by using a Severe Plastic Deformation technique. One technique, restricted to thin sheets, was first developed by Shin et al [38] to refine the grain size of pure aluminum: Constrained Groove Pressing. As shown in Figure II-10 (a), this process consists in pressing

a sheet using groove dies and then straightening it using flat dies. This cycle is repeated several times with a rotation of the sheet by 180° between each cycle. It leads to the development of pure shear deformation under plane strain within the inclined regions and to no deformation within the flat regions. After several cycles, a homogeneous strain distribution throughout the sheet is obtained without any changes in its dimensions. It has also been successfully applied on magnesium alloy sheets [8], as shown in Figure II-10 (b) for an AZ31B alloy, and on steel and copper sheet alloys [39, 40].

(a)
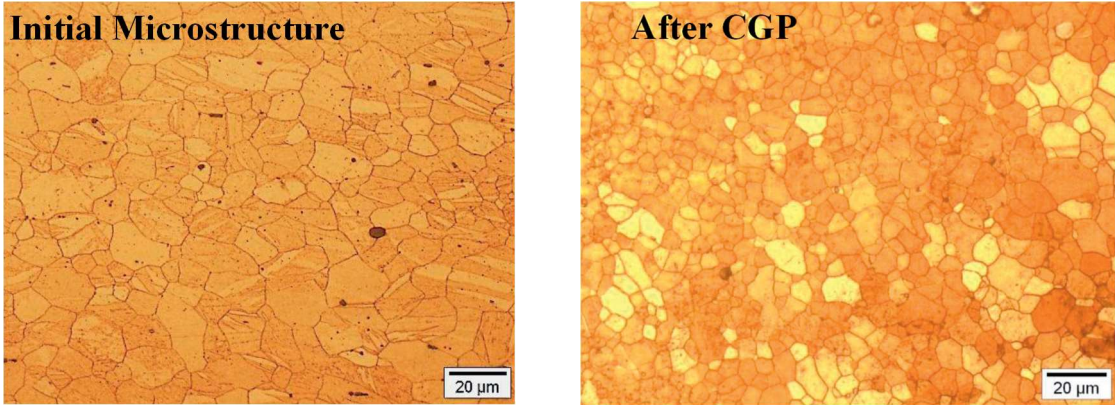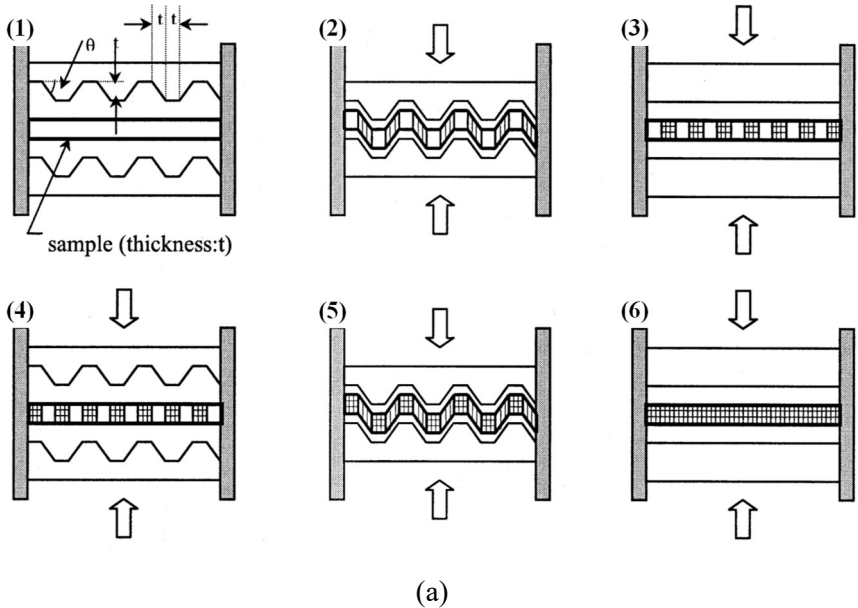
(b)

Figure II-10 (a) Principle of Constrained Groove Pressing [38] and (b) Illustration of grain modification in a magnesium alloy (AZ31B) [8]

The commercial aluminum alloys suitable for superplastic forming are listed in Table II-1. These alloys can be divided into two groups: those which are recrystallized before SPF, and those which develop superplastic microstructures during the early stages of hot forming. AA5083 and AA7475 belong to the former group, while AA2004 is the latter group. In recent years, many efforts have been

made to develop Al-Li alloys for aerospace applications. While currently not of commercial interest, AA8090, which is listed in Table II-1, can be processed to display superplastic properties. Having the similar chemical composition with our studied alloy (AA5383), the AA5083 alloy is described here in detail. This alloy is a non-heat treatable alloy containing small varying amounts of the residual elements Fe and Si. It is a relatively inexpensive material, displaying medium strength, good corrosion resistance, and can be processed to have a moderate degree of superplastic ability. Nowadays, the AA5083 alloy is the main Al alloy used for the production of non-structural parts by SPF.

Alloy	Composition, wt%	SPF temperature (°C)	Strain rate (s^{-1})	Elongation (%)
2004	Al-6Cu-0.4Zr	460	$\sim 10^{-3}$	800~1200
5083	Al-4.5Mg-0.7Mn-0.1Zn	500-520	$\sim 10^{-3}$	~300
7475	Al-5.7Zn-2.3Mg-1.5Cu-0.2Cr	515	2×10^{-4}	800
8090	Al-2.4Li-1.2Cu-0.7Mg-0.1Zr	530	5×10^{-4}	100
2090	Al-2.5Cu-2.3Li-0.12Zr	530	$\sim 10^{-3}$	500

Table II-1 Superplastic alloys and corresponding superplastic forming conditions [41]

II.1.5 Quick plastic forming

Quick plastic forming (QPF) refers to a commercial hot blow forming process which has been developed by the General Motors Company. Briefly, for the QPF process, aluminum alloys are deformed at strain rates greater than those associated with SPF. It takes advantage of the high speed of hot drawing and the excellent formability of superplastic materials. The process is highly optimized in an effort to minimize cycle time and maximize the productivity of the greater capital equipment. Another aspect is that QPF generally produces parts of less complexity compared to the SPF process. The key differences between QPF and SPF are listed in Table II-2.

	Superplastic forming	Quick plastic forming
Process variables	Strain rate/ Temperature chosen for exploiting maximum material ductility	Strain rate/Temperature chosen to maximize productivity consistent with final quality
Market features	Aerospace • Low volume • High price points product • Hand rework common for dimensional and surface quality	Automotive • High volume • Low price product • Emphasize first time dimensional and surface quality
Typical panels	Extreme shapes High forming strains-back pressure to limit cavitation Maximum mechanical properties	Moderate forming strains-back pressure not required Moderate post-form strength

Table II-2 Comparison of SPF and QPF process by Krajewski and Schroth [42]

13

QPF has some advantages when compared to SPF:

- Lower forming temperature. This greatly brings down the processing cost
- No requirement for superplastic grade alloy sheet. Ordinary alloy sheets can be used since the first step is hot drawing and not SP deformation
- Lower forming cycle times due to the relatively higher forming strain rate

Figure II-11 shows the device of quick plastic forming. Even though the shape complexity is less than in superplastic applications, high-temperature forming can still overcome the difficulties associated with the poor formability of aluminum sheet alloys.
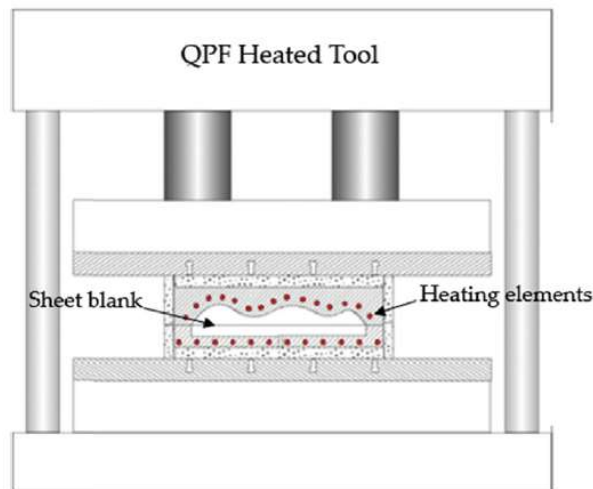
Figure II-11 Schematic of quick plastic forming [43]

II.1.6 Hybrid forming technique

The superplastic forming technique offers the advantage of forming complex deep parts. However, the long forming times due to low strain rates limit its wide application in an industrial context. In this background, two novel SPF processes have been developed by using pre-forming: hot draw mechanical pre-forming and quick plastic gas pre-forming.

Hot Draw Mechanical Pre-Forming

The hot draw mechanical pre-forming technique was first developed by Friedman [44] to form a sheet of ductile material. Shown in Figure II-12, the forming process contains two separate forming steps. The sheet is first externally preheated to the target forming temperature and then automatically loaded onto the heated blank holder, which is supported by a movable cushion system, as shown in Figure II-12(a). The upper die is then lowered until it engages the blank holder and wraps the material around the punch. The press tonnage is increased to seal the die once the blank holder reaches the die shoe (Figure II-12(b)). Gas is then introduced into the lower cavity to complete the part, as shown in

Figure II-12(c). After completion, the gas pressure is released and the upper die is raised to remove the forming part from the die.

In recent years, the hot draw mechanical pre-forming technique has also been applied to form SPF AA5083 and non-SPF AA5182 alloys by Luo et al. [9], and non-SPF AA5083, Ti-6Al-4V alloys by Liu et al. [10, 45] and AZ31B alloy by Wu et al. [46]. In those studies, the forming time cycles, as well as the required forming temperature and the sheet thinning, are reduced compared to the conventional SPF process. Also, the required forming temperature is lower and the sheet thinning is reduced.

(a)   (b)   (c)
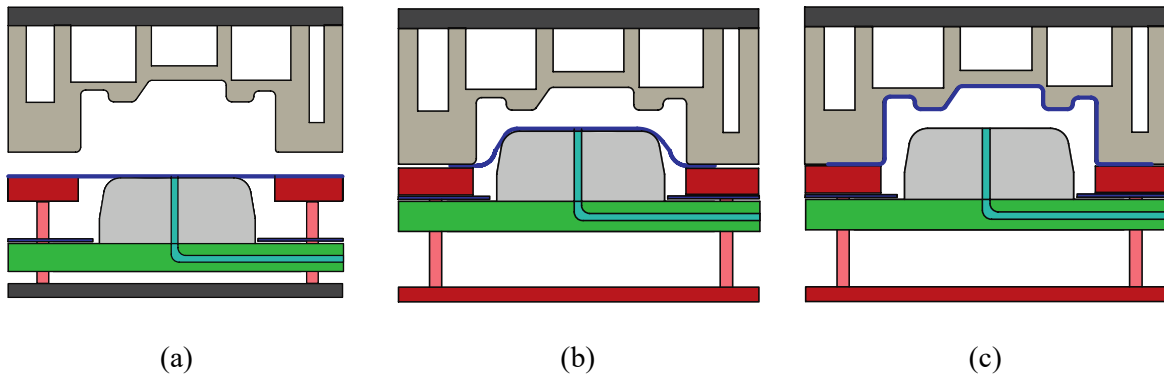
Figure II-12 Schematic of the hot draw mechanical pre-forming process (a) the sheet is first loaded into the die set; (b) a drawing stage pre-forms the panel and (c) a gas forming stage completes the forming operation [9]

The microstructural evolution of AA5083 has been studied in the hybrid forming process [47]. Shown in Figure II-13, after hot drawing pre-forming, most of the grains are elongated along the deformation direction from the initial equiaxed shapes. Because of geometric dynamic recrystallization, many sub-grains are formed within the initial large grains. Once forming is completed, a fairly uniform microstructure is obtained. When comparing the microstructures before and after blow forming, most of grains and sub-grains have grown and the average aspect ratio of the grains has decreased. The elongated grains with sub-grain boundary arrays shows the occurrence of sub-grain rearrangement. In the gas forming stage, dynamic recrystallization, though in a limited amount, seems to contribute to the random distribution of boundary misorientation angles.

(a)   (b)   (c)
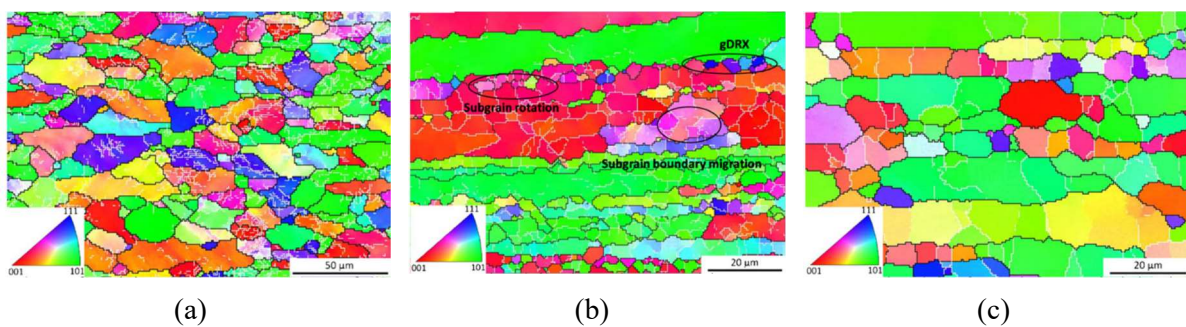
Figure II-13 A EBSD map of annealed AA5083 alloy (a) before forming; (b) after hot stamping (pre-forming) and (c) end of gas forming [47]

Quick Plastic Gas Pre-Forming

In the past years, quick plastic forming has been successfully applied as a forming technique of aluminum sheets in the automotive industry, especially in the case of Al-Mg alloys [42, 43, 48]. The main deformation mechanism for QPF is dislocation creep (DC), which is similar to hot deep drawing, while grain boundary sliding (GBS) plays an important role for SPF conditions. When DC is controlled by a viscous glide, the strain rate sensitivity is usually about 0.3, which is lower than for SPF conditions (m~0.5). The forming limit for the QPF is thus lower than SPF. To reduce the forming time of SPF, QPF can also be used as a pre-forming technique, like the hot-drawing mechanical pre-forming, to form the blank into a certain shape.

II.1.7 Synthesis

In this section, the commonly used sheet metal forming techniques have been reviewed.

The <u>warm stamping</u> is a widespread forming technique in the industry due to its higher manufacturing efficiency compared to other forming techniques. However, because of the relatively lower forming limit, this forming technique is restricted to simple shapes only. There also exists spring back and shape distortion problems for stamping.

The <u>hot stamping technique</u>, which consists of increasing the forming temperature above the recrystallization temperature, allows circumventing those drawbacks. This forming technique can however only be applied to high strength heat treatable aluminum alloys.

<u>Sheet hydroforming</u> technique can improve the draw-ability and reduce surface defects compared to the conventional stamping forming process. Low manufacturing efficiency and high manufacturing cost per part are the drawbacks of this technique. Moreover, the temperature for hydroforming is limited by the pressuring medium sustainable temperature.

Another forming technique, which provides an increase formability of aluminum alloys, is <u>incremental forming</u>. No male or female dies are required for this forming technique and the change of shape design is very efficient. The limitation of incremental forming is also the low forming efficiency, as well as the thinning of the formed sheet and the limited geometry accuracy. The forming limit of conventional incremental forming can be further increased by using a heating device.

Two forming techniques involving a pressuring gas have also been introduced: <u>superplastic forming (SPF) and quick plastic forming (QPF)</u>. SPF is the most widely used forming technique for deep complex parts due to its extreme high forming limit, excellent surface finish, close dimensional accuracy, the absence of spring back and excellent mechanical properties. However, the long cycle forming time can limit its application for mass production. The high requirement for the as-received material is another limiting factor. QPF is a forming technique which, when compared to SPF, provides higher efficiency but is not well suited for complex shaped parts.

16

In order to overcome the disadvantages of SPF, some <u>hybrid forming techniques</u>, which use a pre-forming stage, have been developed: hot drawing mechanical pre-forming and quick plastic gas pre-forming. The pre-forming before SPF can reduce the total forming time while keeping the quality of forming parts. From my literature review, no research has been carried out on the quick plastic gas pre-forming technique. Similar to the hot-drawing mechanical pre-forming technique, the strain rates in the pre-forming stage of the quick plastic gas pre-forming technique would be out of the superplastic range.

II.2 Constitutive models for hot forming

The material flow behavior during hot forming operations is often complex. The hardening and softening mechanisms are influenced by strain, strain rate and forming temperature. The thermo-mechanical parameters can lead to a particular microstructure evolution; while on the other side, the microstructure changes during the hot forming process can in turn affect the mechanical characteristics like the flow stress. A precise description of the flow behavior of metals and alloys in hot deformation conditions is of a great importance for the design of metal forming operations. A constitutive relation is often used to describe the metal flow behavior in a form that can be easily be integrated into a computer code to model the hot forming process under the specific loading conditions. Of course, the results of numerical simulations are reliable only when a proper constitutive model is applied. Generally, an ideal plasticity model for metals and alloys can precisely describe the material thermo-mechanical behavior, providing the relationship between stress, strain, strain rate and forming temperature. In this section, a review on constitutive models for metals and alloys in hot working conditions is presented. The constitutive models are divided into three main categories: phenomenological constitutive models, physically-based constitutive models and artificial neural network models.

II.2.1 Phenomenological constitutive models

Phenomenological models are widely used in the simulation of the forming process for metals and alloys at high temperatures due to their easy implementation. So far, there exists many phenomenological models, including the Johnson-Cook (JC) model, the Khan-Huang-Liang model, the Field-Backofen model, the Voce-Kocks model, the Arrhenius equation and some other phenomenological models. The feature for the phenomenological constitutive models is that the flow stress can be represented as a function of equivalent plastic strain, equivalent plastic strain rate and forming temperature

$$\bar{\sigma} = \bar{\sigma}(\bar{\varepsilon}^P, \dot{\bar{\varepsilon}}^P, T) \qquad (II.1)$$

where $\bar{\sigma}$ is the equivalent stress, $\bar{\varepsilon}^P$ is the equivalent plastic strain, $\dot{\bar{\varepsilon}}^P$ is the equivalent plastic strain rate and T is the testing temperature. In this section, two most commonly used phenomenological models are introduced: Johnson-Cook model, and Arrhenius model.

II.2.1.1   Johnson-Cook model

The Johnson-Cook (JC) constitutive model [49] assumes the flow stress to depend on the strain, strain rate, and temperature, seperately. It has been successfully applied to a variety of materials in different ranges of temperature and strain rates. It is widely used, mostly because of its simplicity and the availability of parameters for many materials. The original JC model is expressed as

$$\bar{\sigma} = (A + B(\bar{\varepsilon}^P)^n)(1 + C \ln \dot{\bar{\varepsilon}}^*)(1 - T^{*m}) \tag{II.2}$$

where A, B, C, n, and m are five parameters that need to be identified. $\dot{\bar{\varepsilon}}^* = \dot{\bar{\varepsilon}}^P / \dot{\bar{\varepsilon}}_{ref}$ is the dimensionless strain rate ($\dot{\bar{\varepsilon}}_{ref}$ is the reference equivalent strain rate), and T^* is the homologous temperature which expressed as

$$T^* = \frac{T - T_{ref}}{T_m - T_{ref}} \tag{II.3}$$

where T is the testing temperature, T_m is the melting temperature, and T_{ref} is the reference temperature ($T > T_{ref}$). In Eq. (II.2), the flow stress is influenced by the strain hardening, strain rate hardening and temperature softening, separately. It is based on a multiplicative decomposition of thermal softening, strain hardening and strain rate hardening. These phenomena are therefore assumed to be uncoupled and isolated from each other.

To consider the possible strain-strain rate-temperature couplings, some modifications of the original JC model have been proposed to improve its application. Lin et al. [50] modified the original JC model by considering the coupled effect of strain rate and deformation temperature to describe the hot tensile behavior of a high-strength alloyed steel. The modified JC model is given by

$$\bar{\sigma} = (A_1 + B_1 \bar{\varepsilon}^P + B_2 (\bar{\varepsilon}^P)^2)(1 + C_1 \ln \dot{\bar{\varepsilon}}^*) \exp[(\lambda_1 + \lambda_2 \ln \dot{\bar{\varepsilon}}^*)(T - T_{ref})] \tag{II.4}$$

where A_1, B_1, B_2, C_1, λ_1, λ_2 are the material parameters. This modified JC model has been used to predict the hot deformation behavior of the 6026 aluminum alloy under a wide range of temperatures (673~823 K) and strain rates (0.001~10 s^{-1}). Figure II-14 shows the comparison between the modified JC model and the experimental results. It is obvious that the predicted flow stresses agree well with the experimental results, which confirms that the modified JC model proposed by Lin et al. [50] can accurately describe the hot compression behavior of the 6026 aluminum alloy in the studied temperature and strain rate range.
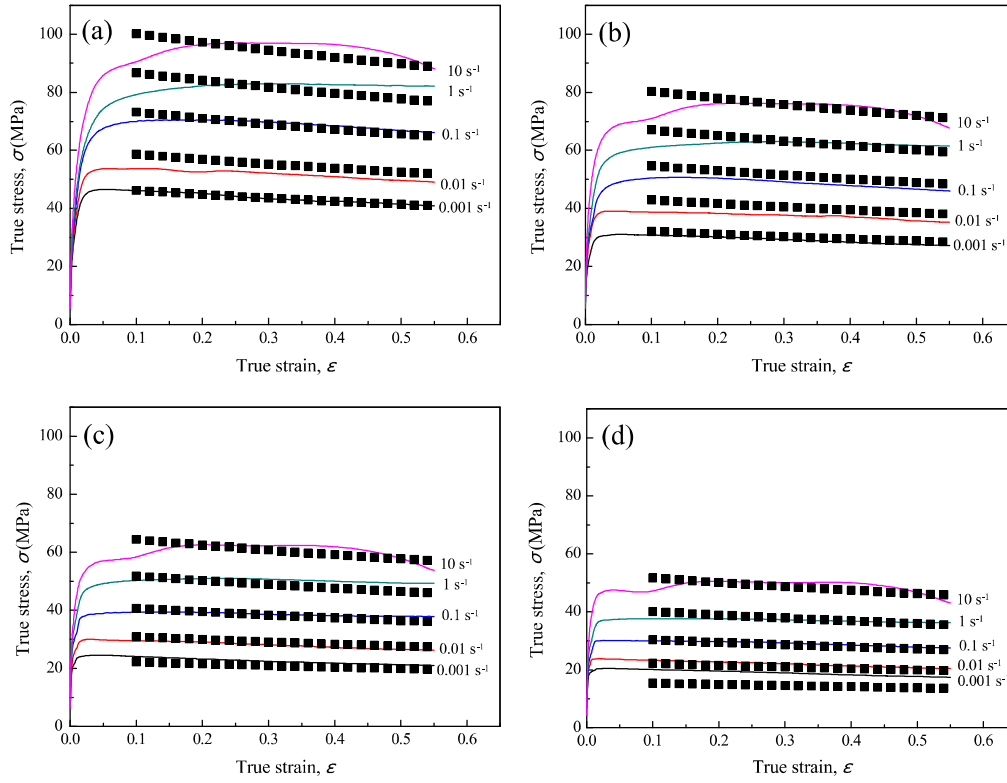
Figure II-14 Comparisons between the experimental (solid lines) and modified JC model predicted (solid symbols) flow curves of AA6026 at (a) 673 K; (b) 723 K; (c) 773 K; (d) 823 K [51]

There are also some other modifications to extend the application of the JC model. For example, Hou and Wang [52] modified the thermal softening part to describe the flow behavior under a wide range of temperature, even the current temperatures were lower than the reference temperature. Zhang et al [53] modified the original JC model by considering the effects of forming temperature on the strain-hardening behavior for IC10 alloys. Lin and Chen [54] developed a combined JC model and Zerilli-Armstrong model to describe the flow stress behavior for hot compressed 42CrMo alloy steel. A detailed review of modified JC models can be found in [55].

II.2.1.2   Arrhenius model

The Arrhenius model is mostly used to describe the material flow behavior at high temperatures. The effect of temperature and strain rate on the deformation behavior can be represented by the Zener-Hollomon parameter in an exponent-type equation [56]. Those expressions are listed as follow

$$\dot{\bar{\varepsilon}}^{P} = \hat{A}F(\bar{\sigma})\exp(-\frac{\hat{Q}}{RT}) \tag{II.5}$$

$$Z = \dot{\bar{\varepsilon}}^{P}\exp(\frac{\hat{Q}}{RT}) \tag{II.6}$$

$$F(\bar{\sigma}) = \begin{cases} \bar{\sigma}^{n_1} & \alpha\bar{\sigma} < 0.8 \\ \exp(\beta\bar{\sigma}) & \alpha\bar{\sigma} > 1.2 \\ [\sinh(\alpha\bar{\sigma})]^n & \text{for all } \bar{\sigma} \end{cases} \tag{II.7}$$

where R is the universal gas constant (8.31 J mol^{-1} K^{-1}), $\hat{Q}$ is the activation energy of hot deformation, $\hat{A}$, α and n are the material constants, $\alpha = \beta / n_1$. The power law and the exponential law are suitable for the low stress ($\alpha\bar{\sigma} < 0.8$) and the high stress ($\alpha\bar{\sigma} > 1.2$), respectively. However, the hyperbolic sine law can be used over a wide range of deformation conditions. For all stress levels, Eq. (II-5) is represented by

$$\dot{\bar{\varepsilon}}^P = A[\sinh(\alpha\bar{\sigma})]^n \exp(-\frac{\hat{Q}}{RT}) \tag{II.8}$$

Then the flow stress can be rewritten as the function of Z parameters, considering the definition of the hyperbolic law given as

$$\bar{\sigma} = \frac{1}{\alpha} \ln\{(\frac{Z}{\hat{A}})^{1/n} + [(\frac{Z}{\hat{A}})^{2/n} + 1]^{1/2}\} \tag{II.9}$$

The above equation does not consider the effect of strain on the flow stress. In recent years, many investigations [57-65] have established the flow stress of different metals and alloys during hot deformation by the Arrhenius model with the strain compensation technique. According to this technique, the values of $\hat{Q}$, $\hat{A}$, n, and α are expressed as polynomial functions of strain. For example, in order to accurately predict the high-temperature flow behavior of an AA2030 aluminum alloy with the Arrhenius model, Ashtiani et al. [65] have used the following functions of strain

$$\begin{aligned} \alpha &= B_0 + B_1\bar{\varepsilon}^P + B_2(\bar{\varepsilon}^P)^2 + B_3(\bar{\varepsilon}^P)^3 + B_4(\bar{\varepsilon}^P)^4 + B_5(\bar{\varepsilon}^P)^5 + B_6(\bar{\varepsilon}^P)^6 \\ n &= C_0 + C_1(\bar{\varepsilon}^P) + C_2(\bar{\varepsilon}^P)^2 + C_3(\bar{\varepsilon}^P)^3 + C_4(\bar{\varepsilon}^P)^4 + C_5(\bar{\varepsilon}^P)^5 + C_6(\bar{\varepsilon}^P)^6 \\ \ln\hat{A} &= D_0 + D_1\bar{\varepsilon}^P + D_2(\bar{\varepsilon}^P)^2 + D_3(\bar{\varepsilon}^P)^3 + D_4(\bar{\varepsilon}^P)^4 + D_5(\bar{\varepsilon}^P)^5 + D_6(\bar{\varepsilon}^P)^6 \\ \hat{Q} &= E_0 + E_1\bar{\varepsilon}^P + E_2(\bar{\varepsilon}^P)^2 + E_3(\bar{\varepsilon}^P)^3 + E_4(\bar{\varepsilon}^P)^4 + E_5(\bar{\varepsilon}^P)^5 + E_6(\bar{\varepsilon}^P)^6 \end{aligned} \tag{II.10}$$

The comparison between the experimental data and predicted data of flow stress from the strain-dependent constitutive equation at various conditions is shown in Figure II-15. It can be seen that the flow stress predicted by the strain-compensated equation agrees well with the experimental results in the whole researched processing domain.
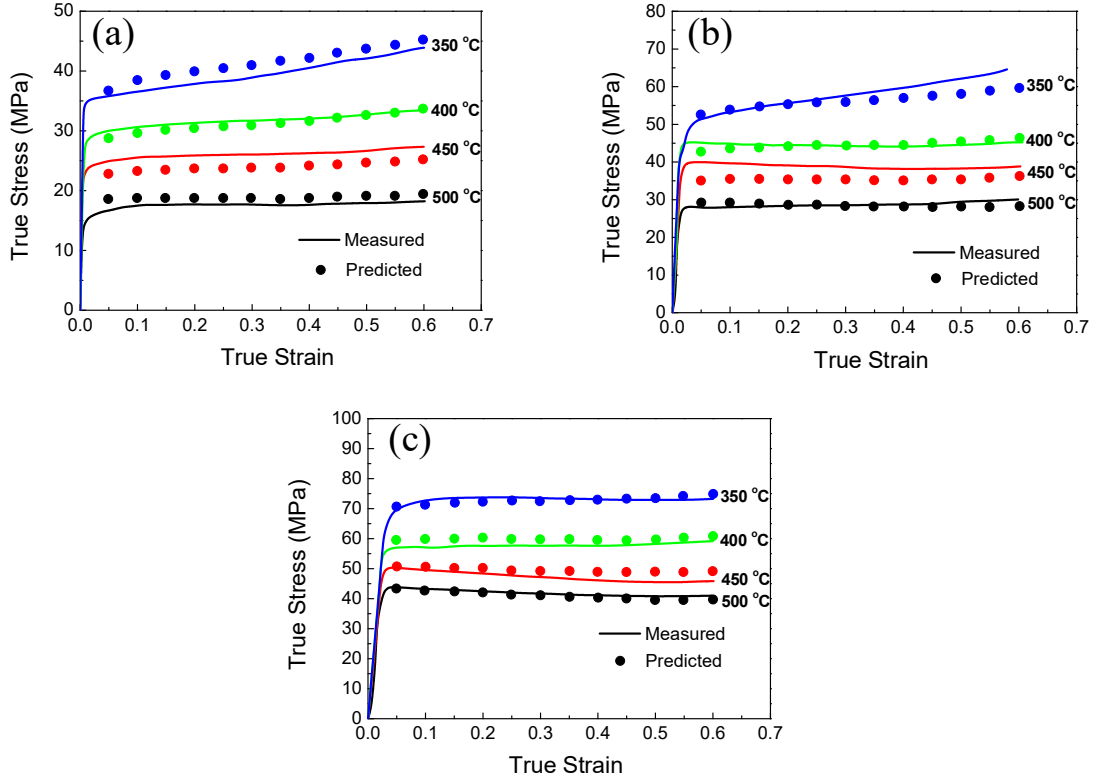
Figure II-15 Comparisons between predicted and measured flow stress curves of AA2030 at strain rates of : (a) 0.005 s^{-1}; (b) 0.05 s^{-1} and (c) 0.5 s^{-1} [65]

A further modification of the Arrhenius model has been proposed by Lin et al. [66] to predict the flow behavior of the 42CrMo steel. The modification consists in using the following expression for the Zener-Hollomon parameter

$$Z' = (\dot{\bar{\varepsilon}}^{P})^{4/3} \exp(\frac{Q}{RT}) \tag{II.11}$$

This modification has also been used for the description of the high-temperature flow behavior of the Ti-modified austenitic stainless steel [67]. We need to mention that this modification depends on the flow behavior of the material.

II.2.1.3   Composite model

In the appendix of the work of Sung et al. [68], two categories of plastic constitutive equations have been listed: integrated constitutive equations and composite functions. The Arrhenius-type model belongs to the integrated constitutive equations. For the composite functions, the material flow behavior is represented by the strain hardening or softening, strain rate sensitivity and thermal softening functions separately. According to the reference of Sung et al. [68], the material flow behavior equation can be expressed as follows

$$\bar{\sigma} = K(\bar{\varepsilon}^P + \bar{\varepsilon}_0^P)^{\hat{n}} \exp(-b\bar{\varepsilon}^P)(\dot{\bar{\varepsilon}}^P)^m \{1 - (\frac{T - T_{ref}}{T_m - T_{ref}})^{\hat{\beta}}\} \qquad (\text{II}.12)$$

where K, $\bar{\varepsilon}_0^P$, $\hat{n}$, m, b and $\hat{\beta}$ are the parameters needed to be identified, T_m and T_{ref} are the melting and the reference temperature, respectively.

II.2.2 Physically-based Models

Phenomenological models can be obtained by fitting the experimental results by mathematical equations. However, as those models do not have any physical meaning, they have natural defects in describing the material behavior, especially for hot and dynamic deformation processes, for which the internal microstructure changes extensively. Thus, some models based on physical mechanisms, such as dislocation dynamics, thermal activation and so on, have been developed. The commonly used physically-based models are the Zerilli-Armstrong (ZA) model [69], the Dynamic recrystallization (DRX) model [70], the Voyiadjis-Almasri [71] model, and some other physical based models [72-75].

II.2.2.1   Zerilli-Armstrong model

The original Zerilli-Armstrong model [69] is derived from dislocation mechanics arguments. The respective influences of strain, strain rate and forming temperature on the flow stress are considered. Generally, the equation is composed of two parts, thermal and athermal

$$\bar{\sigma} = \bar{\sigma}_a + \bar{\sigma}_{th} \qquad (\text{II}.13)$$

where σ_a is the athermal equivalent stress, $\bar{\sigma}_{th}$ is the thermal equivalent stress. The thermal equivalent stress can be represented by

$$\bar{\sigma}_{th} = \frac{M\Delta G_0}{A\hat{b}} e^{-\beta' T} \qquad (\text{II}.14)$$

$$\beta' = -C_3 + C_4 \ln \dot{\bar{\varepsilon}}^P \qquad (\text{II}.15)$$

where M is the direction factor, ΔG_0 is the free energy of thermal activation at 0 K, A is the activation area at 0 K, $\hat{b}$ is Burger's vector, β' is a parameter associated with the equivalent plastic strain rate.

As the activation area A for body-centered cubic (BCC) metals and face-centered cubic (FCC) metals are different, the thermal components for these two structures are given separately

$$\bar{\sigma}_{th} = C_1 \exp(-C_3 T + C_4 T \ln \dot{\bar{\varepsilon}}^P) \quad (\text{For BCC materials}) \qquad (\text{II}.16)$$

$$\bar{\sigma}_{th} = C_2 (\bar{\varepsilon}^P)^{\frac{1}{2}} \exp(-C_3 T + C_4 T \ln \dot{\bar{\varepsilon}}^P) \quad (\text{For FCC materials}) \qquad (\text{II}.17)$$

By combining the athermal activation stress and the effect of the average grain size on the yield strength into one component C_0, two different types of ZA models can be formulated

$$\bar{\sigma} = C_0 + C_1 \exp(-C_3 T + C_4 T \ln \dot{\bar{\varepsilon}}^P) + C_5 (\bar{\varepsilon}^P)^n \quad \text{(For BBC materials)} \quad \text{(II.18)}$$

$$\bar{\sigma} = C_0 + C_2 (\bar{\varepsilon}^P)^{\frac{1}{2}} \exp(-C_3 T + C_4 T \ln \dot{\bar{\varepsilon}}^P) \quad \text{(For FCC materials)} \quad \text{(II.19)}$$

where C_0, C_1, C_2, C_3, C_4, C_5, and n are material parameters.

The original ZA model is based on the assumption that the parameters of this model are regarded as constants at various conditions and for the whole deformation process, which is not the real case for most metals. In fact, the coupling between temperature, strain and strain rate should be considered in a constitutive model. Thus, some modifications of ZA models have been proposed in recent years. Zhang et al. [76] modified the ZA model by considering the effects of temperature, strain rate and strain on the parameters. The modified ZA model can precisely describe the hot flow behavior of the IC10 alloy over a wide range of strain rates and temperatures. Gao and Zhang [77] linked constitutive parameters directly with the characteristics of microstructures to describe the dynamic plasticity of FCC metals. There are also some other modifications of ZA model [78-80]. A modified ZA model has been proposed by Samantaray et al. [81] to describe the hot flow behavior of a titanium-modified austenitic stainless steel in the strain rate range of 0.001~1.0 s^{-1} and the temperature range of 1073~1473 K. Samantaray et al. [81] modified the ZA with the following expression

$$\bar{\sigma} = (C_1 + C_2 (\bar{\varepsilon}^P)^N) \exp\{-(C_3 + C_4 \bar{\varepsilon}^P)\hat{T} + (C_5 + C_6 \hat{T}) \ln \dot{\bar{\varepsilon}}^*\} \quad \text{(II.20)}$$

In above equation, $\hat{T} = T - T_{ref}$ with T and T_{ref} being the testing and reference temperatures, $\dot{\bar{\varepsilon}}^*$ is the dimensionless strain rate which has been defined in the JC model. While C_1, C_2, C_3, C_4, C_5, C_6 and N are material parameters. This modified ZA model has been applied to describe the static deformation behavior of 7050 aluminum alloy [57]. Shown in Figure II-16, the elevated-temperature flow behavior of this aluminum alloy can be accurately predicted by the modified ZA model. This model has been also applied for steel [82] and copper [77].
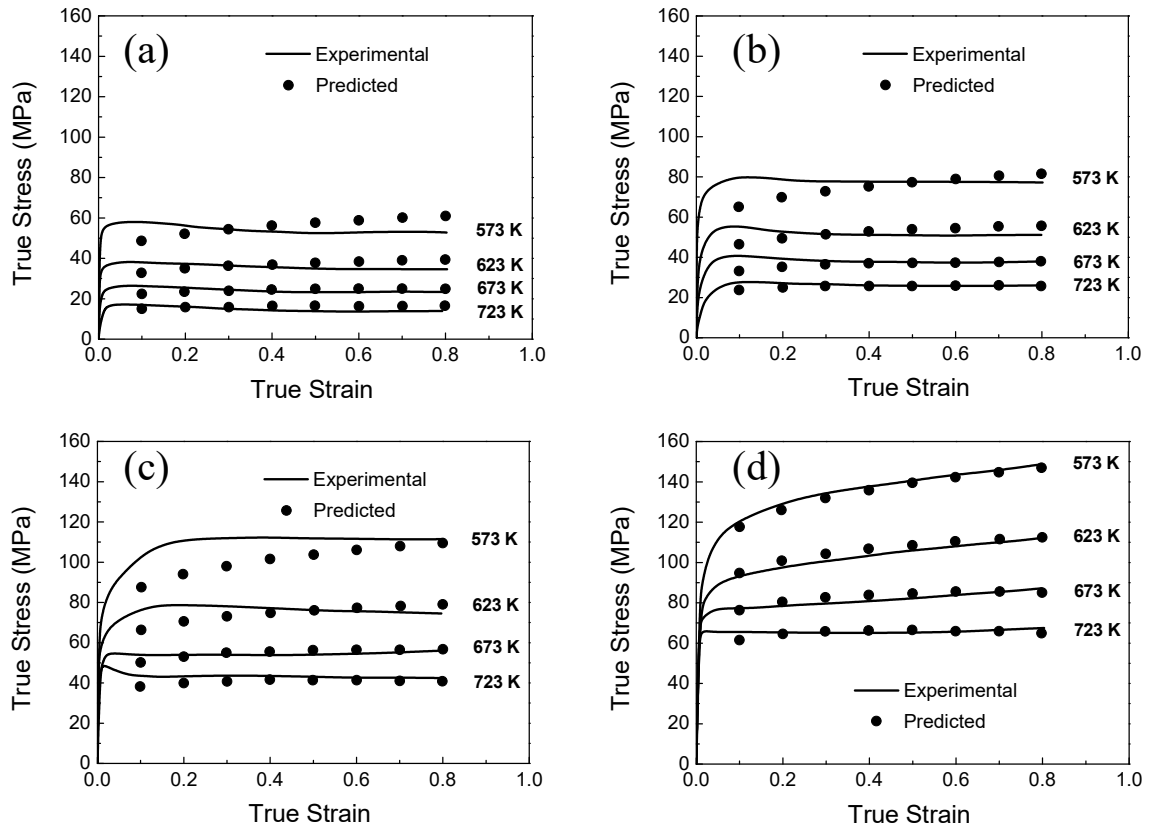
Figure II-16 Comparison between experimental and predicted flow stress for AA7050 alloy, using modified ZA model at elevated temperature at (a) 0.001 s^{-1}; (b) 0.01 s^{-1}; (c) 0.1 s^{-1} and (d) 1.0 s^{-1} [57]

II.2.2.2 Dynamic recrystallization model

The deformation process for most metallic materials can be divided into four stages [70]: Stage I (Working hardening stage); Stage II (Transition stage); Stage III (Softening stage) and Stage IV (Steady stage), especially for relatively low strain rates, shown in Figure II-17.
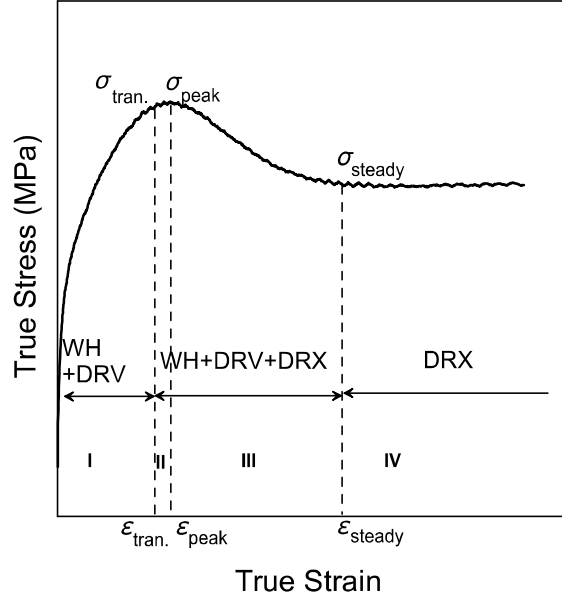
Figure II-17 Typical flow stress curve at the elevated temperature [70]

According to the work hardening and dynamic recovery, the evolution of dislocation density can be represented as follows

$$d\rho / d\bar{\varepsilon}^P = U - \Omega\rho \tag{II.21}$$

where U represents the work hardening coefficient and can be regarded as constant with respect to strain, Ω is the coefficient of dynamic recovery, ρ is dislocation density, $d\rho / d\bar{\varepsilon}^P$ is the rate of increase of dislocation density with the equivalent plastic strain. The above equation can be integrated to give

$$\rho = e^{-\Omega\bar{\varepsilon}^P}(U / e^{\Omega\bar{\varepsilon}^P} + \rho_0 - U / \Omega) \tag{II.22}$$

As the effective stress is negligible compared to the internal stress at high temperature, the applied stress can be related directly to the dislocation density

$$\bar{\sigma} = \alpha\mu b\sqrt{\rho} \tag{II.23}$$

where α is a material constant, μ is the shear modulus, b is the distance between atoms in the slip direction. In the steady-state condition, the dislocation density is

$$\rho_{DRV} = U / \Omega \tag{II.24}$$

Thus, the equivalent stress during work hardening-dynamical recovery period under hot deformation can be given by the following equation

$$\bar{\sigma} = [\bar{\sigma}_{DRV}^2 + (Y_0^2 - \bar{\sigma}_{DRV}^2)e^{-\Omega\bar{\varepsilon}^P}]^{0.5} \tag{II.25}$$

where Y_0 and $\bar{\sigma}_{DRV}$ are the yield stress and the steady-state stress due to dynamic recovery, respectively. The dynamic recrystallization phenomenon is more and more obvious at high temperatures and low strain rates. The recrystallized volume fraction X_D can be represented by

$$X_D = 1 - \exp[-K_d(\frac{\bar{\varepsilon}^P - \bar{\varepsilon}_c^P}{\bar{\varepsilon}^P})^{n_d}] \qquad (\bar{\varepsilon}^P \geq \bar{\varepsilon}_c) \qquad (\text{II.26})$$

where $\bar{\varepsilon}_c^P$ is the critical equivalent plastic strain for occurring dynamic recrystallization, K_d and n_d are dynamic recrystallization parameters. At the same time, the progress of dynamic recrystallization X_D can also be written as

$$X_D = \frac{\bar{\sigma}_{DRV} - \bar{\sigma}}{\bar{\sigma}_p - \bar{\sigma}_{DRX}} \qquad (\bar{\varepsilon}^P \geq \bar{\varepsilon}_c^P) \qquad (\text{II.27})$$

where $\bar{\sigma}_{DRX}$ and $\bar{\sigma}_P$ are the steady-state equivalent stress due to dynamic recrystallization and the peak stress, respectively. According to Equation (II.25) and Equation (II.26), we can obtain the flow stress during dynamical recrystallization period by

$$\bar{\sigma} = \bar{\sigma}_{DRV} - (\bar{\sigma}_P - \bar{\sigma}_{DRX})\{1 - \exp[-K_d(\frac{\bar{\varepsilon}^P - \bar{\varepsilon}_c}{\bar{\varepsilon}^P})^{n_d}]\} \qquad (\bar{\varepsilon}^P \geq \varepsilon_c) \qquad (\text{II.28})$$

Lin et al. [70] proposed the above constitutive equations for the work hardening-dynamic recovery period and the dynamic recrystallization period of the 42CrMo steel. Recently, this physically-based model has been also applied to the description of the hot deformation behavior of a high strength aluminum alloy (Al-Zn-Mg-Cu) [83]. As shown in Figure II-18, this model has a good prediction capability and can be used to determine the hot formation processing parameters of this alloy.
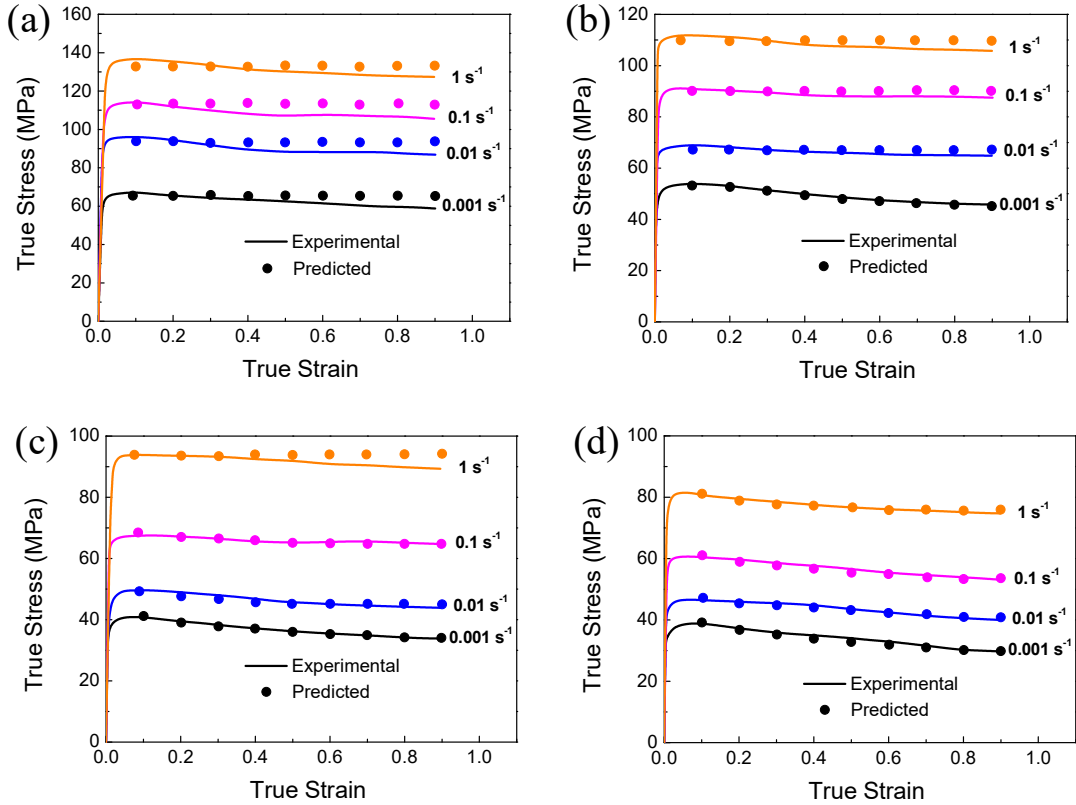
Figure II-18 Comparisons between the predicted and experimental flow stress of the Al-Mg-Zn-Cu alloy at the temperature of (a) 350 ℃; (b) 400 ℃; (c) 450 ℃ and (d) 470 ℃ [83]

II.2.3 Artificial neural network (ANN) approach

Generally, the hot deformation behavior of materials is normally described by the above mentioned phenomenological or physically-based models. However, when the response of the material behavior is quite non-linear, it is difficult to predict the flow stress precisely by using traditional computational methods. The third type of approach uses artificial neural networks (ANN) to overcome this problem. ANN are a large class of parallel processing architectures, which can mimic complex and nonlinear relationships through the application of many nonlinear processing units called neurons. One of the advantages of an AAN model is that it is not necessary to provide a mathematical model at first. Usually, the structure of an ANN is hierarchical with neurons grouped in different layers designed as an input layer, hidden layers, and an output layer, shown in Figure II-19.
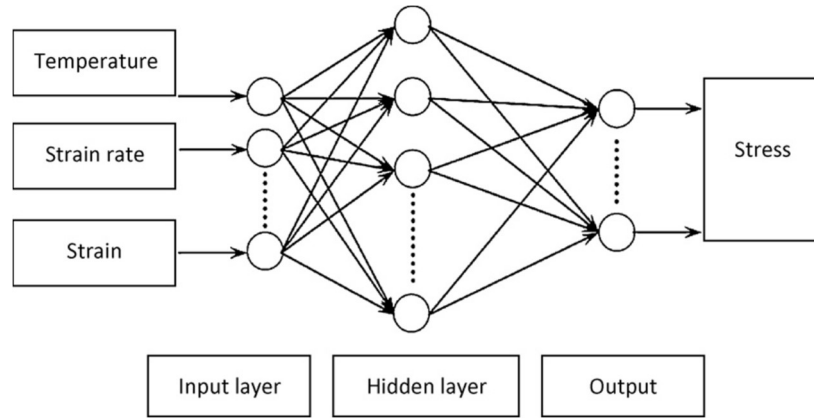
Figure II-19 Schematic structure of back propagation neural network [84]

The convergence criterion for the network is determined by the average root mean square (RMS) error between the designed and predicted output values

$$E_{RMS} = \frac{1}{N} \sum_{i=1}^{N} \sqrt{\frac{1}{P} \sum_{j=1}^{P} (d_{ji} - y_{ji})^2} \qquad (\text{II.29})$$

where E_{RMS} is the average *RMS*, N is the number of training or testing data, p is the number of variables in the output, $d_j(n)$ and $y_j(n)$ are the target output and network for neuron j, respectively. For the prediction of flow stress of the hot deformed material, strain, strain rate, and temperature are used as the inputs of the model, while the flow stress is the output of the model.

Lu et al. [84] used an AAN model to describe the effects of deformation temperature and strain rate on the flow behavior of an Al-Cu-Mg-Ag aluminum alloy. Shown in Figure II-20, a very high correlation between experimental and predicted results has been obtained, indicating the excellent predictability of the developed ANN model. The AAN model has also been used for the hot deformation prediction of steel [85, 86], and other aluminum alloys [87, 88].
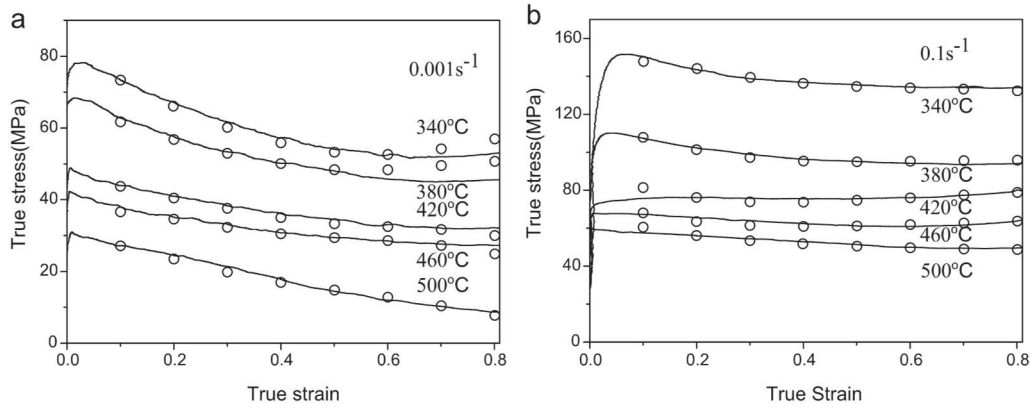
Figure II-20 Comparisons between the experimental (solid lines) and predicted (points) flow stress of Al-Cu-Mg-Ag alloy at (a) 0.001 s^{-1} and (b) 0.1 s^{-1} [84]

II.3 Yield criteria

To describe the viscoplastic behavior of a material in general stress state, the following three elements are needed:

(a) A yield criterion expressing a relationship between the stress components at the moment when plastic "yield" occurs

(b) An associated flow rule expressing the relationship between the components of the stress, the strain rate and the temperature

(c) A hardening rule describing the evolution of the initial yield stress during the forming process.

The transition from the elastic to the plastic state happens when the stress reaches the yield point of the material. A relationship between the principal stresses is needed specifying the conditions under which plastic flow occurs. Such a relationship, which is also called yield function, can be represented by

$$\Phi(\bar{\sigma}, Y) = \bar{\sigma} - Y \qquad (II.30)$$

where $\bar{\sigma}$ is the equivalent stress and Y is the yield stress obtained from a simple test (like tension, compression or torsion). All the points located in the inside of the surface ($\Phi < 0$) are related to an elastic state of the material. The points belonging to the surface ($\Phi = 0$) are related to a plastic state. The points located outside the surface ($\Phi > 0$) have no physical meaning.

Due to the crystallographic structure and the characteristics of the rolling process, sheet metals generally exhibits an anisotropy of mechanical properties. In this section, the anisotropy coefficients are first introduced, then two yield criteria for anisotropic materials are presented: Hill 48 yield criterion and BBC2003 yield criterion.

II.3.1 Anisotropy coefficients

The three principal directions of a sheet, namely the rolling direction, the transverse direction and the normal direction are respectively denoted by longitudinal direction (LD), transversal direction (TD) and normal direction (ND) (see Figure II-21).
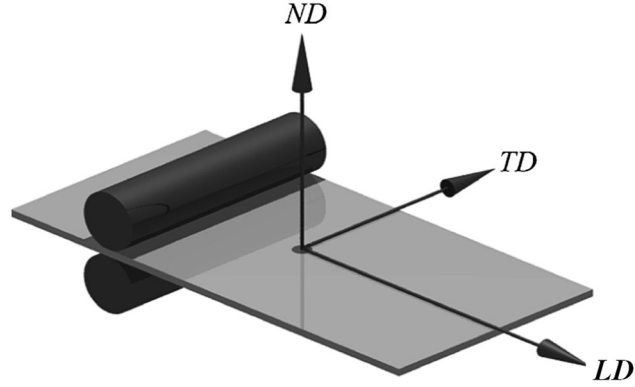
Figure II-21 Orthotropic axes of the rolled sheet metals: LD-longitudinal direction; TD-transversal direction and ND-normal direction

The variation of the plastic behavior with direction is assessed by Lankford parameter or anisotropy coefficient [89], which is determined by uniaxial tension tests on sheet specimens in the form of a strip. The anisotropy coefficient r is defined by

$$r = \frac{\varepsilon_{22}}{\varepsilon_{33}} \qquad (\text{II.31})$$

where ε_{22} and ε_{33} are the strains in the width and thickness directions, respectively. For these tests, the logarithmic transversal strain ε_{22} is calculated by

$$\varepsilon_{22} = \ln(\frac{w}{w_0}) \qquad (\text{II.32})$$

where w_0 and w are the initial and final width. Under the assumption of no volume change, the logarithmic normal strain ε_{33} along the normal direction is given by

$$\varepsilon_{33} = -\varepsilon_{11} - \varepsilon_{22} \qquad (\text{II.33})$$

And the logarithmic longitudinal strain coefficient ε_{11} can be easily obtained by

$$\varepsilon_{11} = \ln(\frac{l}{l_0}) \qquad (\text{II.34})$$

When the specimen inclines at the angle ϑ with respect to the rolling direction, the instantaneous coefficient of plastic anisotropy r_ϑ is defined as the ratio of the plastic strain rates associated to the width (inclined at the angle $\vartheta + 90°$ with respect to the rolling direction) $\dot{\varepsilon}_{\vartheta+90}$ and thickness, $\dot{\varepsilon}_{33}$

$$r_g = \frac{\dot{\varepsilon}_{g+90}}{\dot{\varepsilon}_{33}} \tag{II.35}$$

For metallic sheets, the Lankford coefficients are classically determined for three different directions (0°, 45° and 90°, respectively). The coefficient of normal anisotropy is obtained from

$$r_n = \frac{r_0 + 2r_{45} + r_{90}}{4} \tag{II.36}$$

This value has an important meaning in deep drawing, since it indicates the materials "resistance" to thinning. Also, a measure of the variation of anisotropy with the angle to the rolling direction is given by the planar anisotropy coefficient:

$$\Delta r = \frac{r_0 + r_{90} - 2r_{45}}{2} \tag{II.37}$$

In this study, the *r*-values have been determined at the axial logarithmic strain of 15%.

Experimental research has also proved that yield surfaces are not symmetric in the biaxial region [90]. To describe such a behavior, the coefficient of biaxial anisotropy has been defined by the ratio of the principal strains

$$r_b = \frac{\varepsilon_{22}}{\varepsilon_{11}} \tag{II.38}$$

A biaxial tensile machine can be used to obtain those principal strains.

II.3.2 Yield criteria

II.3.2.1 Hill 48 yield criterion

In 1948 Hill [91] proposed an anisotropic yield criterion by a quadratic function of the following type

$$\bar{\sigma}^2 = F(\sigma_{22} - \sigma_{33})^2 + G(\sigma_{33} - \sigma_{11})^2 + H(\sigma_{11} - \sigma_{22})^2 + 2L\sigma_{23}^2 + 2\hat{M}\sigma_{31}^2 + 2\hat{N}\sigma_{12}^2 \tag{II.39}$$

where F, G, H, L, $\hat{M}$ and $\hat{N}$ are anisotropic parameters. In the plane stress condition ($\sigma_{13} = \sigma_{23} = \sigma_{33} = 0$) the yield function is reduced to

$$\bar{\sigma}^2 = G\sigma_{11}^2 + F\sigma_{22}^2 + H(\sigma_{11} - \sigma_{22})^2 + 2\hat{N}\sigma_{12}^2 \tag{II.40}$$

With the condition of $G + H = 1$, only three independent anisotropic parameters F, G and $\hat{N}$ need to be identified. They can be represented by Lankford's coefficients

$$F = \frac{r_0}{r_{90}(r_0 + 1)}, \quad G = \frac{1}{r_0 + 1}, \quad \hat{N} = \frac{(1 + 2r_{45})(r_0 + r_{45})}{2r_{90}(r_0 + 1)} \tag{II.41}$$

This yield criterion has been applied for sheet metal forming with Gurson-Tvergaard-Needleman damage model due to its easy parameter identification and implementation [92]. However, there exists

some drawbacks for the yield criterion, such as it cannot represent the "anomalous behavior" observed by Woodthrope and Pearce [93] and "second order anomalous" behavior observed by Banabic et al [94].

II.3.2.2 *BBC2003 yield criterion*

BBC2003 is an advanced plane stress yield criterion, which is developed based on BBC2002, to describe the deformation behavior of orthotropic sheet metals [95]. The corresponding formulation is given by

$$\bar{\sigma} = [a(\Gamma + \Psi)^{2k} + a(\Gamma - \Psi)^{2k} + (1-a)(2\Lambda)^{2k}]^{\frac{1}{2k}} \tag{II.42}$$

where k and a are material parameters and yield function is convex when k is an positive integer and $0 \le a \le 1$, respectively. While Γ, Ψ and Λ are functions which are given as follows

$$\begin{aligned} \Gamma &= \frac{\sigma_{11} + M\sigma_{22}}{2} \\ \Psi &= \sqrt{\frac{(N\sigma_{11} - P\sigma_{22})^2}{4} + Q^2\sigma_{12}\sigma_{21}} \\ \Lambda &= \sqrt{\frac{(\hat{R}\sigma_{11} - S\sigma_{22})^2}{4} + \hat{T}^2\sigma_{12}\sigma_{21}} \end{aligned} \tag{II.43}$$

In above two equations, a, M, N, P, Q, $\hat{R}$, S and $\hat{T}$ are yield criterion constants. The integer parameter k is associated with the crystallographic structure of the material. Recommended value of the exponent is $k = 4$ for FCC materials [95].

Compared to Hill 48 yield criterion, BBC2003 yield criterion is more complex for parameter identification and implementation. However, the later yield criterion can describe accurately the yield surface and also give good predictions of the planar distribution of the uniaxial yield stress and uniaxial coefficient of plastic anisotropy [96]. And it has been successfully applied in the sheet metal forming for aluminum alloys, like AA3xxx [97, 98], AA5xxx [99] and AA6xxx [95] alloys .

II.4 Damage models

II.4.1 Foreword
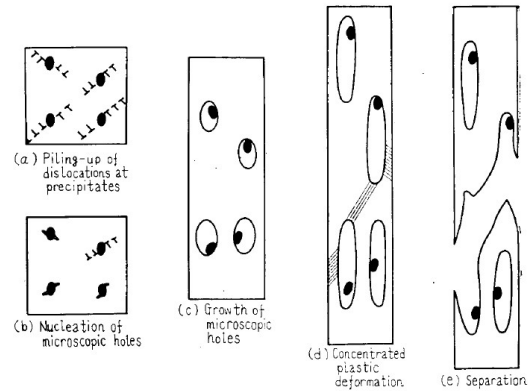
Figure II-22 Stages of ductile fracture [100]

For the design and simulation of sheet metal forming process, besides the consideration of the material rheological behavior, the ductile fracture (DF), which determines the upper limit to the forming process, is another important aspect to be considered. From a physical viewpoint, DF is generally described by the nucleation, and growth of voids that ultimately link to form cracks, shown in Figure II-22. A number of phenomenological or micro/macro-mechanical motivated ductile fracture criteria (DFCs) [101-105] have been developed for the prediction of DF initiation.

Compared with other models or indicators, like plastic instability theory and forming limit diagram (FLD), DFCs can consider stress and strain loading histories in plastic deformation. The early researches of McClintock [101] and Rice and Tracey [102] focused on the evolution of cylindrical and spherical holes in a ductile matrix. Their results show that the void volume fraction is governed by stress triaxiality. The void volume is included as an internal variable for the porous plasticity model proposed by Gurson [103], assuming that ductile fracture occurs as the void volume fraction reaches a critical threshold value. The original Gurson model has been repeatedly improved by considering the void coalescence [106], taking void shape into account [107], incorporating the influence of plastic anisotropy [108] and shear [109].

Criterion	Formula	Type
Rice-Tracey [102]	$\int_0^{\bar{\varepsilon}_f^P} \exp(\frac{3}{2}\frac{\sigma_m}{\bar{\sigma}})d\bar{\varepsilon}^P = C_1$	Uncoupled approach
Cockcroft-Latham [110]	$\int_0^{\bar{\varepsilon}_f^P} \langle \sigma_1 \rangle / \bar{\sigma} d\bar{\varepsilon}^P = C_2$	
Tresca [111]	$\tau_{\max} = \frac{\sigma_1 - \sigma_3}{2} = C_3$	
Oyane et al. [104]	$\int_0^{\bar{\varepsilon}_f^P} \langle 1 + A\frac{\sigma_m}{\bar{\sigma}} \rangle d\bar{\varepsilon}^P = C_4$	
Xue-Wierzbicki [112]	$\int_0^{\bar{\varepsilon}_f^P} \frac{d\bar{\varepsilon}^P}{F(\eta,\xi)} = 1$ $\bar{\varepsilon}_f^P = F(\eta,\xi) = c_1 \exp(-c_2\eta) - [c_1 \exp(-c_2\eta) - c_3 \exp(-c_4\eta)](1 - \xi^{1/n})^n$	
Modified Mohr-Coulomb [113]	$\int_0^{\bar{\varepsilon}_f^P} \frac{d\bar{\varepsilon}^P}{F(\eta,\xi)} = 1$ $\bar{\varepsilon}_f^P = F(\eta,\xi) = \{\frac{A}{c_2}[c_3 + \frac{\sqrt{3}}{2-\sqrt{3}}(c_\theta^{ax} - c_3)(\sec(\frac{\bar{\theta}\pi}{6})-1)]$ $[\sqrt{\frac{1+c_1^2}{3}}\cos(\frac{\bar{\theta}\pi}{6}) + c_1(\eta + \frac{1}{3}\sin(\frac{\bar{\theta}\pi}{6}))]\}^{-\frac{1}{n'}}$	
Gurson-Tvergaard-Needleman [106]	$\phi(\boldsymbol{\sigma}, \bar{\varepsilon}^P, f) = (\frac{\bar{\sigma}}{Y})^2 + 2q_1 f^* \cosh(\frac{3q_2\sigma_m}{2Y}) - 1 - q_1 f^{*2} = 0$	Coupled approach
CMD-based Lemaitre [105]	$\dot{D} = \frac{\partial F_D(Y,\bar{\varepsilon},D,...)}{\partial Y}\dot{\varepsilon}(1-D)$	

Table II-3 Brief summary of selected typical DFCs

An alternative method to predict ductile fracture is to adopt phenomenological models without modeling void nucleation and growth. It is assumed that the fracture occurs at a point of the body where a weighted measure of the accumulated plastic strain reaches a critical value. The typical example of the phenomenological damage model is the modified Mohr-Coulomb model [113] and Xue-Wierzbicki model [112].

In the view of the interactions between theoretical models and material responses, DFCs can also be classified into uncoupled and coupled categories. For the coupled approaches, the current flow stress is influenced by the progression of damage, while uncoupled approaches neglect the yield surface sensitivity to the damage evolution. Some typical DFCs are listed in Table II-3.

II.4.2 Uncoupled ductile fracture criteria

In the uncoupled DFC category, the damage accumulation is formulated empirically or semi-empirically with the following function in terms of variables such as the equivalent plastic strain, the deviatoric stress, and the hydrostatic stress

$$\int_0^{\overline{\varepsilon}_f^P} f(\boldsymbol{\sigma}, \overline{\varepsilon}^P) d\overline{\varepsilon}^P \geq C_C \tag{II.44}$$

where $\boldsymbol{\sigma}$, $\overline{\varepsilon}^P$ and $\overline{\varepsilon}_f^P$ are stress tensor, equivalent plastic strain and equivalent fracture strain, while C_C is the critical value. The uncoupled approach has been widely adopted due to its simple formulation and easy calibration. The Xue-Wierzbicki model and modified Mohr-Coulomb criterion are briefly introduced in this section.

Xue-Wierzbicki model

The Xue-Wierzbicki (X-W) [114] model has been developed based on the work of Bao and Wierzbicki [115] by taking the influence of Lode angle. Bao and Wierzbicki (B-W) carried out a series of experiments and found that the ductile fracture strain is not necessarily a monotonic function of triaxiality [115]. A three branch empirical fracture locus in the space of triaxiality and fracture strain has been proposed. In the high triaxiality domain, the main failure mode is void growth and linkage. For negative stress triaxialities, the fracture is governed by shear mode, while at low-stress triaxialities between above two regimes, the fracture may develop a combination of shear and void growth modes. The B-W model does not consider the effect of the Lode angle even though the experiments conducted by Bao and Wierzbicki are not all conducted in a plane stress state. Based on this work, the pure empirical Xue-Wierzbicki (X-W) model introduced the influence of the third deviatoric stress invariant J_3, which is related to the Lode angle parameter

$$\overline{\varepsilon}_f^P(\eta, \xi) = c_1 e^{-c_2 \eta} - (c_1 e^{-c_2 \eta} - c_3 e^{-c_4 \eta})(1 - \xi^{1/n})^n \tag{II.45}$$

where c_1, c_2, c_3 and c_4 are material constants, n is the hardening exponent, η and ξ are the stress triaxiality and the normalized third stress invariant which are defined respectively

$$\eta = \frac{-p}{\overline{\sigma}} = \frac{\sigma_m}{\overline{\sigma}} \tag{II.46}$$

$$\xi = \cos(3\theta) = \frac{27}{2} \frac{J_3}{\overline{\sigma}^3} \tag{II.47}$$

where p is the hydrostatic pressure, $\overline{\sigma}$ is the equivalent stress, J_3 is the third deviatoric stress invariant, and θ is the Lode angle.

The Xue-Wierzbicki model takes the exponential function of the Rice-Tracey model to describe the lower bound (plane strain condition) and upper bound (axial symmetric condition) of a 3D fracture locus.

Modified Mohr-Coulomb

The stress-based Mohr-Coulomb fracture criterion has been widely used in the modeling of brittle materials, such as soil, rock, and concrete [116]. This model postulates the following fracture criterion

$$(\tau + c_1 \sigma_n)_f = c_2 \tag{II.48}$$

where τ and σ_n are the shear and normal stresses, the constant c_1 is refered to as a friction coefficient and c_2 is shear resistance. In the case of $c_1 = 0$, the MC criterion reduces to the maximum shear stress criterion. Bai and Wierzbicki [113] extended this model to ductile materials. The resulting model is called the modified Mohr-Coulomb (MMC) criterion

$$\bar{\varepsilon}_f^P(\eta, \bar{\theta}) = \{\frac{A}{c_2}[c_3 + \frac{\sqrt{3}}{2-\sqrt{3}}(c_\theta^{ax} - c_3)(\sec(\frac{\bar{\theta}\pi}{6}) - 1)][\sqrt{\frac{1+c_1^2}{3}}\cos(\frac{\bar{\theta}\pi}{6}) + c_1(\eta + \frac{1}{3}\sin(\frac{\bar{\theta}\pi}{6}))]\}^{-\frac{1}{n}} \tag{II.49}$$

where A and n are two power hardening coefficients, c_1, c_2 and c_3 are three fracture parameters, $\bar{\theta}$ is the Lode angle parameter defined as

$$\bar{\theta} = 1 - \frac{6\theta}{\pi} = 1 - \frac{2}{\pi}\cos^{-1}(\xi) \tag{II.50}$$

c_θ^{ax} is defined by the following equation

$$c^{ax} = \begin{cases} 1 & for \; \bar{\theta} \geq 0 \\ c_\theta^c & for \; \bar{\theta} < 0 \end{cases} \tag{II.51}$$

where c_θ^c is the parameter considering the asymmetry of a fracture locus. If taking $c_\theta^c = 1$ for simplicity, the MMC model has only three parameters, and is referred as MMC3. Otherwise, there will be four parameters (c_1, c_2, c_θ^s and c_θ^c), which is called MMC4.

The MMC model has been extended to the anisotropic case by Luo et al. [117]. Another further modification of this model is to replace or link the parameter of c_θ^s with the power coefficient *m*, as shown in the Hosford yield function [118].

Improvement of uncoupled models

It is worth noticing that all the above-mentioned uncoupled criteria were developed to predict the evolution of ductile damage under cold deformation conditions, neglecting the influence of temperature and strain rate. However, complex geometries, which are difficult to form at room temperature, can only be formed at elevated temperatures. Both the constitutive behavior and ductile fracture behavior of material are influenced by forming temperature and strain rate [119]. The preliminary extension of cold deformation ductile fracture criterion is the classical Johnson-Cook model [120], which included temperature and strain rate effects by introducing two separate terms in its formulation. Based on the Johnson-Cook failure criterion, Arild et al. [121] studied the influence of strain rate, temperature, and triaxiality on the flow and fracture behaviors of an AA5083 alloy. However, as the Johnson-Cook

criterion does not consider deviatoric effects, its prediction is limited to a small positive range of triaxiality [112]. More recently, a new fracture model based on the Johnson-Cook criterion was developed by incorporating deviatoric effects to predict the ductility of Ti-6Al-4V sheets at different temperatures and strain rates [122]. Some studies have focused on the influence of temperature and strain rate on the ductile fracture of material with experimental identification at one stress state. Novella et al. [123] applied a modified Oyane-Sato model to predict the formability of AA6082-T6 rolling bars at elevated temperatures by using simple tensile tests. Khan and Liu [124] proposed a new isotropic fracture model which includes the effect of strain rate and temperature to predict fracture on shear deformation. Zhu et al. [125] used a simple process with compression tests to predict the fracture initiation in hot deformation. Few studies have been dedicated to the joint influence of the stress state, temperature and strain rate on damage.

II.4.3   Coupled ductile fracture criteria

Coupled ductile fracture criteria incorporate damage accumulation in constitutive equations. Those models allow the yield surface of the material to be changed by the damage-induced density change. Two typical coupled ductile fracture criteria are presented in this section.

Gurson-like models

In Gurson-like micromechanics-based criteria, the behavior of a material point is described by the pressure-sensitive plastic flow rule and the void volume fraction is an internal variable representing the progression of damage that interacts with the other state variables. In this section, the original Gurson model, Gurson-Tvergaard-Needleman (GNT) model [103, 106] and shear modified Gurson's models [109] are briefly introduced.

Gurson [103] proposed a constitutive model to describe the mechanical behavior of materials with micro-voids. The plastic flow potential of Gurson type model is

$$\phi = (\frac{\bar{\sigma}}{Y})^2 + 2f\cosh(\frac{3\sigma_m}{2Y}) - 1 - f^2 = 0 \qquad (\text{II.52})$$

where Y is the yield stress, σ_m is the mean stress, $\bar{\sigma}$ is the equivalent stress, f is the void volume fraction. When $f = 0$ (material is without damage), the above criterion corresponds to the classical von Mises criterion.

Tvergaard and Needleman [106] extended the original Gurson model by considering the void coalescence during deformation

$$\phi = (\frac{\bar{\sigma}}{Y})^2 + 2q_1 f^* \cosh(\frac{3q_2\sigma_m}{2Y}) - 1 - q_1 f^{*2} = 0 \qquad (\text{II.53})$$

where f^* is expressed as

$$f^* = \begin{cases} f & for \ f \le f_c \\ f_c + \dfrac{1/q_1 - f_c}{f_f - f_c}(f - f_c) & for \ f > f_c \end{cases} \qquad \text{(II.54)}$$

For the above two equations, q_1 and q_2 are parameters in the plastic flow potential, f_c is the critical value of void volume fraction at which the material stress carrying capacity starts to decay more rapidly, f_f corresponds to the condition when the material totally loses the stress-carrying capacity.

The material point is assumed to fail when volume fraction of micro-voids f increases from the initial value f_0 to f_f. The original Gurson model only considers void growth as the failure mechanism. The void growth rate is a function of the plastic strain rate and can be expressed by

$$\dot{f}_{growth} = (1 - f)tr(\dot{\varepsilon}^{\prime}) \qquad \text{(II.55)}$$

where $\dot{\varepsilon}^{\prime}$ is the plastic strain rate tensor. Tvergaard and Needleman [106] introduced another failure mechanism called the micro-void nucleation due to plastic deformation

$$\dot{f}_{nucleation} = \frac{f_N}{S_N \sqrt{2\pi}} \exp[-\frac{1}{2}(\frac{\bar{\varepsilon}^P - \bar{\varepsilon}_N^P}{S_N})]\dot{\bar{\varepsilon}}^P \qquad \text{(II.56)}$$

where f_N is the volume fraction of void nucleating particles, $\bar{\varepsilon}_N^P$ and S_N are the mean strain and standard deviation for nucleation, respectively. The evolution of total volume fraction of voids due to plastic deformation can be represented by

$$\dot{f} = \dot{f}_{growth} + \dot{f}_{nucleation} \qquad \text{(II.57)}$$

Nahshon and Hutchinson [109] found one limitation of the original Gurson's model to be the sole consideration of stress triaxiality. They introduce another failure mechanism to describe the micro-void shear localization

$$\dot{f}_{shear} = k_w f(1 - \xi)\dot{\bar{\varepsilon}}^P \qquad \text{(II.58)}$$

where k_w is a new material coefficient. Assuming the three micro-mechanisms to be independent, the governing equation for the total volume fraction of micro-voids is

$$\dot{f} = \dot{f}_{growth} + \dot{f}_{nucleation} + \dot{f}_{shear} \qquad \text{(II.59)}$$

CMD-based Lemaitre

The Lemaitre model is derived from the general framework of continuum damage mechanics. The starting point of this model is the definition of a damage state variable D, which is assumed to represent the ratio between the damaged area S_D and the total surface S of any cross-section. Due to the effect of damage, the effective stress can be defined as

$$\sigma^{\prime} = \frac{\sigma}{1 - D} \qquad \text{(II.60)}$$

where σ' is the effective stress tensor, σ is the actual stress tensor. In the constitutive equations, the effective stress is used instead of Cauchy stress to describe the damage impact on the macroscopic behavior of materials.

Lemaitre [126] defined the dissipation potential with the additive function of the plastic potential and damage dissipative potential. The latter is defined as

$$F_D = \frac{r}{(r+1)(1-D)}(\frac{Y}{r})^{s+1} \tag{II.61}$$

where r and s are the material parameters, and Y is energy release rate which is defined by

$$Y = \frac{\bar{\sigma}^2}{2E(1-D)^2}[\frac{2}{3}(1+v)+3(1-2v)(\frac{-p}{\bar{\sigma}})^2] \tag{II.62}$$

where $\bar{\sigma}$ is the equivalent stress, E is the Young's modulus, v is the Poisson's ratio. Finally, the damage evolution rule is

$$\dot{D} = \dot{\gamma}\frac{\partial F_D}{\partial Y} = \frac{\dot{\gamma}}{1-D}(\frac{Y}{r})^s = \dot{\bar{\varepsilon}}^P(\frac{Y}{r})^s \tag{II.63}$$

where $\dot{\gamma}$ is the plastic multiplier, which can be deduced from the equivalent plastic strain rate as $\dot{\gamma} = \dot{\bar{\varepsilon}}^P(1-D)$.

In the above equation, the term $-p/\bar{\sigma}$ refers to the stress triaxiality. It is used in the definition of the damage strain release rate Y, which introduces the influence of the stress triaxiality in the damage evolution rule. However, another important factor, the Lode parameter, is not considered in this conventional Lemaitre model, leading to the inaccurate prediction for complex stress states. For this reason, the Lemaitre model has been improved by incorporating the influence of the Lode angle parameter in the formulation of Cao et al. [127]. They modified the damage dissipative potential as

$$F_D = \frac{r}{(r+1)(1-D)}(\frac{Y}{r})^{s+1}\frac{1}{\alpha_1 + \alpha_2\bar{\theta}^2} \tag{II.64}$$

where α_1 and α_2 are two positive parameters, $\bar{\theta}$ is the Lode angle parameter. With the modified potential, the damage evolution rule for the Lemaitre model becomes

$$\dot{D} = \dot{\gamma}\frac{\partial F_D}{\partial Y} = \dot{\bar{\varepsilon}}^P(\frac{Y}{r})^s\frac{1}{\alpha_1 + \alpha_2\bar{\theta}^2} \tag{II.65}$$

Another similar modification which includes the influence of the Lode angle parameter can be seen in [128].

II.5 Mechanical behavior of Al-Mg alloys at elevated temperatures

For the continuing trend toward weight reduction of vehicles, high-strength aluminum alloys have been increasingly used for vehicle construction. In particular, aluminum-magnesium (Al-Mg) alloy sheets are widely used in the automotive and shipbuilding industries, especially for outer panels, due to their excellent properties of high strength, corrosion resistance, and weldability. However, the relatively low formability at room temperature compared to steel sheets limits their applications. Moreover, Al-Mg alloy sheets often exhibit stretcher-strain (St-St) marks after metal forming operations [129]. Figure II-23 shows the particular conditions of strain rate and temperature leading to the appearance of stretcher-strain marks. It can be seen that no St-St mark appears in the hot deformation conditions. Thus, there is some interest in forming of Al-Mg sheet alloys at elevated temperatures. In this section, the review will be focused on the mechanical and microstructure properties of Al-Mg alloys at elevated temperatures.

As we have mentioned before, forming processes at elevated temperatures can be divided into two categories according to the temperature range: warm forming and hot forming. The boundary temperature for the two forming process is the recrystallization temperature, which is about 320°C for Al-Mg alloys. The behavior of Al-Mg alloys in both the warm and hot forming conditions is discussed in the following.
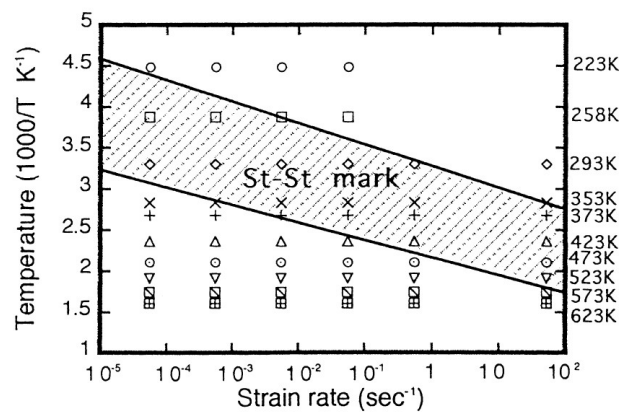
Figure II-23 Conditions of temperature and strain rate for the appearance of St-St marks [129]

II.5.1   Al-Mg alloys behavior in warm forming conditions

In the early times, many studies have focused on the formability of Al-Mg alloys at warm temperatures. Ayres and Robert [130] studied the uniaxial ductility of Al-Mg alloy sheets from 298 to 573K for a wide range of strain rates. Ayres and Wenner [131] also conducted research on the effect of strain and strain hardening on the punch stretching of the same alloy at two warm temperatures (403 and 473 K). Tetsuo et al. [129, 132] investigated the influence of both temperature and strain rate on the uniaxial and biaxial ductility of 5083-O Al-Mg alloy sheets from room temperature to 523 K. To discuss

the strain and strain rate hardening effects, the strain hardening exponent, n-value, and the strain rate sensitivity exponent, m-value, were determined from uniaxial tensile tests at various temperatures and strain rates. The corresponding results are shown in Figure II-24. In general, higher n- and m-values result in larger forming limit strains. At 573 K, the m-value is strongly influenced by the strain rate, with variations from 0.1 to 0.4 corresponding to strain rates of $10^{-1} \sim 10^{-4}$ s^{-1}. The n-value is rather small and does not change much with the strain rate. However, when the temperature is below 473 K, the m-value is rather insensitive to the strain rate, while n-value is influenced by the strain rate. We can see that the improvement of formability of Al-Mg at 573 K at low forming speed is due to the high strain rate sensitivity value (m-value). Below 475 K, the formability is also strongly affected by the strain hardening (n-value).

All those experiments showed the following characteristics of Al-Mg alloys:

- The ductility becomes higher with an increasing temperature and with a decreasing strain rate
- Some of the alloys exhibit superplasticity under certain conditions of elevated temperature and low strain rate
- The strain-rate sensitivity (m-value) is central to stretch-formability, since higher the m-value, the higher the ductility and lower the flow stress

(a)   (b)
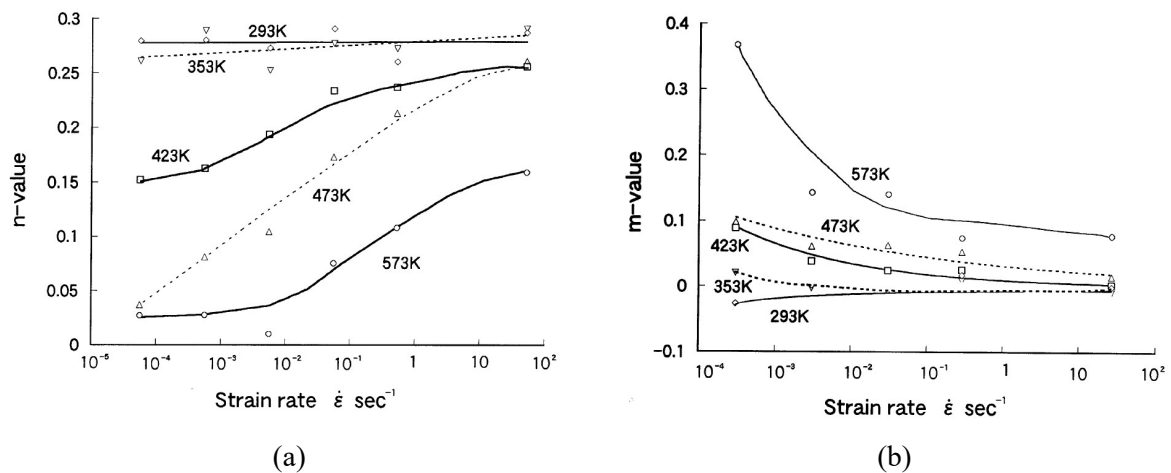
Figure II-24 Effect of strain rate and temperature on (a) strain hardening (n-value) and (b) strain rate hardening (m-value) of 5083-O Al-Mg alloy sheet in uniaxial tension tests [129]

II.5.2 Al-Mg alloys behavior in hot forming conditions

Increasing the forming temperature allows increasing augmenting the forming limit of aluminum alloys. In comparison with warm forming, the deformation mechanisms for hot forming are more complex. In the superplastic range, the main deformation mechanism is grain boundary sliding (GBS) and the strain rate sensitivity value m is above 0.5. The temperature domain in which superplasticity of the 5083 Al alloy can be obtained is generally between 500 and 560°C with optimum strain rates ranging from 10^{-4} s^{-1} to 10^{-3} s^{-1} [133-135]. Martin et al. [136] investigated the evolution of microstructure and

texture during high-temperature deformation of Al-Mg alloy. They found that both grain boundary sliding (GBS) and dislocation creep (DC) played an important role in the deformation. At low strain rates, the predominance mechanism is GBS while DC plays an important role at high strain rates and continuous recrystallization takes place during the deformation. Generally, as-received Al-Mg alloy sheet exhibits distinct deformation textures, due to the rolling in the final stage of the processing. Heating of the sheet prior to forming can produce a fine recrystallized microstructure. McNelley et al. [137] experimentally studied the influence of annealing on the texture evolution of AA5083 alloy. Shown in Figure II-25 (a), the as-received AA5083 alloy exhibited the discrete orientation along the rolling direction. After annealing, the microstructure exhibited nearly equiaxed grains (Figure II-25 (b)). It was also observed that there were no further discernable changes in texture noted for annealing treatments with durations up to 3600 seconds. Similar microstructural evolutions of an AA5083 alloy were also observed by Dharmendra [138].

(a)   (b)
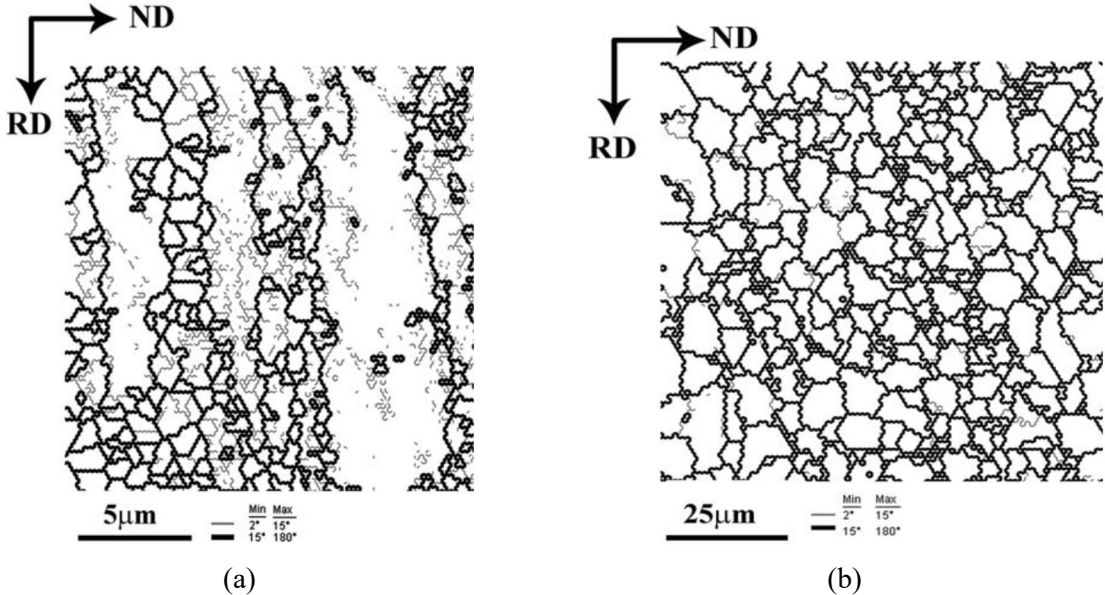
Figure II-25 The grain map of the AA5083 alloy at different state (a) as received type and (b) after heating for 360 s at 450 $^\circ$C [137]

The hot deformation behavior of Al-Mg sheet alloys has been studied for many years [137, 139-143]. Figure II-26 shows the typical flow curves in the hot deformation conditions for a fixed temperature [137] and a fixed strain rate [139]. The discontinuous yielding phenomenon, in which the flow stress decreased rapidly and eventually reaches a steady-state, occurred in the certain range of strain rates and temperatures. When the deformation temperature is at 450°C, this phenomenon only appeared at high strain rates. While it can be observed for the all the researched temperatures at the strain rate of 0.1 s^{-1} (Figure II-26(b)). Thus, the discontinuous yielding phenomenon is largely influenced by the imposed strain rate. This phenomenon is related to the rapid generation of mobile dislocations from grain boundary sources, leading to hot deformation proceeding from the grain boundary region inward. The stable flow in the large strain is associated with dynamic recovery and dynamic recrystallization.
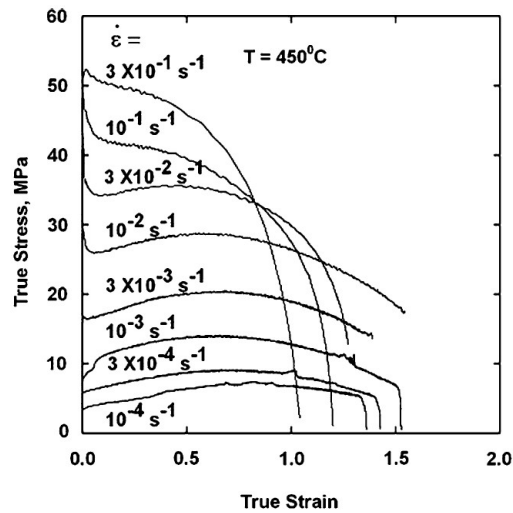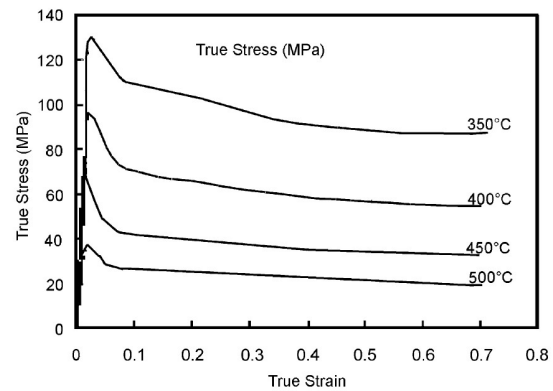
Figure II-26 (a) Flow curves of superplastic AA5083 alloy at various strain rates and 450 °C [137]; (b) Flow curves of Al-5 wt.% Mg alloy at different temperatures and a strain rate of 0.1 s^{-1} [139]

II.6 Summary

In this literature review, the sheet metal forming techniques, which are commonly used in the industry, have been presented. Generally, in order to obtain complex deep parts, superplastic forming (SPF) has often been adopted. However, long cycle times and high requirements for the as-received material limit its wide application in the industry. Quick plastic deformation (QPF) is another forming method at high temperatures, which uses higher forming strain rates than SPF and does not allow obtaining very complex shapes. The deformation mechanisms for SPF and QPF are different. For SPF, the main deformation mechanism is grain switching and grain boundary sliding, while the strain hardening or softening mechanisms are dominant for QPF. In order to obtain a complex shape without reducing part quality while increasing forming efficiency, one of the possible method consists in chaining those two different forming processes. At first, QPF is used to form the part to a certain deformation at high strain rate, then SPF techniques are adopted to obtain the final shape by matching the die. With the consideration of QPF and SPF techniques, the strain rate range for characterization of the material behavior is chosen from 0.0001 s^{-1} to 0.1 s^{-1}. While the temperatures are selected between 623 K and 723 K, which are in the hot forming range.

A proper description of the material mechanical behavior is required for the simulation of hot metal forming. The commonly used constitutive models have been briefly described. For our thesis, after characterization of our researched material, some of these constitutive models will be used or improved to describe our material behavior. The ductile fracture is another aspect that should be accounted for during hot temperature metal forming. The modified Mohr-Coulomb (MMC) model has been widely used to predict the ductile fracture at cold deformation by putting the fracture strain as the function of

triaxiality and Lode angle. Normally, the strain rate sensitivity for the ductile fracture at room temperature is neglected. For hot deformation, the influence of strain rate and temperature on the ductile fracture is however of a big importance. The first damage model considering both the influence of strain rate and temperature is the empirical Johnson-Cook model. It is valid only for large triaxiality ratios and does not take the Lode angle into account. The choice of damage model should depend on the experimental results. This will be discussed in Chapter IV.

Chapter III.
Experimental investigation of the high temperature behavior of the AA5383 alloy

In this chapter, the material AA5383 alloy used throughout this study is microstructurally and mechanically characterized. In the first part, the alloy employed as a work piece material is identified and introduced. Optical microscopy and X-ray diffraction techniques are used to analyze the main microstructural features of the AA5383 alloy. The impact of the initial heat treatment on the microstructure is also discussed. In the second part, the mechanical behavior of the alloy is characterized from different experimental tests in the ranges of 623~723 K and 0.0001~0.1 s^{-1}. The objective is to build an experimental database that will later allow identifying a yield function, a viscoplastic flow rule and a damage model. To study the flow behavior, uniaxial tensile tests for different loading directions, different temperatures and different strain rates as well as free bulging tests are performed. For the characterization of the damage behavior, different type of tests (notched tension, shear and free bulging tests) are carried out to study the effect of stress state, temperature and strain rate on the ductility. The experimental procedures used for the different tests are presented in this chapter. The experimental results are also exposed and briefly discussed.

III.1 Metallurgical characteristics of the AA5383 alloy

Aluminum alloys with magnesium as the major alloying element are widely used in the automotive and marine industries due to their corrosion resistance, high strength to weight ratio and important ductility. For marine applications, the most commonly used wrought aluminum alloys are 5083/5383 alloys. The present study focuses on the wrought aluminum alloy AA5383, whose chemical composition is given in Table III-1.

Mg(%)	Mn(%)	Fe(%)	Cr(%)	Si(%)	Cr(%)	Cu(%)	Zn(%)	Al
4.91	0.80	0.17	0.12	0.05	0.12	0.06	0.04	balance

Table III-1 Chemical composition of AA 5383 alloy (wt. %)

III.1.1 As-received material

The studied alloy has been received in the form of 3.2 mm thick sheets. To observe the initial microstructure, some samples have been cut, grinded and polished. An electro-chemical etching method (with boric acid at the voltage of 30 V for 50 s) has then been used to reveal the microstructure. According to metallographic observations (Figure III-1), because of the rolling process, the initial grains are elongated along the rolling direction.
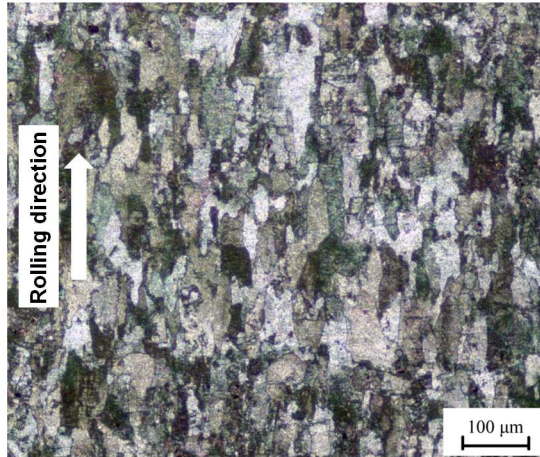
Figure III-1 Metallographic observation of the as-received AA5383 alloy

Also, to investigate crystallographic texture, which is likely to be an important source of anisotropy, some X-Ray Diffraction (XRD) analyses have been carried out. More specifically, a BRUKER Discover D8 diffractometer, equipped with a copper anode, has been used to measure the {111}, {002}, {220} and {311} pole figures of the as-received AA5383 alloy. The orientation density function has then been estimated from pole figures with the harmonic method [144]. The corresponding inverse pole figures are plotted for the three principal directions (i.e. RD, TD and ND) in Figure III-2. ND poles (red color) are preferably located close to the [110] direction while RD poles are aligned with the [112] direction of the standard stereographic triangle. The above features indicate that the as-received material displays a brass-type texture [145].

| (a) | (b) | (c) |
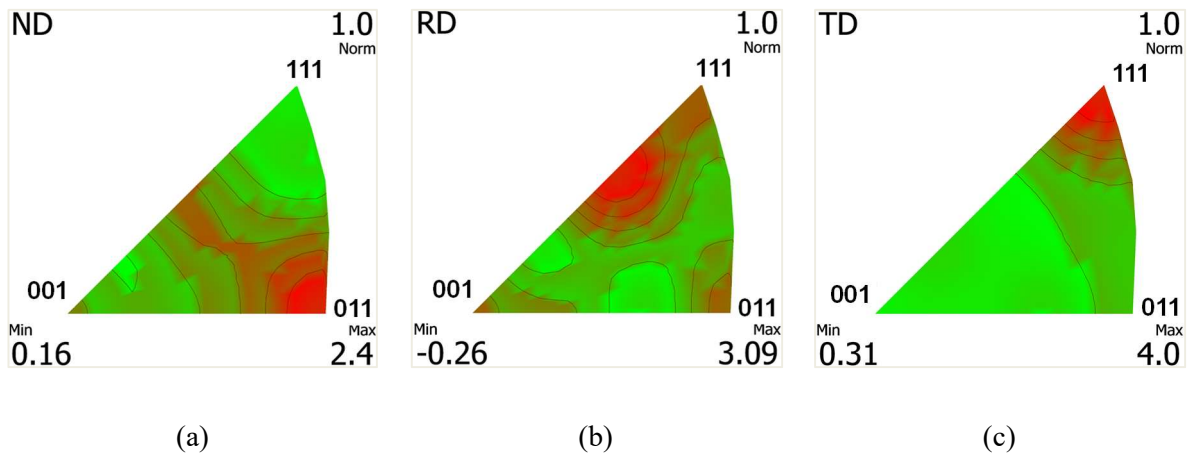
Figure III-2 Inverse pole figures of as-received material for (a) normal direction; (b) rolling direction and (c) transverse direction

III.1.2 Heat-treated material

In order to increase ductility, the AA5383 alloy has been heat-treated at 623 K and the duration has been varied from 5 min to 60 min. As illustrated by Figure III-3 (a), even when the heat treatment time

is only 5 min, significant microstructural changes are observed. Specifically, in comparison with the as-received condition, grains are smaller and equiaxed, rather than elongated. The average grain size after the heat treatment is about 19 μm. When the annealing time is further increased, no major microstructural transformation is observed (Figure III-3 (b-c)). A similar phenomenon has been reported for other AA5XXX alloys [137]. In the following, all specimens have been annealed at 623 K during 5 min prior to deformation.
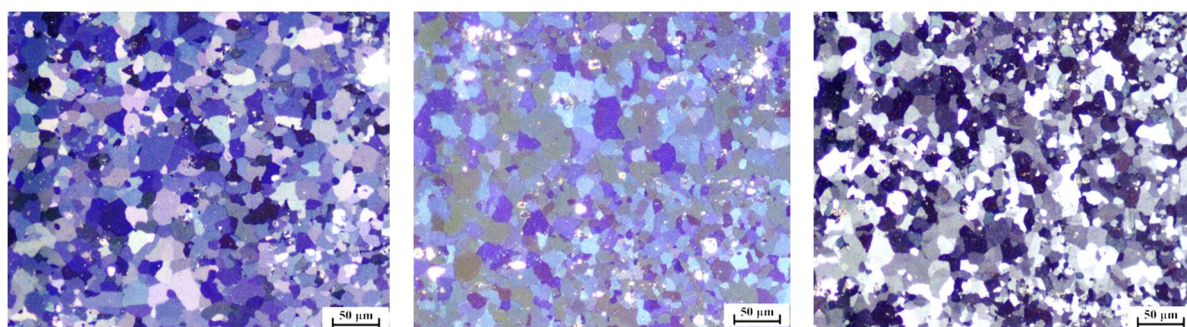
| (a) | (b) | (c) |

Figure III-3 Metallographic observations of the AA5383 alloy after heat treatment at 623 K for (a) 5 min; (b) 30 min and (c) 60 min

Using the same experimental procedure as before, the crystallographic texture of the heat-treated material (at 623 K for 5 min) has been evaluated with XRD techniques. The corresponding inverse pole figures are shown in Figure III-4. According to the results, because of recrystallization, the texture is less pronounced, the maximum and minimum pole densities being closer to unity. The annealing treatment is therefore expected to reduce plastic deformation anisotropy.
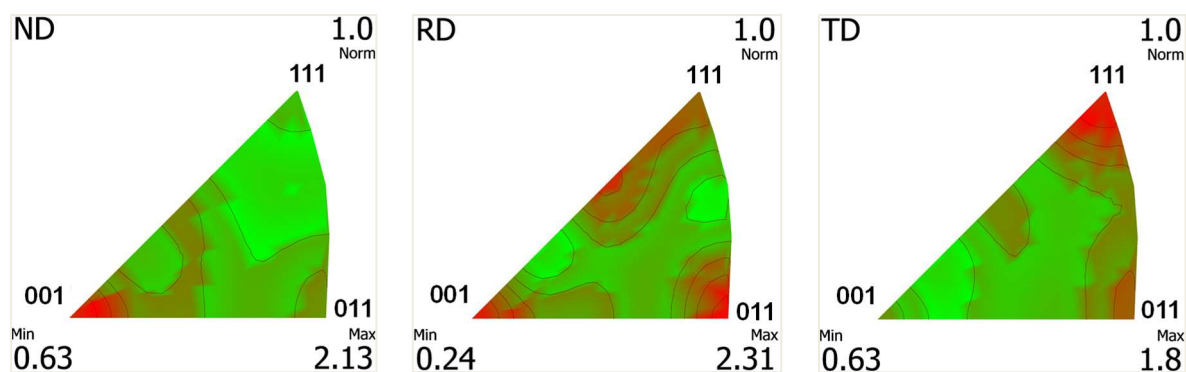
| (a) | (b) | (c) |

Figure III-4 Inverse pole figures of material heat treated at 623 K for 5 min for (a) normal direction; (b) rolling direction and (c) transversal direction

III.2 Experimental procedures

To evaluate the high temperature behavior of the AA5383 alloy, different experimental tests have been conducted. The objective of these tests is twofold. First, some uniaxial and biaxial tension tests have been carried out to evaluate the viscoplastic flow behavior of the AA5383 alloy. The corresponding results will later be used to select (i) a yield function, (ii) a viscoplastic flow rule and (iii) a hardening rule. Secondly, some complex-shaped specimens have been submitted to different loading conditions to evaluate the fracture behavior of the AA5383 alloy. Such tests will allow identifying the parameters of a fracture criterion. In this section, the specimen geometries and the experimental devices are briefly described.

III.2.1 Specimen geometries

In order to characterize the flow behavior and fracture response of the material over a wide range of temperatures and strain rates, different specimens have been machined from the AA5383 sheet, see Figure III-5:

- Uniaxial Tension (UT) specimens with a 78.14 mm long and 12.5 mm wide gauge section to characterize the flow behavior as well as the fracture behavior under uniaxial tension. The loading direction is aligned with an angle of either 0° (UT0), 45° (UT45) or 90° (UT90) with respect to rolling direction.
- Eccentric shear (SH) specimens with two asymmetric notches to characterize the fracture behavior for a purely deviatoric stress state. The gauge section shape is developed based on the work of Peirs et al. [146] to ensure shear deformation. The loading direction coincides with the rolling direction.
- Notched Tension (NT) specimens to characterize the fracture behavior at different triaxiality values. NT specimens have been machined with a minimum section width of 10 mm and different circular cut-out radii: R = 20 mm (NT20); R = 10 mm (NT10); R = 5 mm (NT5) and R = 2 mm (NT2). The loading direction coincides with the rolling direction.
- Free Bulging (FB) flanges of 290 mm diameter to characterize the plastic and fracture response for biaxial stress state.
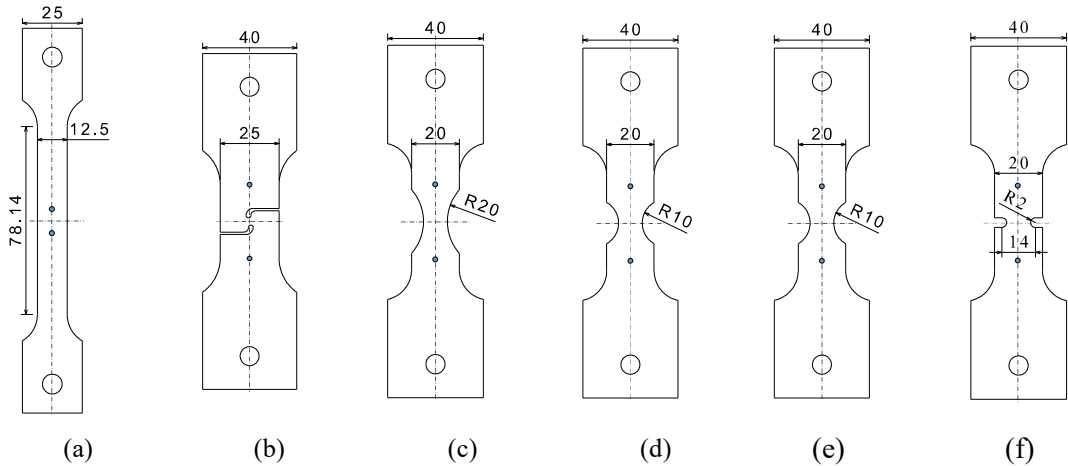
Figure III-5 Specimen geometries for testing: (a) UT specimen; (b) SH specimen; (c) NT20 specimen; (d) NT10 specimen; (e) NT5 specimen and (f) NT2 specimen. Blue slid dots highlight the position of the extensometer for relative displacement measurement

III.2.2 Testing machines

III.2.2.1 GLEEBLE machine

In the present work, the tension experiments have been performed with a GLEEBLE 3500 machine (Figure III-6(a)). The maximum force capacity is 100 kN for both tension and compression and the maximum velocity is 1 m/s. A schematic diagram of the GLEEBLE 3500 machine is shown in Figure III-6(b). The specimen is fixed between two copper jaws, which are cooled down by the circulation of water. Specimens are heated with the Joule effect, which allows high heating rates as well as a good homogeneity of the temperature in the center of the specimen.
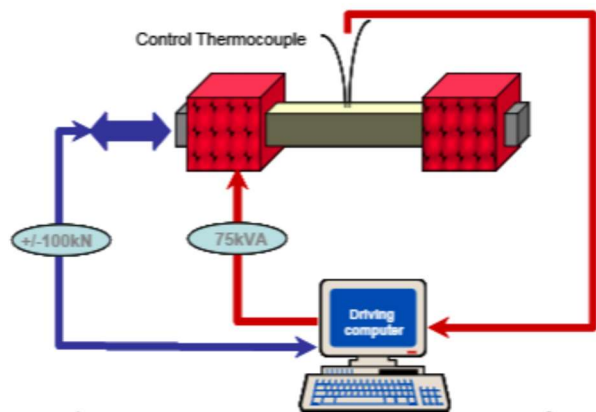
Figure III-6 (a) Gleeble 3500 and (b) schematic diagram

Flat specimens are attached to the copper jaws. A U-shaped part is positioned on the back of each copper jaw to keep it in the right position, particularly during the heating stage. A type K thermocouple,

which consists of two 0.2 mm diameter wires, is welded to the specimen center to control the temperature (Figure III-7). All the tests are carried out in a vacuum chamber in order to avoid the oxidation of the specimen. The driving computer allows controlling the machine and recording the experimental data.
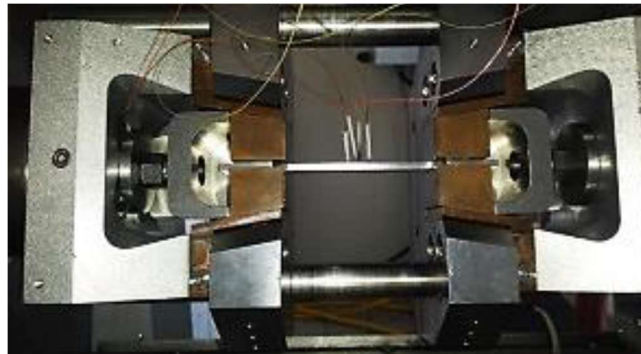
Figure III-7 Fixed position of the specimen in the GLEEBLE

The longitudinal elongation Δl is measured by a LVDT extensometer (Figure III-8 (a)) that is placed at the center of specimen. The extensometer consists of two arms that can move relatively to each other during a deformation process. Each arm is composed of a straight alumina stem and an angled quartz stem to realize the measurements up to very high temperatures (about 1300°C). The extensometer is fixed at a place such that each arm is at the same distance from the center of the specimen. The error of this measuring instrument is about 2 μm.

The width reduction Δw of tension specimens is measured by using a dilatometer type "C Gauge" extensometer (Figure III-8 (b)), which is placed at the center of the specimen.

(a)   (b)

Figure III-8 (a) LVDT Extensometer and (b) C gauge Extensometer

III.2.2.2   Gas forming machine

A gas forming machine is used for the evaluation of the behavior of the aluminum alloy under biaxial stress state. The gas forming machine, which is shown in Figure III-9 (a), has been developed at the LAMPA.
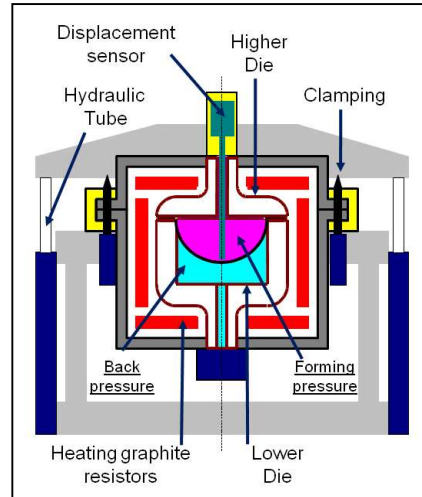
<div align="center">(a)   (b)</div>

Figure III-9 (a) Gas forming machine at LAMPA and (b) pressure scheme

To perform a biaxial test, the specimen is first clamped between the blank holder and the matrix. Using graphite resistors, the temperature of the tooling and the specimen is then increased to the deformation temperature, which is controlled with a K-type thermocouple placed at the center of the specimen. The specimen is finally inflated by injecting argon gas. The input pressure is controlled either according to the height of the deformed specimen or according to the forming time. The height of the dome apex is measured using a displacement sensor, which is located outside of the hot zone. A ceramic bar, attached to the end of the sensor, is used to measure the displacement of the bottom pole of the specimen by the direct contact.

The characteristics of the machine are: a deformation temperature comprised in 300ºC and 1100ºC, a maximum pressure of 120 bars, a maximum displacement for the sensor of 200 mm. The upper die has a cylindrical geometry with an aperture radius of 145 mm. The die entry radius is 5 mm and 200 mm deep. The initial diameter of the specimen is 290 mm and the diameter of the deformed zone is 200 mm. The dome displacement of the deformed part is limited to 100 mm in order to be moved out easily. Generally, the sheet can have the fracture before reaching this dome displacement.

III.3 Flow behavior of the AA5383 alloy

III.3.1 Uniaxial tension

III.3.1.1 Interpretation of tension tests

The GLEEBLE machine is used for the characterization of flow behavior under uniaxial tension. During uniaxial tensile tests, the cross-head velocity is controlled to obtain a constant logarithmic strain rate $d\varepsilon_{11} / dt$:

$$d\varepsilon_{11} / dt = dl / dt / l \tag{III.1}$$

where l is the gauge length, ε_{11} is the axial logarithmic strain. According to the above equation, the strain rate is kept constant by gradually changing the cross-head velocity during tensile tests. In the GLEEBLE machine, the axial force and the elongation of the gauge length can be measured; the axial Cauchy stress σ and the axial logarithmic strain ε_{11} can be evaluated from:

$$\varepsilon_{11} = \ln(\frac{l}{l_0}) \tag{III.2}$$

$$\sigma = \frac{F}{A_0}.\frac{l}{l_0} \tag{III.3}$$

where l_0 and A_0 are the initial gauge length and cross-section area, while F is the current axial force. It should be noticed that, for the evaluation of the axial Cauchy stress, the volume is assumed to be constant.

III.3.1.2 Impact of strain rate and temperatures

In order to investigate the impact of temperature and strain rate on the flow behavior, some UT tests along the rolling direction have been carried out at different temperatures (623, 673 and 723 K) and strain rates (0.0001, 0.001, 0.01, 0.1 s^{-1}). All the tests have been stopped at the axial logarithmic strain of 0.6. The testing conditions have been listed in Table III-2. The initial axial gauge length for those UT tests is set as 10 mm. To verify the homogeneity of temperature in the gauge area, the temperature of 5 mm from the center position is also measured. As shown in Figure III-10, the maximum temperature difference during the deformation in the gauge length is less than 4 K, indicating the homogeneity of temperature.

T $\quad\quad$ $\dot{\bar{\varepsilon}}^P$ Deg	0.0001 s^{-1}	0.001 s^{-1}	0.01 s^{-1}	0.1 s^{-1}
623 K	0°	0°	0°	0°
673 K	0°	0°	0°	0°
723 K	0°	0°	0°	0°

Table III-2 Testing conditions for UT test along the rolling direction
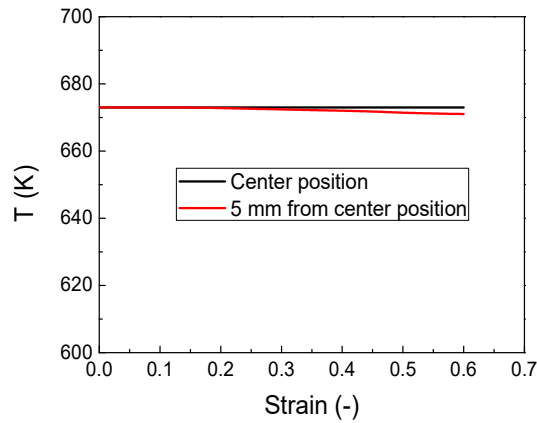
Figure III-10 Temperature evolution for uniaxial tension test

For each condition, three tests have been performed. As there exits high repeatability, only one curve is presented for each testing condition. The corresponding true axial stress-strain curves are shown in Figure III-11. According to the results, the influence of temperature and strain rate on the flow behavior is significant. Generally, both the yield stress and the steady stress increase with an increasing strain rate and a decreasing temperature. A yield drop phenomenon, which is particularly visible for high strain rates, is sometimes observed. This phenomenon can be explained by the sudden increase of the dislocation density at the beginning of deformation. Also, whatever the deformation temperature is, a hardening behavior is observed at low strain rates while softening is predominant for high strain rates.
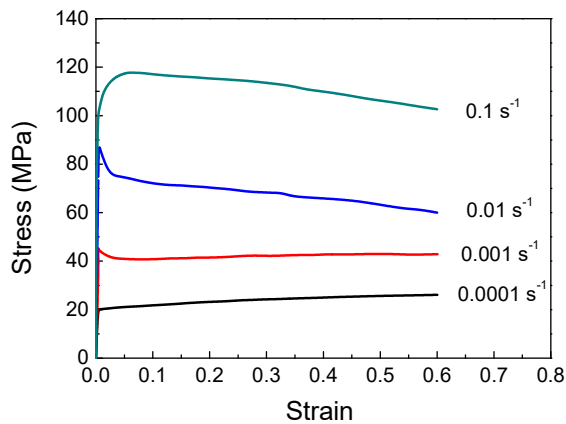
(a)
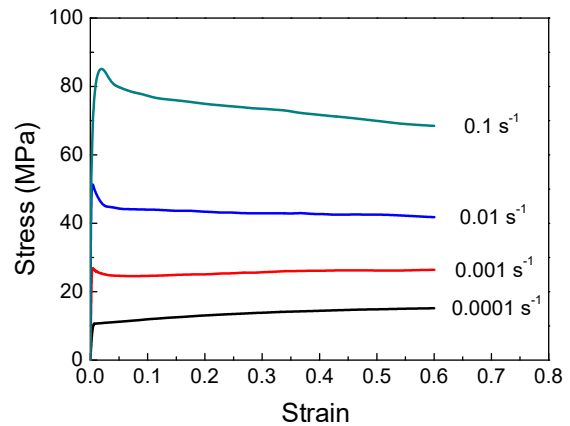
(b)
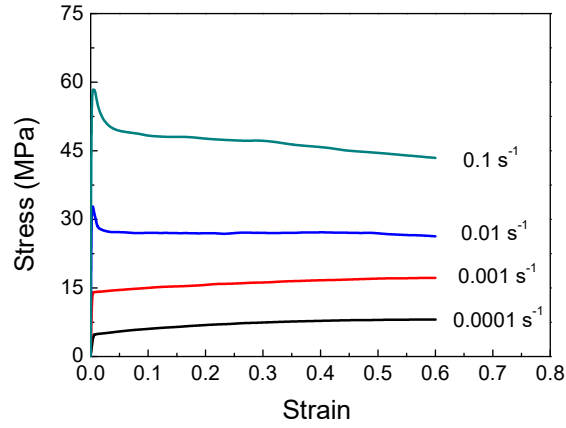
(c)

Figure III-11 Stress-strain curves obtained from UT tests at (a) 623 K; (b) 673 K and (c) 723 K

To study the influence of hot deformation on the evolution of microstructure and texture, some UT tests have been performed at two different strain rates (0.1 s^{-1} and 0.0001 s^{-1}) and three different temperatures (623 K, 673 K and 723 K) and interrupted for an axial logarithmic strain of 50%. In general, the microstructure after hot deformation consists of fine grains without obvious elongation (Figure III-12), indicating that dynamic recrystallization (DRX) occurs during hot deformation. It is generally established that the softening mechanism of alloys during the high temperature deformation is related to the Zener-Hollomon parameter [51, 56, 63, 147]

$$Z = \dot{\bar{\varepsilon}}^P \exp(\frac{Q}{RT}) \tag{III.4}$$

Liu et al. [148] indicated that DRX is more likely to occur for materials with high Z values. This tendency has been reported for the AA2195 alloy under the hot compression deformation [149]. In the present case, this can explain the fact that the AA5383 alloy deformed at 623 K and 0.1 s^{-1} exhibits a larger amount of small recrystallized grains.
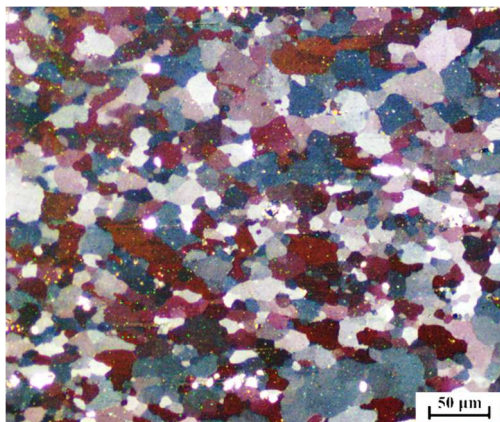
(a)
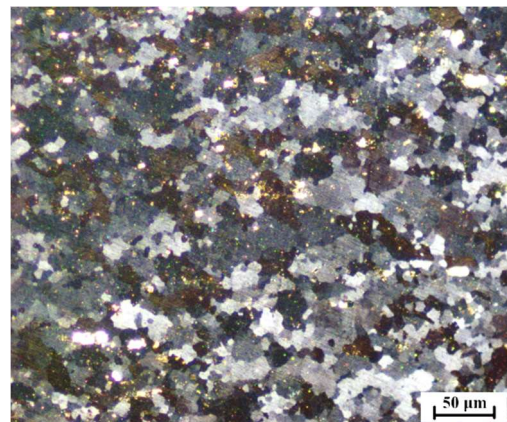
(b)
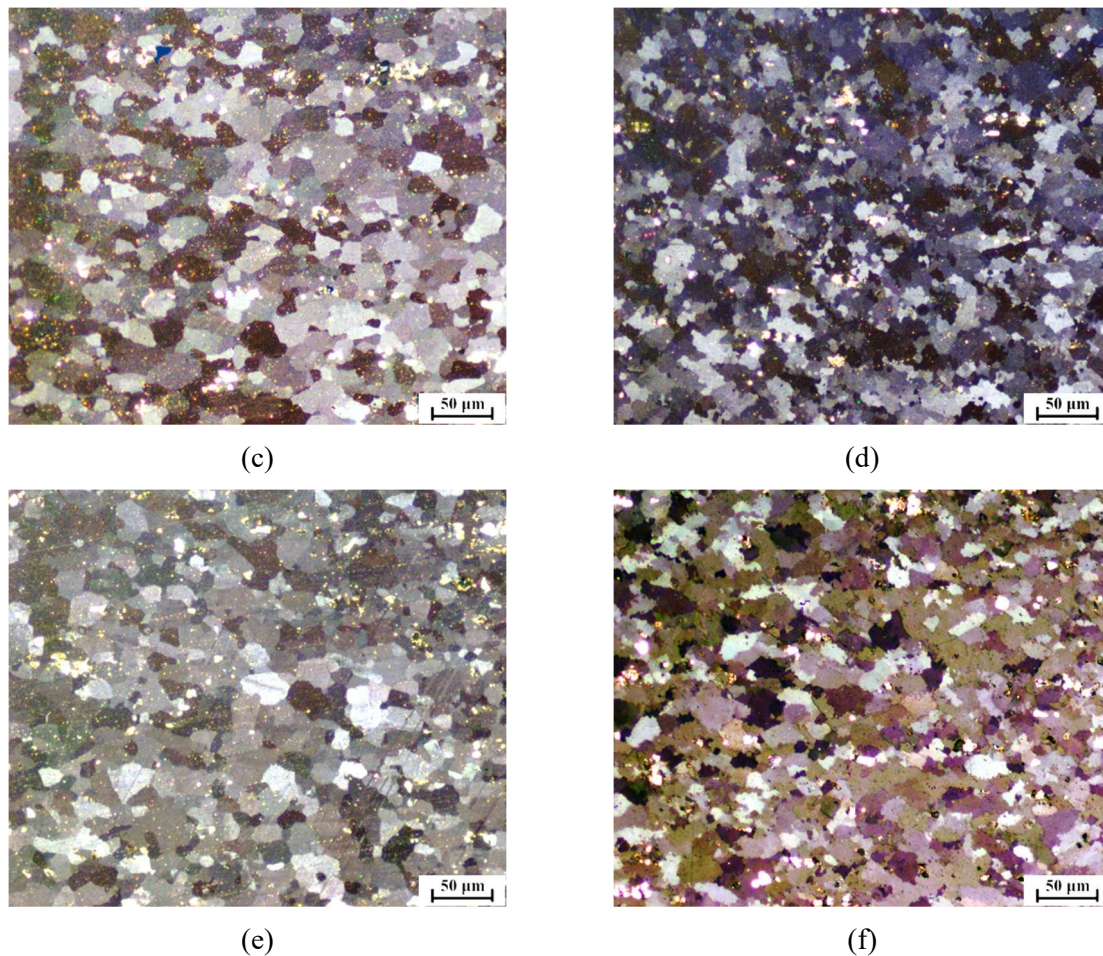
Figure III-12 Metallographic observations of deformed specimens at different temperatures and strain rates. (a) 623 K and 0.0001 s^{-1}; (b) 623 K and 0.1 s^{-1}; (c) 673 K and 0.0001 s^{-1}; (d) 673 K and 0.1 s^{-1}; (e) 723 K and 0.0001 s^{-1}; (f) 723 K and 0.1 s^{-1}

III.3.1.3 *Plastic deformation anisotropy*

For the purpose of evaluating plastic deformation anisotropy, the loading direction has been varied from 0° to 90° for a fixed strain rate of 0.001 s^{-1} and a fixed temperature of 673 K. The corresponding results are shown in Figure III-13. The material exhibits a small degree of plastic deformation anisotropy. The 0° direction displays the highest yield stress compared with the other two directions. The calculated Lankford coefficients are listed in Table III-3. Following the general trend for aluminum alloys, the *r*-values are generally lower than unity [150]. Also, our experimental data for *r*-values are very close to the values obtained for Al-Mg alloy at elevated temperatures [151].
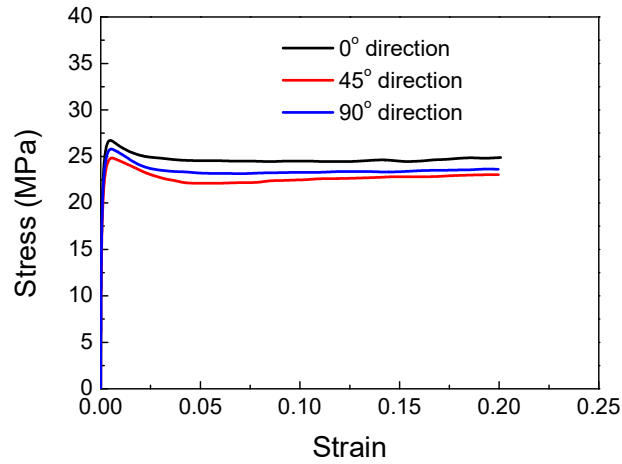
Figure III-13 Stress-strain curves obtained from UT tests at 673 K and 0.001s^{-1} for different directions.

r_0 (-)	r_{45} (-)	r_{90} (-)	Y_0 (MPa)	Y_{45} (MPa)	Y_{90} (MPa)
0.71	0.88	0.78	26.8	24.7	25.7

Table III-3 Yield stresses and Lankford coefficients at 673 K and 0.001 s^{-1}

III.3.2 Biaxial tension

For anisotropic materials, the flow behavior for uniaxial tension and biaxial tension are generally different [152]. As the stress state in the forming process is complex, an accurate determination of the biaxial yield stress is of great importance. For this purpose, some free bulging tests have been carried out with the gas forming machine to estimate the biaxial yield stress at 673 K and 0.001 s^{-1}. However, unlike uniaxial tension experiments, the biaxial yield stress cannot be directly determined from the experimental data. To overcome this difficulty, an inverse method will later be used to estimate the biaxial yield stress.

The bulging forming tests have been carried out at 673 K with three different constant pressures: P_1=0.6 MPa, P_2=1.0 MPa and P_3=1.5 MPa. The experimental dome height evolutions for FB tests are presented in Figure III-14. All the tests are stopped for a dome displacement of 70 mm. It can be clearly seen that the rate of deformation is not linearly related to the pressure value in the whole range. The displacement rate for the dome apex is enormous at the beginning and progressively tends to a steady regime with a constant value. To the same extent of deformation, the highest pressure allows reducing the forming time significantly.
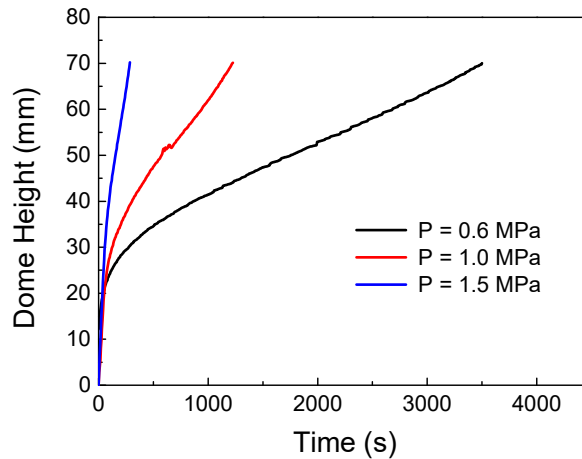
Figure III-14 Dome height-time curves obtained from FB tests

III.4 Damage behavior of the AA5383 alloy

Apart from the constitutive behavior, ductile fracture is another important issue in sheet metal forming. For hot forming of sheet metals, the stress state, as well as the forming temperature and the strain rate, impacts the formability. In this part, the results of the different tests that have been conducted to evaluate the damage behavior of the AA5383 alloy are discussed.

III.4.1 Influence of the stress state

In order to study the effect of the stress state on the ductility, different tests have been performed for a fixed temperature of 673 K and a fixed strain rate of 0.001 s^{-1}. These tests will allow determining the evolution of the equivalent fracture strain as a function of the stress state.

SH tests

The objective of shear tests is to obtain the fracture strain for a purely deviatoric stress state. Thus, it is important to choose the geometry of the specimen such that fracture initiates as a result of shear deformation. Peirs et al. [146] developed a novel shear specimen geometry by using finite element simulations together with experiments. The proposed specimen, with eccentric notch positions, provides a more important concentration of shear strains in the central zone during the deformation when compared to the traditional symmetric notched position shape. For our shear experiments, this eccentric notched specimen is selected and the detailed geometry is shown in Figure III-15.
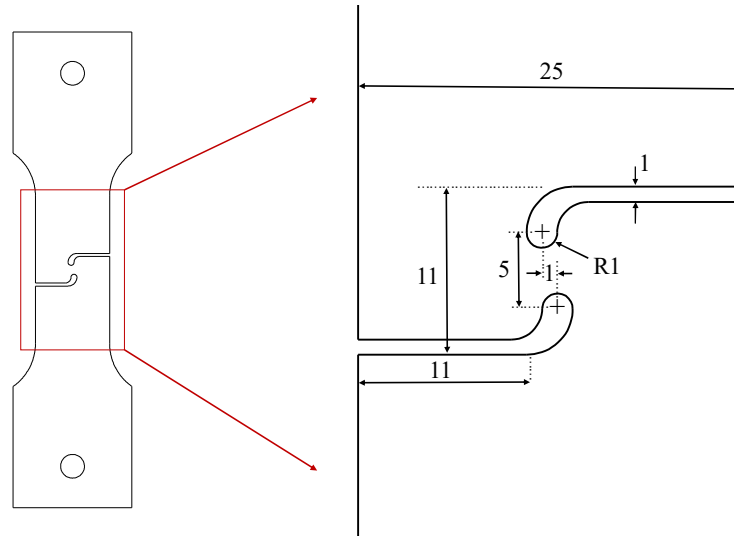
Figure III-15 Detailed geometry of SH specimen

During the shear experiment, the displacement and force are obtained directly from the machine. Unlike uniaxial tensile tests, the stress and strain cannot be calculated analytically from experimental data. Peirs et al. [146] found that, by using this shear geometry, the ratio between the average stress in the shear zone and the local stress in the center part is close to 1 at onset of plastic deformation. Thus, the local stress can be approximately represented by the average stress:

$$\tau_{ave} = \frac{F}{L \cdot t} \tag{III.1}$$

where F is the axial force, L and t are the length and width of the shear region, respectively. However, the relation between the local shear strain and the specimen elongation is not straightforward. To obtain the local shear strain, a numerical-experimental hybrid approach will later be used.

In the shear experiment, the velocity must be adjusted to control the strain rate in the initiation zone. To this aim, different numerical simulations of the shear test have been performed to adjust the velocity to obtain an average equivalent strain rate of $0.001 s^{-1}$ at the center position. As the relation between the shear strain and the displacement is almost linear in the plastic deformation range [146, 153], the velocity is assumed to be constant. For the present tests, the initial gauge length for the extensometer is 25 mm. The velocity has been set to 0.04 mm/s, which corresponds to an equivalent strain rate of $0.001 \ s^{-1}$ in the middle part of the specimen.

Shear tests have been repeated three times. Those force-displacement curves are shown in Figure III-16. According to the experimental results, the repeatability is correct for shear tests. Also, the force progressively increases during the test until fracture initiates. The drop of the axial force is therefore considered as the starting point of fracture.
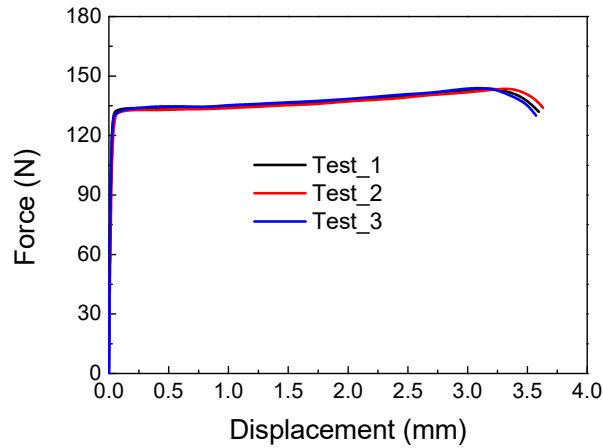
Figure III-16 Force-displacement curves for shear test at 673 K and 0.001 s^{-1}

UT and NT tests

To study the fracture behavior at different stress states, UT, NT20, NT10, NT5 and NT2 specimens have been deformed at 673 K under displacement control for different velocities of 0.024, 0.011, 0.008, 0.006 and 0.005 mm/s, respectively. These loading conditions have been chosen to obtain an average equivalent strain rate of 0.001 s^{-1} at the center position. Three repetitions are carried out in order to ensure the accuracy of the results. The force-displacement curves are shown in Figure III-17. Unlike the shear test, the force in the uniaxial and notched tension tests decreases at the beginning of plastic deformation. We can associate the sudden decrease of force as the point of fracture initiation.

(a)

(b)
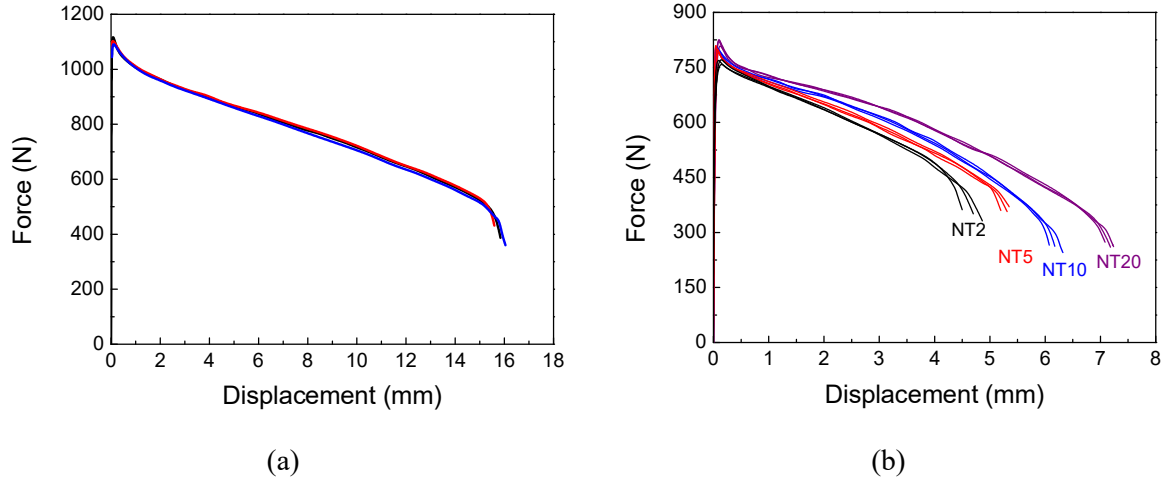
Figure III-17 Force-displacement curves for (a) UT tests and (b) different NT tests at 673 K and 0.001 s^{-1}

With the same initial section area, the axial forces for the different notched specimens at the onset of plastic deformation are quite close to each other. The slight difference can be explained by the different distributions of strain rate in the middle section.

For the fracture displacement of the notched specimen, the NT20 exhibits the maximum displacement (around 7 mm). Generally, the fracture elongation decreases with the decrease of R value for notched specimens [122, 154-156]. As for those tests, the true fracture strain cannot be directly

obtained from the experimental data. A hybrid experimental and simulated method will therefore be used to identify the fracture strains from the computed deformation history (see next chapter).

Some images of notched tension specimens at the instance of failure are shown in Figure III-18. For NT20 and NT10 specimens, the fracture initiates from the center of specimen while the crack starts from the edge of the notch for NT2 specimens. For NT5 specimen, the failure is simultaneously detected in the center and on the edge of the specimen. It is evident that the position of failure initiation changes from the center to the edge of specimen as the original notched radius decreases. A similar phenomenon for notched tension tests has been seen in the literature [154].
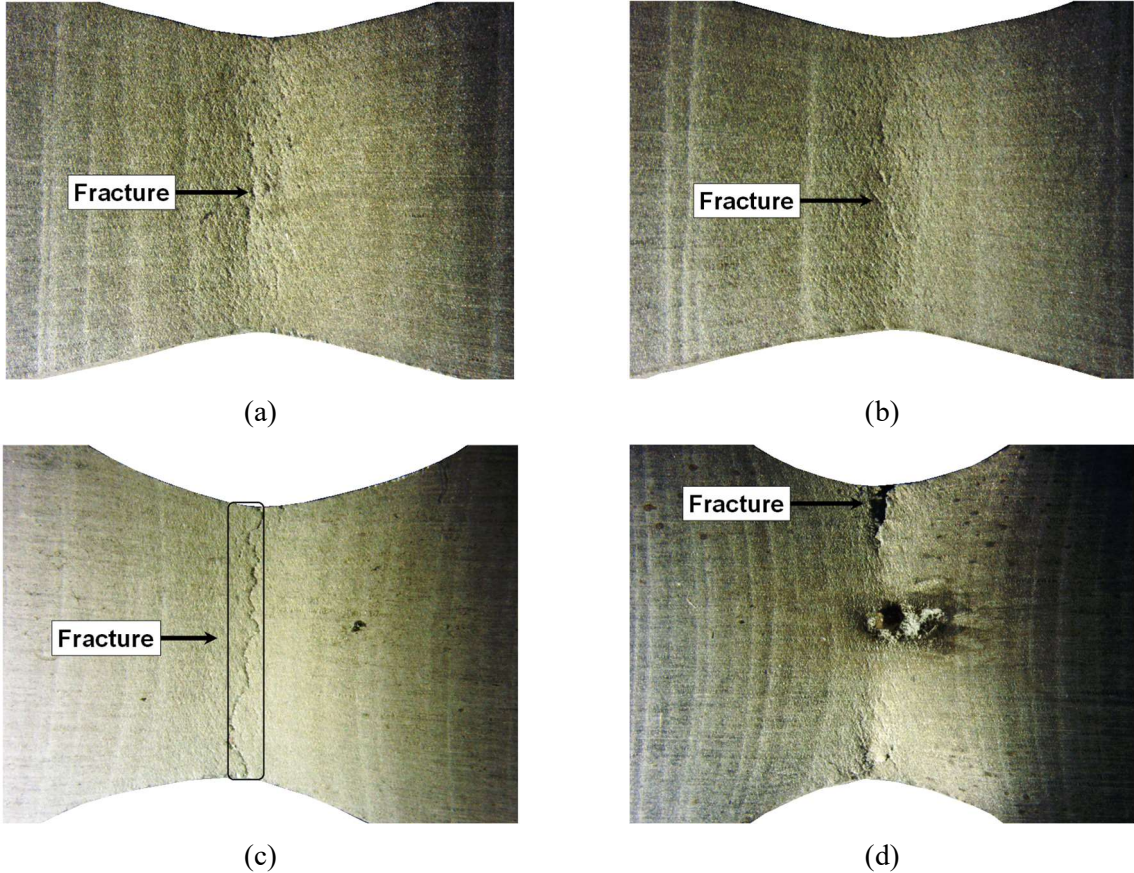
Figure III-18 Experimental fracture initiation deformed at 673 K and 0.001 s^{-1} for (a) NT20; (b) NT10; (c) NT5 and (d) NT2 specimens

Free Bulging test

Free bulging tests can be used to evaluate the fracture strain for a biaxial stress state. To control the strain rate in the experiment, the evolution of the forming pressure needs to be determined numerically at the first step. For the free bulging forming simulation, the subroutine DLOAD is used to change the forming pressure iteratively in order to have the constant deformation strain rate of 0.001 s^{-1} at the dome apex. The employed pressure control strategy and the constitutive model are detailed in Chapter V. The resulting pressure evolution from the numerical simulation, seen in Figure III-19 (a), is used as an input

in the free bulging forming experiment. It can be seen that the forming pressure increases until the maximum value and then slowly decreases. The dome displacement increases gradually with the forming time up to a maximum value of 82.2 mm (Figure III-19 (b)), which is the fracture displacement for free bulging test at 673 K and 0.001 s^{-1}. The deformed specimen is shown in Figure III-20. It can be seen that the fracture is located at the dome apex.

| (a) | (b) |
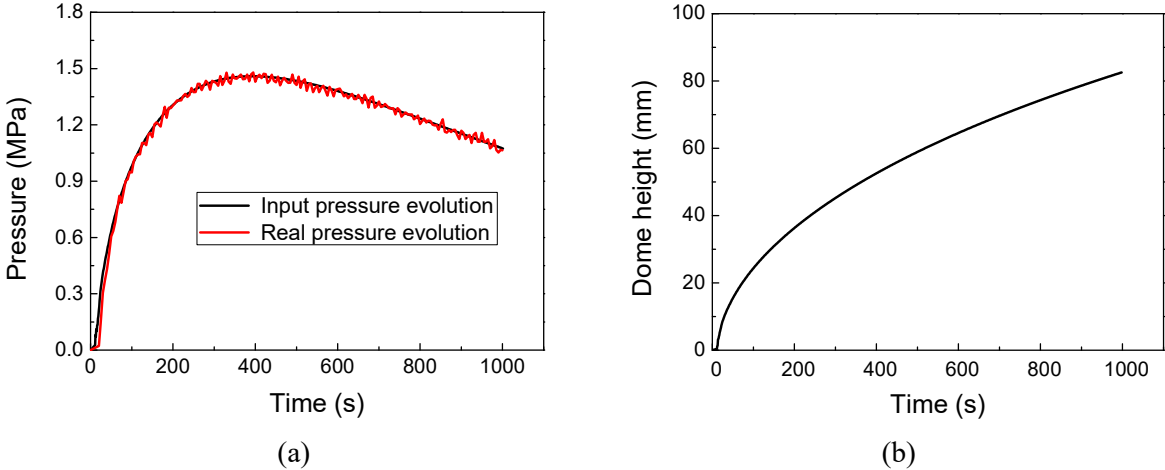
Figure III-19 (a) Pressure evolution; (b) force-displacement curve for FB test deformed at 673 K and 0.001 s^{-1}
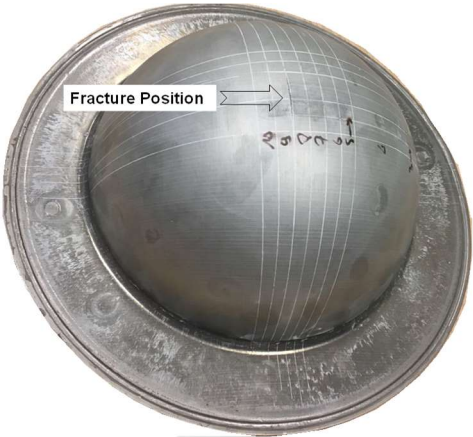
Figure III-20 Fractured specimen for FB test deformed at 673 K and 0.001 s^{-1}

III.4.2 Influence of temperature and strain rate

In the high temperature deformation range, the temperature and strain rate have an important influence on fracture strains [14, 157, 158]. In order to study these effects, the experimental tests are limited to the NT20 specimen. The testing conditions are listed in Table III-4, and each test is repeated three times.

$\dot{\varepsilon}$ (s^{-1}) T (K)	0.0001	0.001	0.01	0.1
623		+		
673	+	+	+	+
723		+		

Table III-4 Testing temperatures and strain rates for NT20 specimen

The force-displacement curves for NT20 specimens at different temperatures and strain rates are shown in Figure III-21. At each testing temperature and strain rate, there exists high repeatability before the sudden decrease of axial force. As expected, the fracture displacement increases with the increment of temperature and the decrement of strain rate.
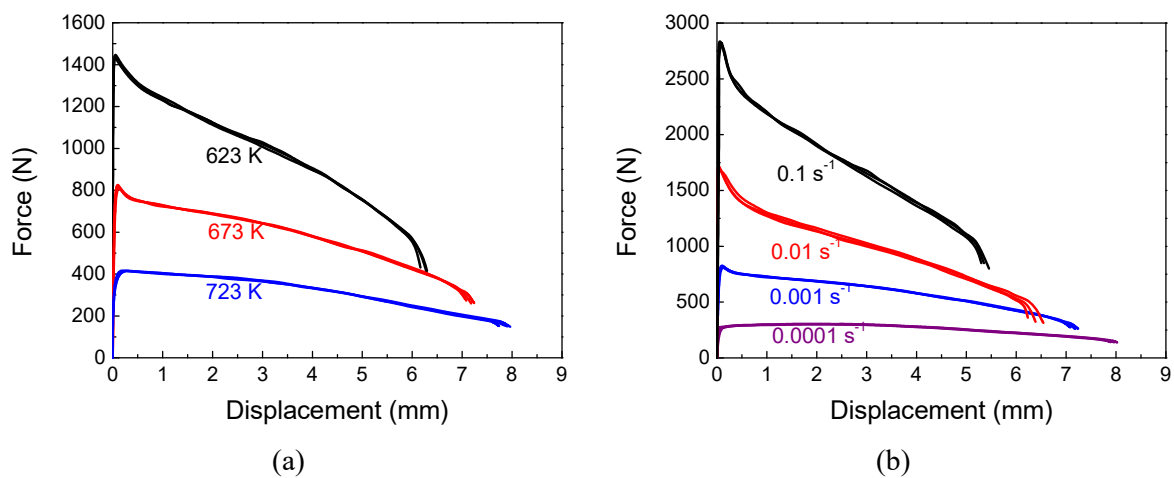
Figure III-21 Force-displacement curves for NT20 specimen deformed at (a) 0.001 s^{-1} and (b) 673 K

III.5 Summary

The present study focuses on the AA5383 aluminum-magnesium alloy. In this chapter, this alloy has been microstructurally and mechanically characterized. For the as-received state, because of the rolling process, the microstructure is composed of elongated grains along the rolling direction. The crystallographic texture is quite pronounced, with an important brass component. In the present work, the AA5383 is heat-treated at 623 K for 5 min prior to any deformation to increase the ductility. As a result of this treatment, grains are equiaxed and the brass component of the crystallographic texture is largely attenuated.

The simulation of hot forming operations requires a constitutive model for the AA5383 alloy. To select an appropriate model, different tests have been carried out. The objective of these tests is twofold.

First, some uniaxial and biaxial tests have been performed to evaluate the flow behavior. These tests provide an experimental database that will be used in the next chapter to identity a yield criterion,

a viscoplastic flow rule and a hardening rule. As expected, the flow stress is largely influenced by strain rate and temperature. The material exhibits a hardening behavior at low strain rates while slight softening occurs for high strain rates. The softening phenomenon is related to dynamic recrystallization. Also, uniaxial tension tests for different angles with respect to rolling direction have been employed to study the anisotropic properties at 673 K and 0.001 s^{-1}. The yield stress along the rolling direction is a little higher than the ones for the 45° and 90° directions.

Second, to characterize the fracture behavior under hot deformation, four notched tension specimens, a shear specimen, together with a free bulging, are used to study the influence of stress state, temperature and strain rate on the forming limit. For a fixed deformation temperature and strain rate, the fracture displacement decreases with the decrease of radius value for notched specimens. Also, for a fixed stress state, the maximum displacement increases with an increasing temperature and a decreasing strain rate. The corresponding results will allow determining the parameters of ductile fracture in the following chapter.

An important difficulty is due to the fact that, except from tension tests on smooth specimens, most material properties (e.g. yield stress, fracture strains) cannot be directly obtained from experimental data. To circumvent this issue, some inverse methods will therefore have to be used to adjust material parameters.

Chapter IV.
Material models for AA5383 alloy at high temperature deformation

In this chapter, material models, including a constitutive model and a damage model, are proposed to describe the thermo-mechanical behavior of AA5383 alloy. The constitutive model consists of flow stress behavior and yield function. For the flow stress behavior, Arrhenius type model and a composite type model are tested. While the BBC2003 yield criterion is proposed to describe the yield behavior under the plane stress condition. Those models are implemented in the user defined subroutine UMAT by a semi-implicit integration method. Finite element simulations are performed of all the experimental tests to obtain equivalent fracture strain at the material point where fracture initiates. The values of stress state for different deformed shapes are also obtained from the numerical results by using a weighting function based on the damage accumulation rule. The modified Mohr-Coulomb (MMC) criterion with adding the influence of temperature and strain rate is proposed to predict the damage behavior. The identification and validation progress are also discussed.

IV.1 Identification strategies

The general strategy for parameter identification is presented in Table IV-1. First, the flow rule parameters have been determined from the results of the uniaxial tension tests performed along the rolling direction. For this purpose, a genetic algorithm (GA) has been used to estimate the corresponding parameters.

Then, to adjust the yield criterion parameters, the yield stresses associated with different loading modes must be known. For uniaxial tension tests, the yield stresses corresponding to the different loading directions are directly obtained from the experimental data. At the opposite, the yield stress for biaxial tension is not directly available from free bulging tests. Therefore, some numerical simulations of bulging tests have been carried out to estimate the biaxial yield stress by comparing the numerical and experimental dome height versus time evolutions for the different imposed pressures. A Newton-Raphson method has been used to obtain the yield criterion parameters.

Finally, using the yield criterion and the flow rule parameters, some numerical simulations of the uniaxial tension, shear, notched tension and free bulging tests have been conducted to determine the MMC fracture criterion parameters. The simulation results have been used to estimate the fracture strains for different loading paths. The criterion parameters have been determined from the fracture strains with a genetic algorithm.

To use the proposed material models or criteria, we have two assumptions: for yield behavior, Lankford coefficients are constant in the studied temperature and strain rate range; for damage behavior, the shape of the fracture locus is not influenced by temperature and strain rate.

	Parameters	Experimental data	Testing condition	Identification method
Flow rule	K, $\bar{\varepsilon}_0^P$, $\hat{n}$, m, b, $\hat{\beta}$	Uniaxial Tension(UT)	T : 623~723 K $\dot{\bar{\varepsilon}}$: 0.0001~0.1 s^{-1} Loading direction: 0°	GA method
Yield criterion	a, M, N, P, Q, $\hat{R}$, S, $\hat{T}$	Uniaxial Tension (UT) Free Bulging (FB)	*For UT:* T : 673 K; $\dot{\bar{\varepsilon}}$: 0.001 s^{-1} Loading direction: 0°, 45°, 90° *For FB:* T : 673 K; $\dot{\bar{\varepsilon}}$: 0.001 s^{-1}	Direct method + Inverse method + Newton-Raphson method
Damage criterion	A, c_1, c_2, c_3, n', D_1, D_2	Tension (UT and NT) Shear (SH) Free Bulging(FB)	*For UT, NT, SH, FB:* T : 673 K; $\dot{\bar{\varepsilon}}$: 0.001 s^{-1} ; *For NT20:* T : 623, 673, 723 K $\dot{\bar{\varepsilon}}$: 0.0001, 0.001, 0.01, 0.1 s^{-1}	Inverse method + GA method

Table IV-1 Parameter identification strategy for AA5383 alloy

IV.2 Constitutive model

In this section, a constitutive model, which consists of flow behavior and yield criterion, is proposed to describe the hot deformation behavior of AA 5383 alloy. For the flow behavior, Arrhenius type model and a composite model are proposed and identified based on the experimental results. While the yield criterion is represented by BCC2003 yield criterion. The implementation algorithm for above models is also presented.

IV.2.1 Flow behavior

The precise description of the flow behavior of metals and alloys under hot deformation conditions is of a great importance for the design of metal forming operations. In our study, two models are tested to describe the flow behavior of AA5383 alloy: Arrhenius model and a composite model. The selection of those two models are based on wide application and easy identification.

IV.2.1.1   Arrhenius model

At hot temperatures, the relation between the flow stress, temperature and strain rate is often expressed by an Arrhenius constitutive model [147]. The influence of temperature and strain rate on the deformation behavior can be represented by Zener-Hollomon parameter [56]. The details of Arrhenius model are referred to Chapter II.

As the original equations of Arrhenius model do not consider the effect of the equivalent plastic strain on the flow stress, the strain-compensated Arrhenius model (the parameters are as the function of the equivalent plastic strain) is often used to describe the flow behavior of alloys. The detailed parameter identification process can be found in Ref. [147]. For our case, the same identification procedure is employed as follows:

- Determination of α by the equation $\beta / \dot{n}$, where β and $\dot{n}$ correspond to the slope of $\bar{\sigma} = f(\ln \dot{\bar{\varepsilon}}^P)$ and $\ln \bar{\sigma} = f(\ln \dot{\bar{\varepsilon}}^P)$, respectively;

- Determination of n by calculation the slope of $\ln[\sinh(\alpha\bar{\sigma})] = f(\ln \dot{\bar{\varepsilon}}^P)$;

- Determination of $\hat{Q}$ by taking the slope of $\ln[\sinh(\alpha\bar{\sigma})] = f(1/T)$;

- Determination of $\hat{A}$ by using the following equation, as all the other parameters are known in this step:

$$\ln[\sinh(\alpha\bar{\sigma})] = \frac{\ln \dot{\bar{\varepsilon}}^P}{n} + \frac{\hat{Q}}{nRT} - \frac{\ln \hat{A}}{n} \tag{IV.1}$$

All the parameters are identified at the equivalent plastic strain from 0.05 to 0.6 with the interval of 0.05. Shown in Figure IV-1, the two order polynomial function is used to plot the identified parameters as the function of the equivalent plastic strain. The corresponding expression is summarized in Table IV-2.

(a) α
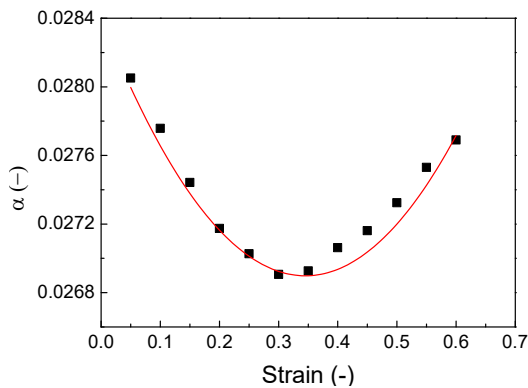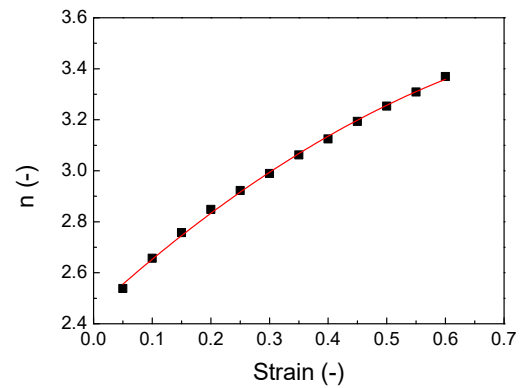
(b) n
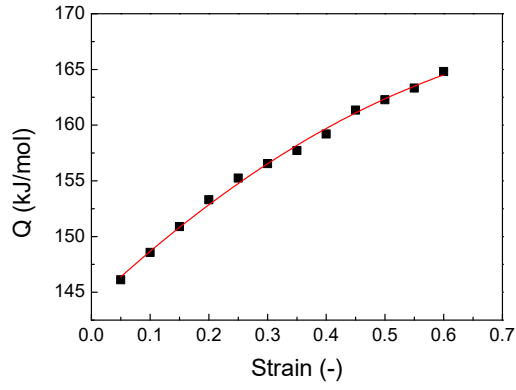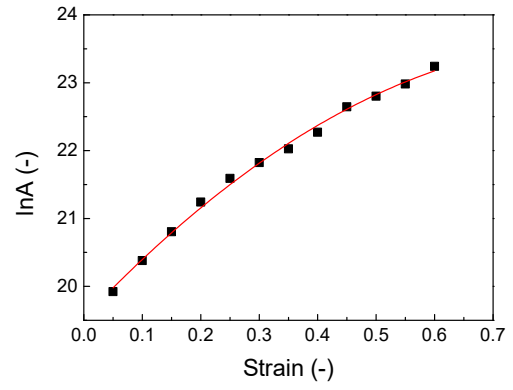
(c) $\hat{Q}$ (d) $\ln \hat{A}$

Figure IV-1 Parameters of Arrhenius model as the function of equivalent plastic strain

Parameter	Expression
α	$0.0126(\bar{\varepsilon}^P)^2 - 0.0087\bar{\varepsilon}^P + 0.0284$
n	$-0.981(\bar{\varepsilon}^P)^2 + 2.098\bar{\varepsilon}^P + 2.453$
$\hat{Q}$	$-25.523(\bar{\varepsilon}^P)^2 + 49.551\bar{\varepsilon}^P + 143.97$
$\ln \hat{A}$	$-5.123(\bar{\varepsilon}^P)^2 + 9.143\bar{\varepsilon}^P + 19.533$

Table IV-2 Material parameters for strain-compensated Arrhenius model

The comparison between the calculated and the experimental stress-strain curves is shown in Figure IV-2. It can be observed that the strain-compensated Arrhenius model can precisely describe the material flow behavior at relatively low strain rates. While for the highest deformation strain rate, the model underestimates the flow stress at 623 K and overestimates the flow stress ate 723 K. For the deformation temperature of 673 K, the experimental results and the calculated results are in good agreement. For the whole studied range, the relative average error of the model is around 7.6 %.
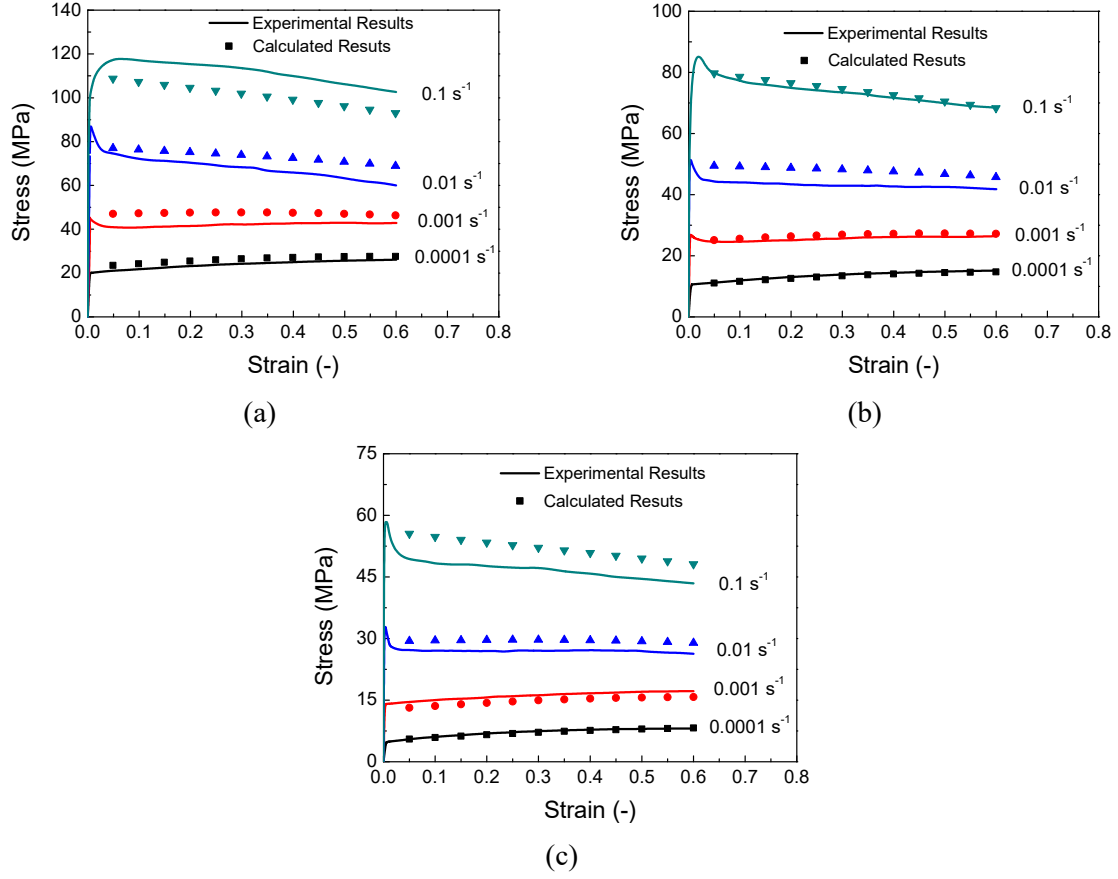
Figure IV-2 Comparison between the experimental results and calculated stress-strain relations by the strain-compensated Arrhenius model at: (a) 623 K; (b) 673 K; (c) 723 K

IV.2.1.2 Composite model

The detailed description of the composite model can be seen in Chapter II. For our alloy, the melting temperature is 858 K, while the reference temperature is set to T_{ref} = 623 K.

A genetic algorithm optimization method [159] is used to identify the parameters. The objective function $\mathfrak{R}_f$ is the relative error between the computed equivalent stress $\bar{\sigma}^C$ and the experimental equivalent stress $\bar{\sigma}^E$

$$\mathfrak{R}_f(K, \bar{\varepsilon}_0^P, \hat{n}, m, b, \hat{\beta}) = \sum \left| \frac{\bar{\sigma}^C - \bar{\sigma}^E}{\bar{\sigma}^E} \right| \tag{IV.2}$$

This function is minimized by the optimization method. Unlike some other common optimization methods (e.g. Newton-Raphson, Levenberg-Marquardt), genetic algorithms have some ability to overcome the difficulties associated with local minima. In this work, the population consists of 10000 individuals, the maximum number of generations is fixed to 100, the crossover probability is 0.8 and the mutation probability is 0.02. The identified parameter values are listed in Table IV-3.

Parameter	K [MPa]	$\bar{\varepsilon}_0^P$ [-]	$\hat{n}$ [-]	m [-]	b [-]	$\hat{\beta}$ [-]
Value	480	0.82	0.65	0.24	0.60	0.28

Table IV-3 Material parameters for the composite model

The comparison between the experimental and simulated results is shown in Figure IV-3. In general, at low strain rates, the calculated results are well in agreement with the experimental results. However, at high stain rates, the predicted results show some differences with the experimental ones. For all tested configurations, the average error of the model is around 6.3%.

Comparing the above two models, the composite model has the advantage to have a lower relative error. Moreover, the implementation of the strain-compensated Arrhenius model is much more difficult due to the dependence of its parameters to equivalent plastic strain. Based on above two reasons, the composite model is adopted to describe the flow behavior of AA5383 alloy.

(a)

(b)

(c)
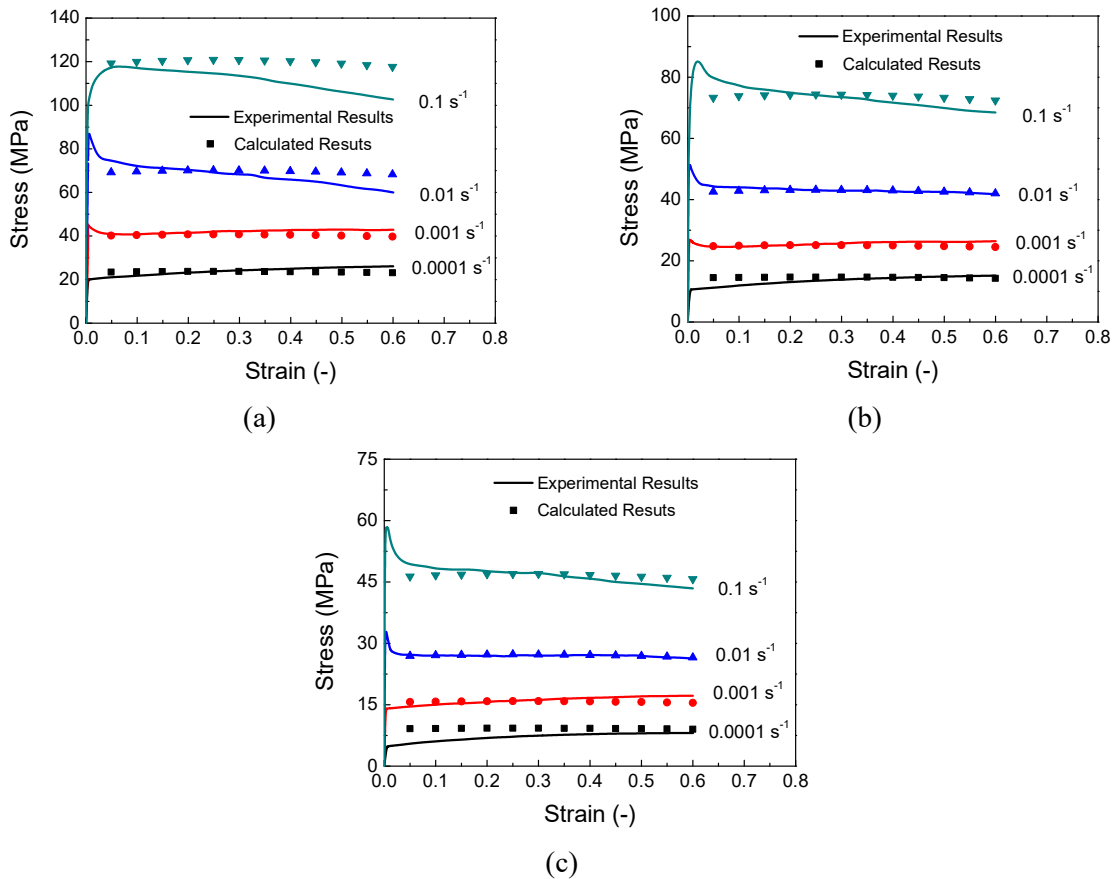
Figure IV-3 Comparison between the experimental results and calculated stress-strain relations by composite model at: (a) 623 K; (b) 673 K; (c) 723 K

IV.2.2 Yield function criteria

In the sheet metal forming, there is a commonly accepted assumption that the sheet is approximately subjected to an in-plane stress loading during the entire processing. Thus, the yield

criteria are considered as a function of the in-plane stresses $\sigma_{11}, \sigma_{22}, \sigma_{12}, \sigma_{21}$ only. Within the whole manuscript, the 1-axis denotes the rolling direction of the sheet, the 2-axis denotes the transverse direction and the 3-axis denotes the normal direction. BBC2003 yield criterion is proposed to describe the yield behavior, as it is an advanced yield criterion for the plane stress condition. What's more, the parameters of this criterion are able to be identified under our experimental conditions. For comparison, the commonly used Hill48 yield criterion is used as a reference.

IV.2.2.1 Determination of the parameters for yield criteria

The parameters of Hill48 yield criterion can be calculated directly by Eq. (II.41), and the corresponding results are shown in Table IV-4.

G	H	F	$\hat{N}$
0.585	0.415	0.532	1.623

Table IV-4 Calculated Hill48 parameters for AA5383 alloy

In this part, we mainly discuss the procedure of identifying the parameters of BBC2003 yield criterion. In the conventional identification of BBC2003 yield criterion, the following experimental data are considered to be given:

- Three directional yield stresses obtained from UT tests along the 0°, 45° and 90° rolling directions (denoted here as Y_0, Y_{45} and Y_{90}).

- Three *r*-values corresponding to 0°, 45° and 90° orientations (denoted here as r_0, r_{45} and r_{90}).

- The biaxial yield stress (denoted here as Y_b).

- The biaxial *r*-value (ratio of plastic strain in transverse direction to the plastic strain in rolling direction), denoted as r_b.

In our study, the experimental coefficient of biaxial plastic anisotropy (r_b) is not available as an input data. The most convenient strategy to handle this problem is to put the following constraint $r_b = 1$. Authors have shown that, for metallic sheets, this constraint can lead to well-shaped yield loci [96]. The value of biaxial yield stress Y_b in this configuration is not explicit. It can be obtained from free bulging tests by using inverse method to fit the dome height evolution. The other data are analytically calculated from the UT tests along different loading directions (i.e. 0°, 45° and 90°).

By using the tensor transformation rules, the plane stress tensor components in the UT specimen with orientation angle θ with respect to the rolling direction are expressed as

$$\sigma_{11} = Y_\theta \cos^2 \theta$$
$$\sigma_{22} = Y_\theta \sin^2 \theta \qquad \text{(IV.3)}$$
$$\sigma_{12} = \sigma_{21} = Y_\theta \cos \theta \sin \theta$$

where Y_θ is the yield stress of the tensile test specimen under uniaxial load. Three stress tensors $\boldsymbol{\sigma}_0, \boldsymbol{\sigma}_{45}$ and $\boldsymbol{\sigma}_{90}$ corresponding to the orientation angle can be obtain from the above equation. For the bulging test, the stress tensor $\boldsymbol{\sigma}_b$ can be determined by $\sigma_{11} = \sigma_{22} = Y_b, \sigma_{12} = \sigma_{21} = 0$.

A directional r-value with different orientation angle θ can be calculated from

$$r_\theta = -\left. \frac{\sin^2 \theta \cdot \dfrac{\partial \Phi}{\partial \sigma_{11}} - \sin 2\theta \cdot \dfrac{\partial \Phi}{\partial \sigma_{12}} + \cos^2 \theta \cdot \dfrac{\partial \Phi}{\partial \sigma_{22}}}{\dfrac{\partial F}{\partial \sigma_{11}} + \dfrac{\partial F}{\partial \sigma_{22}}} \right|_{\sigma_\theta} \qquad \text{(IV.4)}$$

with $\theta \in \{0^o, 45^o, 90^o\}$. While the biaxial r-value, r_b, follows from

$$r_b = \left. \frac{\dfrac{\partial \Phi}{\partial \sigma_{22}}}{\dfrac{\partial \Phi}{\partial \sigma_{11}}} \right|_{\sigma_b} \qquad \text{(IV.5)}$$

Thus, one can obtain the following set of eight equations:

$$\left.\begin{aligned}
\bar{\sigma}(\boldsymbol{\sigma}_0, a, M, N, P, Q, \hat{R}, S, \hat{T}) - Y_{ref} &= 0 \\
\bar{\sigma}(\boldsymbol{\sigma}_{45}, a, M, N, P, Q, \hat{R}, S, \hat{T}) - Y_{ref} &= 0 \\
\bar{\sigma}(\boldsymbol{\sigma}_{90}, a, M, N, P, Q, \hat{R}, S, \hat{T}) - Y_{ref} &= 0 \\
\bar{\sigma}(\boldsymbol{\sigma}_b, a, M, N, P, Q, \hat{R}, S, \hat{T}) - Y_{ref} &= 0 \\
r_0(\boldsymbol{\sigma}_0, a, M, N, P, Q, \hat{R}, S, \hat{T}) - r_0^{\exp} &= 0 \\
r_{45}(\boldsymbol{\sigma}_{45}, a, M, N, P, Q, \hat{R}, S, \hat{T}) - r_{45}^{\exp} &= 0 \\
r_{90}(\boldsymbol{\sigma}_{90}, a, M, N, P, Q, \hat{R}, S, \hat{T}) - r_{90}^{\exp} &= 0 \\
r_b(\boldsymbol{\sigma}_b, a, M, N, P, Q, \hat{R}, S, \hat{T}) - r_b^{\exp} &= 0
\end{aligned}\right\} \qquad \text{(IV.6)}$$

"exp" superscript denotes the values determined from the experiments, while $r(\bullet)$ and $\bar{\sigma}(\bullet)$ are calculated by Eq. (IV.3~IV.5). This equations system is non-linear with respect to eight unknown constants of the yield function. Thus, an improved Newton Raphson method, due to the work of Banabic et al. [96], is employed. The convergence of this algorithm depends on the proper initial vector choice. In the present study, this vector is fixed to [0.7, 1.2, 1, 1, 1, 1, 1, 1] which allows convergence.
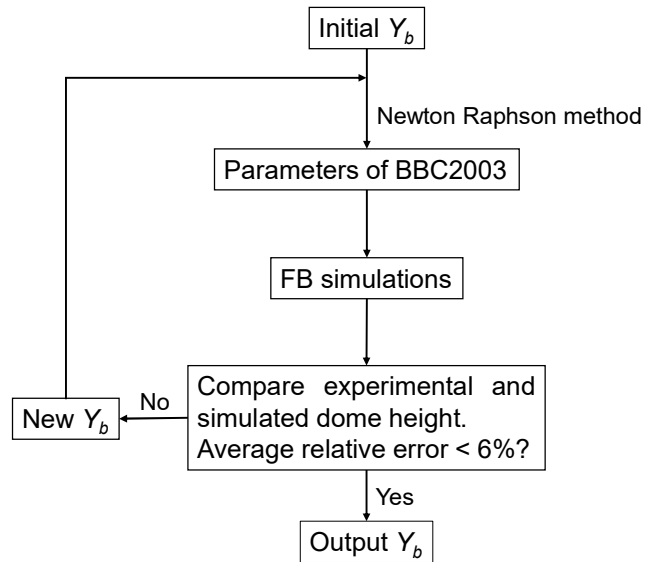
Figure IV-4 Flow chart for the BBC2003 criterion identification

As shown in Figure IV-4, because the biaxial yield stress is unknown at the beginning of the identification procedure, an iterative procedure is used to determine the yield criterion parameters. This procedure uses the experimental data obtained from the free bulging tests with different constant pressures. Specifically, with some estimated yield criterion parameters, numerical simulations of the bulging tests with constant pressures (0.6 MPa, 1.0 MPa and 1.5 MPa) and constant temperature (673 K) are carried out. The numerical and experimental dome height evolutions are compared to each other, which allows adjusting the biaxial yield stress. The new biaxial yield stress is then used as an input of the Newton-Raphson algorithm to obtain a new estimation of the yield criterion parameters. This procedure is repeated until the dome height evolution is correctly reproduced.

(a)   (b)
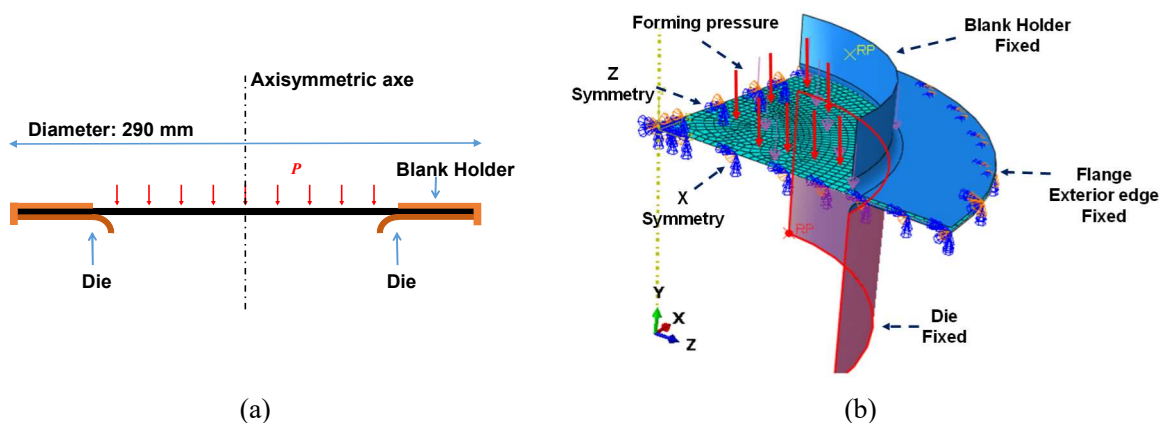
Figure IV-5 (a) Geometry and (b) simulation model for free bulging

The employed numerical model for free bulging test simulations is presented in Figure IV-5.Only a quarter of the part is considered due to symmetry planes. The forming pressure is applied on the upper face of the sheet. The interaction between the sheet (slave) and the die (master) is controlled with a hard

contact algorithm (surface to surface) with Coulomb friction of 0.1 [160]. Shell elements with reduced integration are chosen for the sheet while both the die and blank holder are defined as discrete rigid surfaces.

The final BBC2003 yield criterion parameters are listed in Table IV-5. The corresponding biaxial yield stress at 673 K and 0.001 s^{-1} is $Y_b = 35.3$ MPa. The computed ratio between the biaxial yield stress and the uniaxial yield stress along the rolling direction at 673 K and 0.001 s^{-1} is around 1.32, which is significantly different from the unity value that one would obtain under the assumption of isotropy. Similar phenomenon has also been reported for the Mg AZ31 sheet alloy [161]. As shown in Figure IV-6, this estimation of the biaxial yield stress allows correctly reproducing the evolution of the dome height for the different forming pressures.

(a)

(b)

(c)
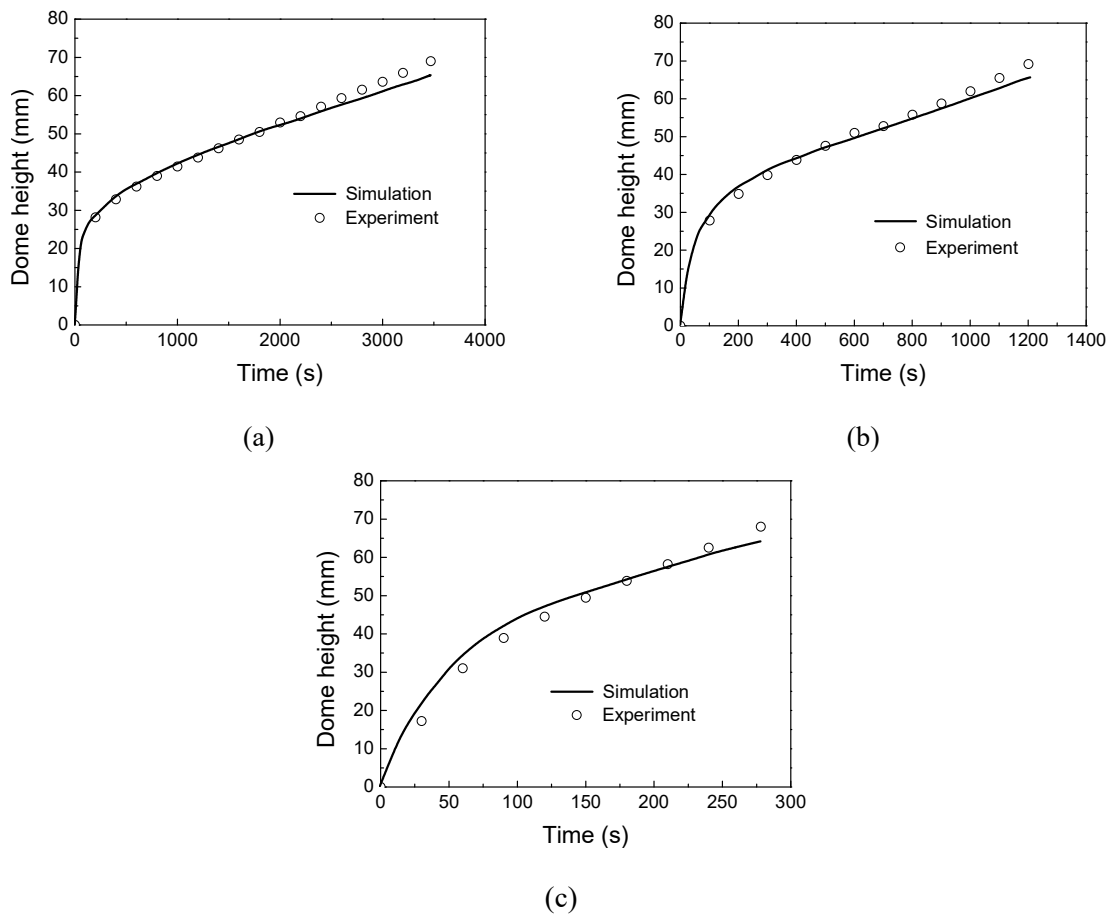
Figure IV-6 Results of inverse analysis for free bulging: experimental date vs. numerical design for forming pressure at (a) 0.6 MPa; (b) 1.0 MPa and (c) 1.5 MPa

a [-]	M [-]	N [-]	P [-]	Q [-]	$\hat{R}$ [-]	S [-]	$\hat{T}$ [-]	Y_{ref} [MPa]	k [-]
0.0339	1.1254	1.9836	1.9740	2.1624	0.8035	0.8528	0.8867	26.8	4

Table IV-5 BBC2003 anisotropic parameters for AA5383 alloy

In the following, the predicted capabilities of Hill48 and BBC2003 yield criteria are compared for AA5383 alloy. As the parameters of Hill48 are analytically calculated from Lankford coefficient *r*-values, the comparison only refers to uniaxial yield stresses and yield locus.

(a)   (b)
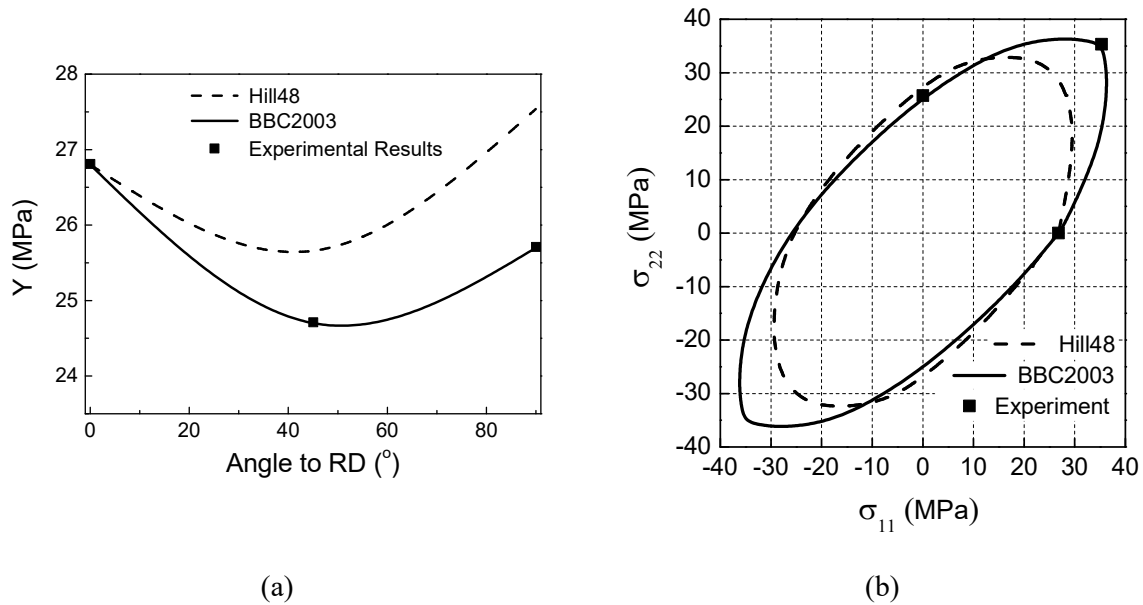
Figure IV-7 (a) Yield stress and (b) yield locus of AA5383 alloy predicted by Hill48 criterion and BBC2003 criterion

As shown in Figure IV-7 (a), the BBC2003 yield criterion can correctly describe the yield stress in all directions, while Hill48 overestimates the yield stress in the 45° and 90° directions. For the yield loci (see Figure IV-7 (b)), the BBC2003 criterion shows a good agreement with the experimental results. However, the Hill48 criterion obviously underestimates the biaxial yield stress, since it does not consider this stress state in the identification of the parameters. Thus, the BBC2003 yield criterion is selected for the whole numerical simulation in our study.

IV.2.3 Implementation of constitutive model

To implement the flow model and the yield criterion into ABAQUS/Implicit solver, a UMAT subroutine needs to be developed. Figure IV-8 presents the general flow chart of the calculations within the UMAT subroutine.
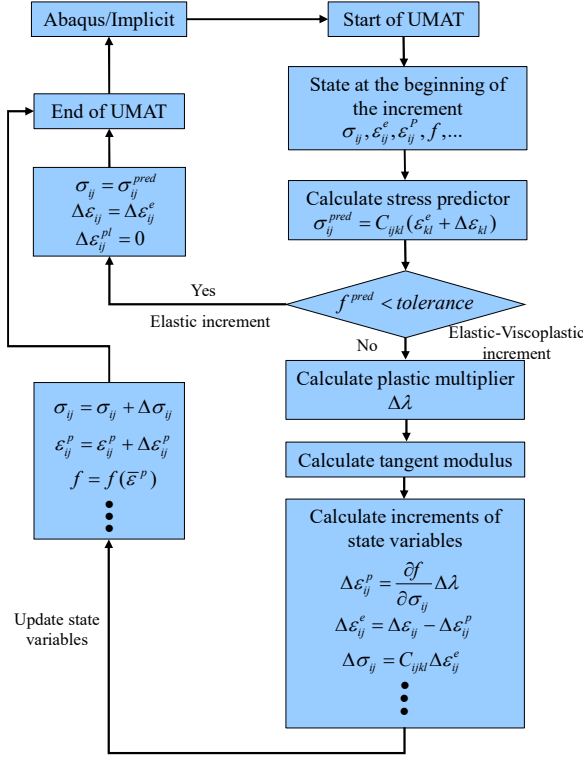
Figure IV-8 Flow chart of calculation in the UMAT subroutine

The plane stress elasticity is assumed to be isotropic, and the plane stress-projected constitutive equations method [162] is used. The explicit expressions relating the elastic and plastic out-of-plane strain components to the in-plane components are needed. Under the plane stress condition, namely $\sigma_{13} = \sigma_{23} = \sigma_{33} = 0$, we have the following relation

$$
\begin{pmatrix} \sigma_{11} \\ \sigma_{22} \\ \sigma_{12} \\ 0 \end{pmatrix} = \begin{pmatrix} 2\mu+\lambda & \lambda & 0 & \lambda \\ \lambda & 2\mu+\lambda & 0 & \lambda \\ 0 & 0 & \mu & 0 \\ \lambda & \lambda & 0 & 2\mu+\lambda \end{pmatrix} \begin{pmatrix} \varepsilon_{11}^e \\ \varepsilon_{22}^e \\ 2\varepsilon_{12}^e \\ \varepsilon_{33}^e \end{pmatrix}
\tag{IV.7}
$$

where λ and μ are referred to *Lamé*'s first parameter and *Lamé*'s second parameter, respectively. Thus, ε_{33}^e can be represented as

$$
\varepsilon_{33}^e = -\frac{\lambda}{2\mu+\lambda}(\varepsilon_{11}^e + \varepsilon_{22}^e)
\tag{IV.8}
$$

Then Eq. (IV.7) can be reduced to

$$
\begin{pmatrix} \sigma_{11} \\ \sigma_{22} \\ \sigma_{12} \end{pmatrix} = \begin{pmatrix} 2\mu+\lambda-\dfrac{\lambda^2}{2\mu+\lambda} & \lambda-\dfrac{\lambda^2}{2\mu+\lambda} & 0 \\ \lambda-\dfrac{\lambda^2}{2\mu+\lambda} & 2\mu+\lambda-\dfrac{\lambda^2}{2\mu+\lambda} & 0 \\ 0 & 0 & \mu \end{pmatrix} \begin{pmatrix} \varepsilon_{11}^e \\ \varepsilon_{22}^e \\ 2\varepsilon_{12}^e \end{pmatrix}
\tag{IV.9}
$$

Thus, for the plane stress condition, the stiffness is represented by

$$\mathbb{C} = \begin{pmatrix} 2\mu + \lambda - \dfrac{\lambda^2}{2\mu + \lambda} & \lambda - \dfrac{\lambda^2}{2\mu + \lambda} & 0 \\[2mm] \lambda - \dfrac{\lambda^2}{2\mu + \lambda} & 2\mu + \lambda - \dfrac{\lambda^2}{2\mu + \lambda} & 0 \\[2mm] 0 & 0 & \mu \end{pmatrix} \tag{IV.10}$$

The associated flow rule is assumed in this study. For the implementation of the constitutive model, the following systems of equations need to be solved

$$\Delta\boldsymbol{\sigma} = \mathbb{C}:\Delta\boldsymbol{\varepsilon}^e = \mathbb{C}:(\Delta\boldsymbol{\varepsilon} - \Delta\boldsymbol{\varepsilon}^P) \tag{IV.11}$$

$$\Delta\boldsymbol{\varepsilon}^P = \Delta\gamma\frac{\partial\Phi}{\partial\boldsymbol{\sigma}} \tag{IV.12}$$

$$\Delta\bar{\varepsilon}^P = \frac{\boldsymbol{\sigma}:\Delta\varepsilon_{ij}^P}{\bar{\sigma}} = \frac{\boldsymbol{\sigma}:\Delta\gamma\dfrac{\partial\Phi}{\partial\boldsymbol{\sigma}}}{\bar{\sigma}} = \frac{\boldsymbol{\sigma}:\dfrac{\partial\Phi}{\partial\boldsymbol{\sigma}}}{\bar{\sigma}}\Delta\gamma = \Delta\gamma \tag{IV.13}$$

Eq. (IV.13) can also be written as

$$\dot{\bar{\varepsilon}}^P = \dot{\gamma} \tag{IV.14}$$

where $\dot{\bar{\varepsilon}}^P$ is equivalent plastic strain rate. Within the framework of rate-dependent plasticity, the equivalent plastic strain rate can be obtained from the composite flow behavior model

$$\dot{\bar{\varepsilon}}^P = \left\{\frac{\bar{\sigma}}{K(\bar{\varepsilon}^P + \bar{\varepsilon}_0^P)^{\hat{n}}\exp(-b\bar{\varepsilon}^P)[1 - (\dfrac{T - T_r}{T_m - T_r})^{\hat{\beta}}]}\right\}^{1/m} \tag{IV.15}$$

In the above system of equations, $\boldsymbol{\sigma}$ is stress tensor, $\bar{\sigma}$ is equivalent stress for BBC yield criterion, $\mathbb{C}$ is the elastic stiffness tensor, $\Delta\gamma$ is plastic multiplier and $\Delta\boldsymbol{\varepsilon}^e$, $\Delta\boldsymbol{\varepsilon}^P$ and $\Delta\bar{\varepsilon}^P$ are elastic, plastic and equivalent plastic strain increments associated with the interval $[t_n, t_{n+1}]$, respectively.

The flow direction $\boldsymbol{n}$ for the plane stress condition can be represented by

$$\boldsymbol{n} = \frac{\partial\Phi}{\partial\boldsymbol{\sigma}} = \frac{\partial\bar{\sigma}}{\partial\boldsymbol{\sigma}} = \frac{\partial\bar{\sigma}}{\partial\sigma_{11}}e_1 \otimes e_1 + \frac{\partial\bar{\sigma}}{\partial\sigma_{22}}e_2 \otimes e_2 + \frac{\partial\bar{\sigma}}{\partial\sigma_{12}}e_1 \otimes e_2 + \frac{\partial\bar{\sigma}}{\partial\sigma_{21}}e_2 \otimes e_1 \tag{IV.16}$$

where e_1, e_2 and e_3 are the principal directions of $\boldsymbol{\sigma}$. The detailed calculation for the derivative of equivalent stress on the stress tensor is given in Appendix A.

Calculate plastic multiplier

In the implicit classic backward-Euler integration scheme, the consistency condition can be ensured but it demands to solve a system of algebraic equations iteratively which increases the computational time. The explicit forward-Euler scheme is fast but suffers in-accuracy in satisfying consistency

condition at the end of each increment. In this study, a semi-implicit method is used in the development of UMAT subroutine. The following equation is employed to calculate the plastic multiplier at each time increment

$$\Delta \boldsymbol{\varepsilon}^p = (1-\alpha)\dot{\boldsymbol{\varepsilon}}_t^p \Delta t + \alpha \dot{\boldsymbol{\varepsilon}}_{t+\Delta t}^p \Delta t \tag{IV.17}$$

where α is a numerical parameter controlling the explicit/implicit character of the integration method. In our integration scheme, α is set to 0.5. Without the consideration of thermal expansion, the plastic strain rate tensor at the end of the time increment can be obtained from a Taylor expansion

$$\dot{\boldsymbol{\varepsilon}}_{t+\Delta t}^p = \dot{\boldsymbol{\varepsilon}}_t^p + \frac{\partial \dot{\boldsymbol{\varepsilon}}^p}{\partial \boldsymbol{\sigma}} : \Delta \boldsymbol{\sigma} + \frac{\partial \dot{\boldsymbol{\varepsilon}}^p}{\partial \overline{\varepsilon}^p} : \Delta \overline{\varepsilon}^p \tag{IV.18}$$

Thus, the following formulation is obtained

$$\Delta \boldsymbol{\varepsilon}^p = \dot{\boldsymbol{\varepsilon}}_t^p \Delta t + \alpha \Delta t \frac{\partial \dot{\boldsymbol{\varepsilon}}^p}{\partial \boldsymbol{\sigma}} : \Delta \boldsymbol{\sigma} + \alpha \Delta t \frac{\partial \dot{\boldsymbol{\varepsilon}}^p}{\partial \overline{\varepsilon}^p} : \Delta \overline{\varepsilon}^p \tag{IV.19}$$

Above expressions $\dfrac{\partial \dot{\boldsymbol{\varepsilon}}^p}{\partial \boldsymbol{\sigma}}$ and $\dfrac{\partial \dot{\boldsymbol{\varepsilon}}^p}{\partial \overline{\varepsilon}^p}$ can be expressed as follows

$$\frac{\partial \dot{\boldsymbol{\varepsilon}}^p}{\partial \boldsymbol{\sigma}} = \frac{\partial \dot{\gamma}}{\partial \boldsymbol{\sigma}} \boldsymbol{n} = \frac{\partial \dot{\gamma}}{\partial \dot{\overline{\varepsilon}}^p} \frac{\partial \dot{\overline{\varepsilon}}^p}{\partial \overline{\sigma}} \frac{\partial \overline{\sigma}}{\partial \boldsymbol{\sigma}} \boldsymbol{n} = \frac{\partial \dot{\overline{\varepsilon}}^p}{\partial \overline{\sigma}} \boldsymbol{n} \otimes \boldsymbol{n} \tag{IV.20}$$

$$\frac{\partial \dot{\boldsymbol{\varepsilon}}^p}{\partial \overline{\varepsilon}^p} = \frac{\partial \dot{\gamma}}{\partial \overline{\varepsilon}^p} \boldsymbol{n} = \frac{\partial \dot{\overline{\varepsilon}}^p}{\partial \overline{\varepsilon}^p} \boldsymbol{n} \tag{IV.21}$$

where $\dfrac{\partial \dot{\overline{\varepsilon}}^p}{\partial \overline{\sigma}}$ and $\dfrac{\partial \dot{\overline{\varepsilon}}^p}{\partial \overline{\varepsilon}^p}$ relate to the rate dependent plasticity (equation IV.26)

$$\frac{\partial \dot{\overline{\varepsilon}}^p}{\partial \overline{\sigma}} = \frac{1}{m} \frac{\dot{\overline{\varepsilon}}^p}{\overline{\sigma}} \tag{IV.22}$$

$$\frac{\partial \dot{\overline{\varepsilon}}^p}{\partial \overline{\varepsilon}^p} = \left\{ \frac{\overline{\sigma}}{K[1-(\frac{T-T_r}{T_m-T_r})^\beta]} \right\}^{1/m} \left[-\frac{n}{m}(\overline{\varepsilon}^p + \overline{\varepsilon}_0^P)^{(-\frac{n}{m}-1)} \exp(\frac{b}{m}\overline{\varepsilon}^p) + (\overline{\varepsilon}^p + \overline{\varepsilon}_0^P)^{(-\frac{n}{m})} \exp(\frac{b}{m}\overline{\varepsilon}^p)\frac{b}{m} \right] \tag{IV.23}$$

The plastic strain increment can therefore be obtained from the resolution of

$$\Delta \boldsymbol{\varepsilon}^p + \alpha \Delta t (\frac{\partial \dot{\boldsymbol{\varepsilon}}^p}{\partial \boldsymbol{\sigma}} : \mathbb{C} : \Delta \boldsymbol{\varepsilon}^p - \frac{\partial \dot{\boldsymbol{\varepsilon}}^p}{\partial \overline{\varepsilon}^p} : \Delta \overline{\varepsilon}^p) = \dot{\boldsymbol{\varepsilon}}^p \Delta t + \alpha \Delta t \frac{\partial \dot{\boldsymbol{\varepsilon}}^p}{\partial \boldsymbol{\sigma}} : \mathbb{C} : \Delta \boldsymbol{\varepsilon} \tag{IV.24}$$

An alternative form consists of estimating $\Delta \overline{\varepsilon}^p$ by solving the following equation

$$\Delta \overline{\varepsilon}^p \boldsymbol{n} + \alpha \Delta t (\frac{\partial \dot{\overline{\varepsilon}}^p}{\partial \overline{\sigma}} \boldsymbol{n} \otimes \boldsymbol{n} : \mathbb{C} : \boldsymbol{n} \Delta \overline{\varepsilon}^p - \boldsymbol{n} \frac{\partial \dot{\overline{\varepsilon}}^p}{\partial \overline{\varepsilon}^p} \Delta \overline{\varepsilon}^p) = \dot{\overline{\varepsilon}}^p \boldsymbol{n} \Delta t + \alpha \Delta t \frac{\partial \dot{\overline{\varepsilon}}^p}{\partial \overline{\sigma}} \boldsymbol{n} \otimes \boldsymbol{n} : \mathbb{C} : \Delta \boldsymbol{\varepsilon} \tag{IV.25}$$

Dividing above by $\boldsymbol{n}$, we can obtain

$$\Delta \overline{\varepsilon}^p + \alpha \Delta t (\frac{\partial \dot{\overline{\varepsilon}}^p}{\partial \overline{\sigma}} \boldsymbol{n} : \mathbb{C} : \boldsymbol{n} \Delta \overline{\varepsilon}^p - \frac{\partial \dot{\overline{\varepsilon}}^p}{\partial \overline{\varepsilon}^p} \Delta \overline{\varepsilon}^p) = \dot{\overline{\varepsilon}}^p \Delta t + \alpha \Delta t \frac{\partial \dot{\overline{\varepsilon}}^p}{\partial \overline{\sigma}} \boldsymbol{n} : \mathbb{C} : \Delta \boldsymbol{\varepsilon} \tag{IV.26}$$

Thus,

$$\Delta\gamma = \Delta\overline{\varepsilon}^p = \frac{\dot{\overline{\varepsilon}}^p \Delta t + \alpha\Delta t \dfrac{\partial\dot{\overline{\varepsilon}}^p}{\partial\overline{\sigma}} \boldsymbol{n}:\mathbb{C}:\Delta\boldsymbol{\varepsilon}}{1 + \alpha\Delta t(\dfrac{\partial\dot{\overline{\varepsilon}}^p}{\partial\overline{\sigma}}\boldsymbol{n}:\mathbb{C}:\boldsymbol{n} - \dfrac{\partial\dot{\overline{\varepsilon}}^p}{\partial\overline{\varepsilon}^p})} \tag{IV.27}$$

By using the plastic incompressibility, the plastic thickness strain is obtained

$$\varepsilon_{33}^p = -(\varepsilon_{11}^p + \varepsilon_{22}^p) \tag{IV.28}$$

The elasto-viscoplastic consistent tangent operator

Based on Eq. (IV. 11), it can be derived

$$\Delta\boldsymbol{\sigma} = \mathbb{C}:(\Delta\boldsymbol{\varepsilon} - \Delta\boldsymbol{\varepsilon}^p) = \mathbb{C}:(\Delta\boldsymbol{\varepsilon} - \Delta\gamma\boldsymbol{n}) \tag{IV.29}$$

Combining Eq. (IV.27) with Eq. (IV. 29), it follows

$$\begin{aligned}
\Delta\boldsymbol{\sigma} &= \mathbb{C}:(\Delta\boldsymbol{\varepsilon} - \boldsymbol{n}\frac{\dot{\overline{\varepsilon}}^p \Delta t + \alpha\Delta t \dfrac{\partial\dot{\overline{\varepsilon}}^p}{\partial\overline{\sigma}} \boldsymbol{n}:\mathbb{C}:\Delta\boldsymbol{\varepsilon}}{1 + \alpha\Delta t(\dfrac{\partial\dot{\overline{\varepsilon}}^p}{\partial\overline{\sigma}}\boldsymbol{n}:\mathbb{C}:\boldsymbol{n} - \dfrac{\partial\dot{\overline{\varepsilon}}^p}{\partial\overline{\varepsilon}^p})}) \\
&= \mathbb{C}:(\mathbf{I} - \frac{\boldsymbol{n}\alpha\Delta t \dfrac{\partial\dot{\overline{\varepsilon}}^p}{\partial\overline{\sigma}}\boldsymbol{n}:\mathbb{C}}{1 + \alpha\Delta t(\dfrac{\partial\dot{\overline{\varepsilon}}^p}{\partial\overline{\sigma}}\boldsymbol{n}:\mathbb{C}:\boldsymbol{n} - \dfrac{\partial\dot{\overline{\varepsilon}}^p}{\partial\overline{\varepsilon}^p})}):\Delta\boldsymbol{\varepsilon} - \mathbb{C}:\frac{\boldsymbol{n}\dot{\overline{\varepsilon}}^p \Delta t}{1 + \alpha\Delta t(\dfrac{\partial\dot{\overline{\varepsilon}}^p}{\partial\overline{\sigma}}\boldsymbol{n}:\mathbb{C}:\boldsymbol{n} - \dfrac{\partial\dot{\overline{\varepsilon}}^p}{\partial\overline{\varepsilon}^p})}
\end{aligned} \tag{IV.30}$$

The visco-plastic consistent tangent matrix is defined by

$$\mathbb{C}^{ep} = \frac{d\boldsymbol{\sigma}_{n+1}}{d\boldsymbol{\varepsilon}_{n+1}} \tag{IV.31}$$

where $\boldsymbol{\sigma}_{n+1}$ and $\boldsymbol{\varepsilon}_{n+1}$ are the updated stress and total strain tensor, respectively. Thus, we can find

$$\mathbb{C}^{ep} = \mathbb{C}:(\mathbf{I} - \frac{\boldsymbol{n}\alpha\Delta t \dfrac{\partial\dot{\overline{\varepsilon}}^p}{\partial\overline{\sigma}}\boldsymbol{n}:\mathbb{C}}{1 + \alpha\Delta t(\dfrac{\partial\dot{\overline{\varepsilon}}^p}{\partial\overline{\sigma}}\boldsymbol{n}:\mathbb{C}:\boldsymbol{n} - \dfrac{\partial\dot{\overline{\varepsilon}}^p}{\partial\overline{\varepsilon}^p})}) = \mathbb{C} - \frac{\alpha\Delta t \dfrac{\partial\dot{\overline{\varepsilon}}^p}{\partial\overline{\sigma}}(\mathbb{C}:\boldsymbol{n})(\boldsymbol{n}:\mathbb{C})}{1 + \alpha\Delta t(\dfrac{\partial\dot{\overline{\varepsilon}}^p}{\partial\overline{\sigma}}\boldsymbol{n}:\mathbb{C}:\boldsymbol{n} - \dfrac{\partial\dot{\overline{\varepsilon}}^p}{\partial\overline{\varepsilon}^p})}) \tag{IV.32}$$

In order to verify the implementation of the developed UMAT, one possible solution is to compare its results for a specific case with those obtained from well-established model available in the ABAQUS library. A specific set of the BBC2003 parameters permits to recover the von Mises criterion if $2a = M = N = P = Q = R = S = T = 1$. By using those values, the accuracy of the developed UMAT subroutine can be assessed by comparing to the ABAQUS built-in Mises plasticity model. Thus, the simple uniaxial tension, shear and biaxial tension simulations are designed and conducted with assuming of isotropic mechanical behavior. The comparison demonstrates the accuracy of the developed UMAT subroutine.

IV.3 Damage model

One of the objectives for the thesis is to study the influence of stress state, temperature and strain rate on the damage behavior of AA5383 alloy. In this part, the equivalent fracture strains at different forming conditions are determined by performing the finite element simulations of all the experimental tests. The MMC criterion with the consideration of temperature and strain rate is proposed to predict the damage behavior.

IV.3.1 Determination of equivalent fracture strain

Due to the localization of deformation before the occurrence of fracture, the data from the extensometer is not yet valid. The value of the localized equivalent plastic deformation could be determined using numerical simulations. In this section, SH, UT, NT20, NT10, NT5, NT2 and FB simulations are performed at 673 K and 0.001 s^{-1} to investigate the impact of stress state on equivalent fracture strains. While NT20 is chosen to study the effect of temperature and strain rate. In the numerical simulations, the BBC2003 yield criterion with the composite hardening model is employed. The increment time for each step is fixed at 0.1 s. To reduce the computational cost, 2-D shell elements are selected. The displacement or force boundary conditions for the numerical simulations are identical to the corresponding experiments.

IV.3.1.1 Mesh convergence analysis

First of all, before running the needed numerical simulations, mesh convergence is investigated. Table IV-6 illustrates/summarizes the tested configurations.

	Mesh size (mm)	Elements number
Mesh_1	0.3	6754
Mesh_2	0.1	12004
Mesh_3	0.05	20236

Table IV-6 Mesh size and element number for the FE model of NT20 specimen at 673 K and 0.001 s^{-1}

The impact of mesh size on equivalent plastic strain, stress triaxiality and force-displacement curves is shown in Figure IV-9. It can be concluded that mesh convergence is ensured when using a mesh size less than 0.1 mm. Indeed, the difference between the tested configurations could be remarked for large deformations especially when the equivalent deformation exceeds 0.6.
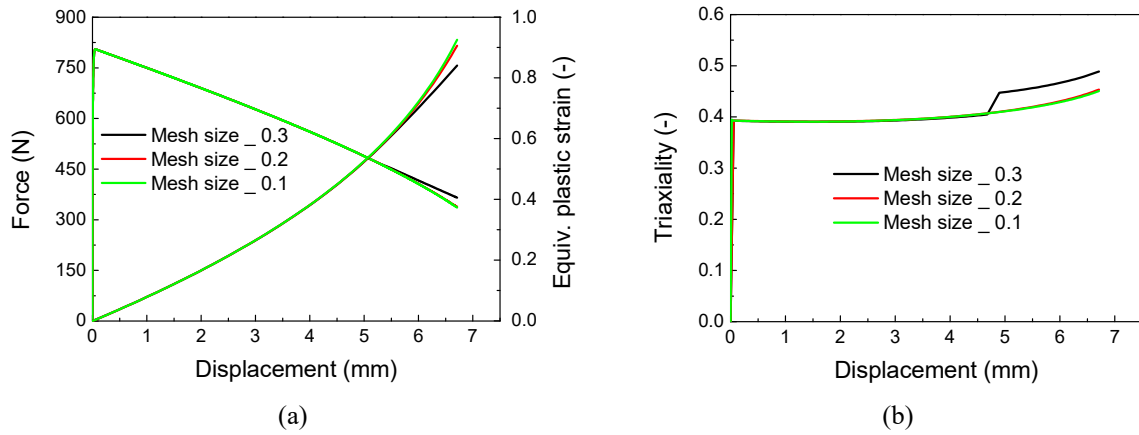
Figure IV-9 Numerical results of NT20 at different mesh sizes: (a) force and equivalent plastic strain vs displacement curves and (b) stress triaxiality vs displacement curve

IV.3.1.2   Comparison between 3D and 2D simulation

Throughout this manuscript, 2D shell elements have been used for the numerical simulations. To check the 3D influence, we have performed shear and notched tension simulations in both 2D and 3D by using von Mises yield criterion. The stress triaxiality evolutions are shown in Figure IV-10. First, the difference between 3D and 2D simulation is negligible, especially for SH and NT5 tests. Thus, the triaxiality value can reasonably be estimated with 2D models under the plane stress assumption. Second, when the actual thickness of shear specimens is considered, the shear condition is reasonably satisfied, with a triaxiality ranging from -0.1 to 0.06.
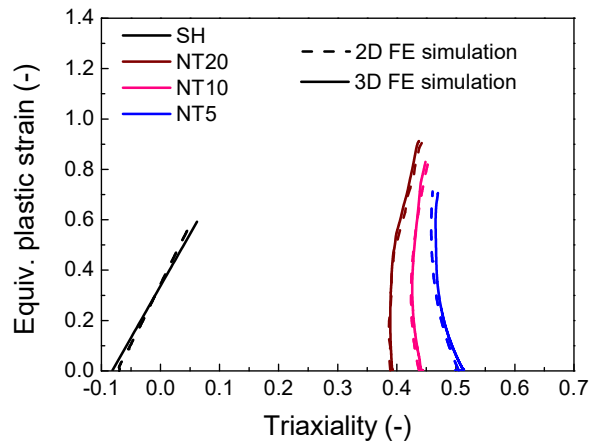
Figure IV-10 Comparison of stress triaxiality evolution between 3D and 2D FE simulations

IV.3.1.3   Influence of specimen geometry, temperature and strain rate on the equivalent fracture strain

SH simulation at 673 K and 0.001 s^{-1}

Figure IV-11 (a) presents the numerical model for SH specimen. The mesh size in the middle part is set to 0.1 mm due to the mesh convergence study. Figure IV-11 (b) shows that the maximum equivalent plastic strain at the fracture displacement is quietly consistent in the middle part. SDV7 parameter indicates the equivalent plastic strain. Hence, the average equivalent fracture strain is calculated in this area.

(a)   (b)
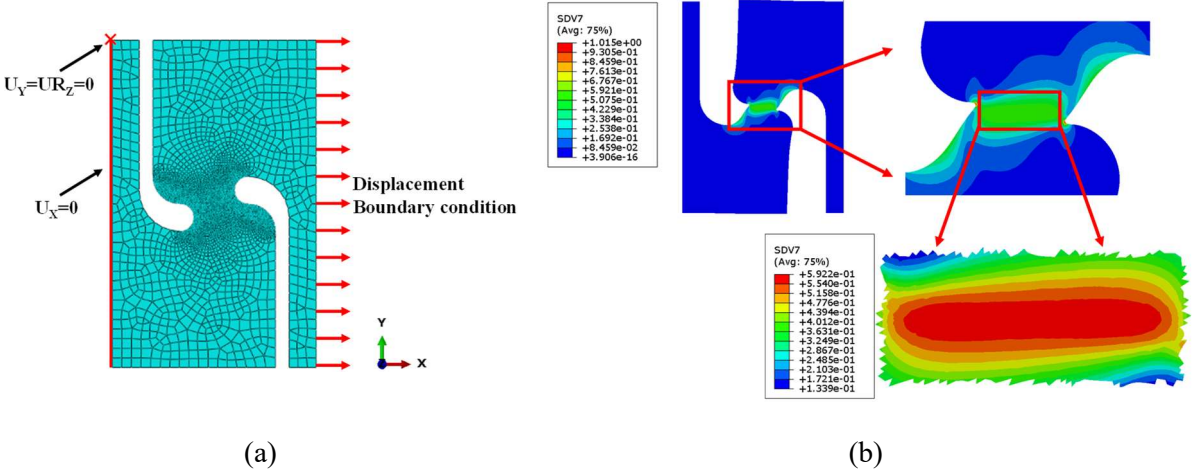
Figure IV-11 (a) Numerical model and (b) equivalent plastic strain distribution at the instant of failure for SH specimen

The simulated equivalent plastic strain evolution and force-displacement curves are illustrated by Figure IV-12. The average error between the simulated and the experimental curves does not exceed 0.1%.
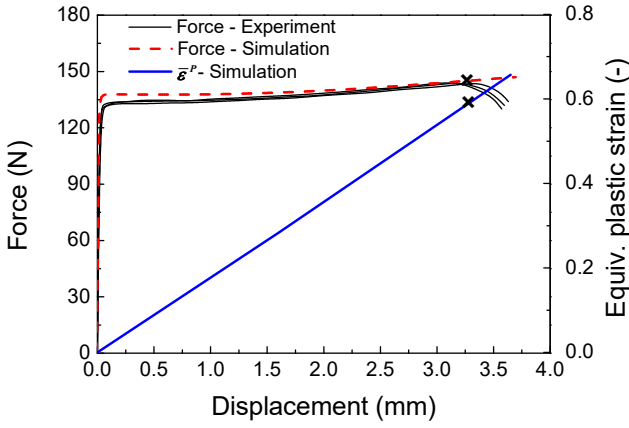
Figure IV-12 Experimental and numerical force-displacement comparison and the evolution of the equivalent plastic strain deformed at 673 K and 0.001 s^{-1} for SH specimen

UT and NT simulations at 673 K and 0.001 s^{-1}

The numerical models for a uniaxial tension and four notched tension specimens are shown in Figure IV-13. Due to the mesh convergence study, the element size is set to 0.1, 0.2, 0.15, 0.1 and 0.07 mm for UT, NT20, NT10, NT5 and NT2, respectively. Figure IV-14 shows the distribution of the

equivalent plastic strain at the fracture displacement. For UT, NT20 and NT10 specimens, the maximum equivalent plastic strain is localized in the center of the specimen. These results are in agreement with the literature [154, 163]. However, based on experimental observations, the equivalent plastic fracture strain is calculated at the center of the NT5 specimen and at the notch edge of the NT2 specimen. Only UT, NT20, NT10 and NT5 specimens are used to calibrate the fracture criterion. The NT2 specimen will be used for the verification of the identified damage model parameters.
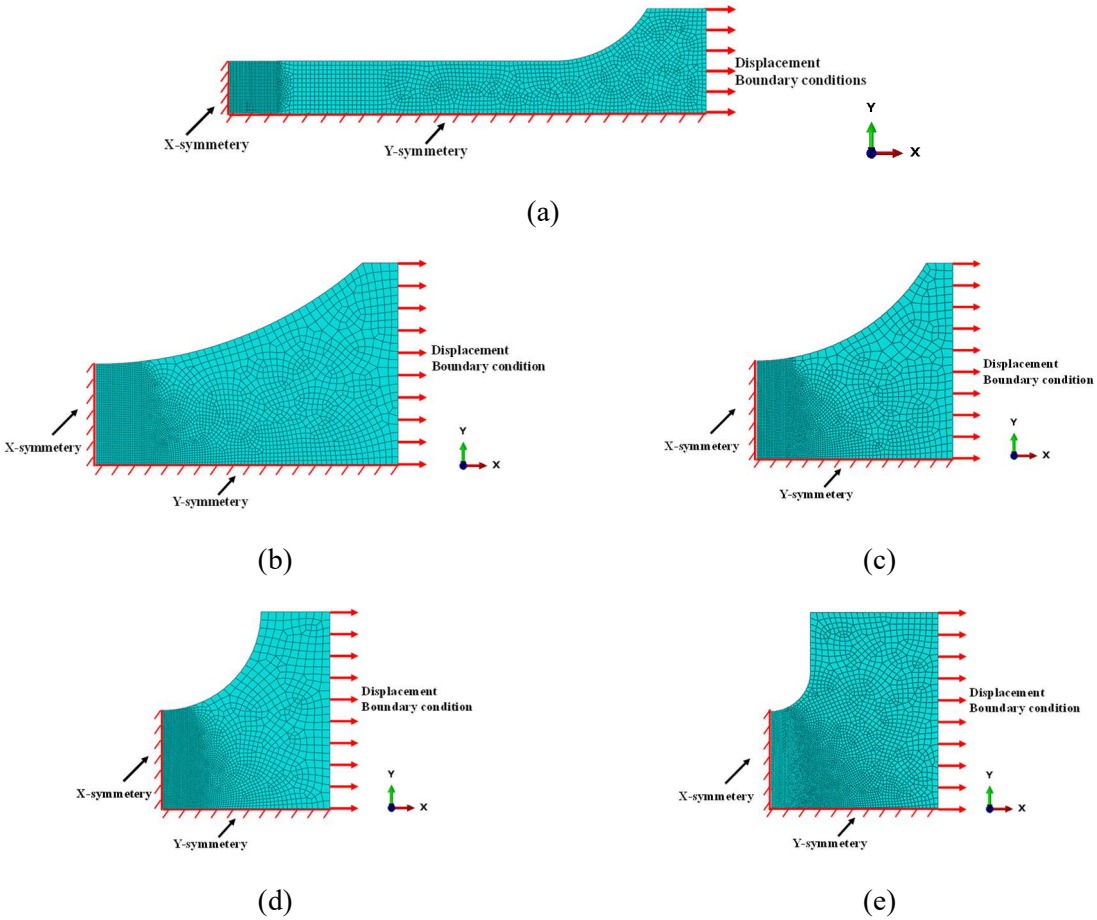
Figure IV-13 Numerical models for different tension specimens: (a) UT; (b) NT20; (c) NT10; (d) NT5 and (e) NT2
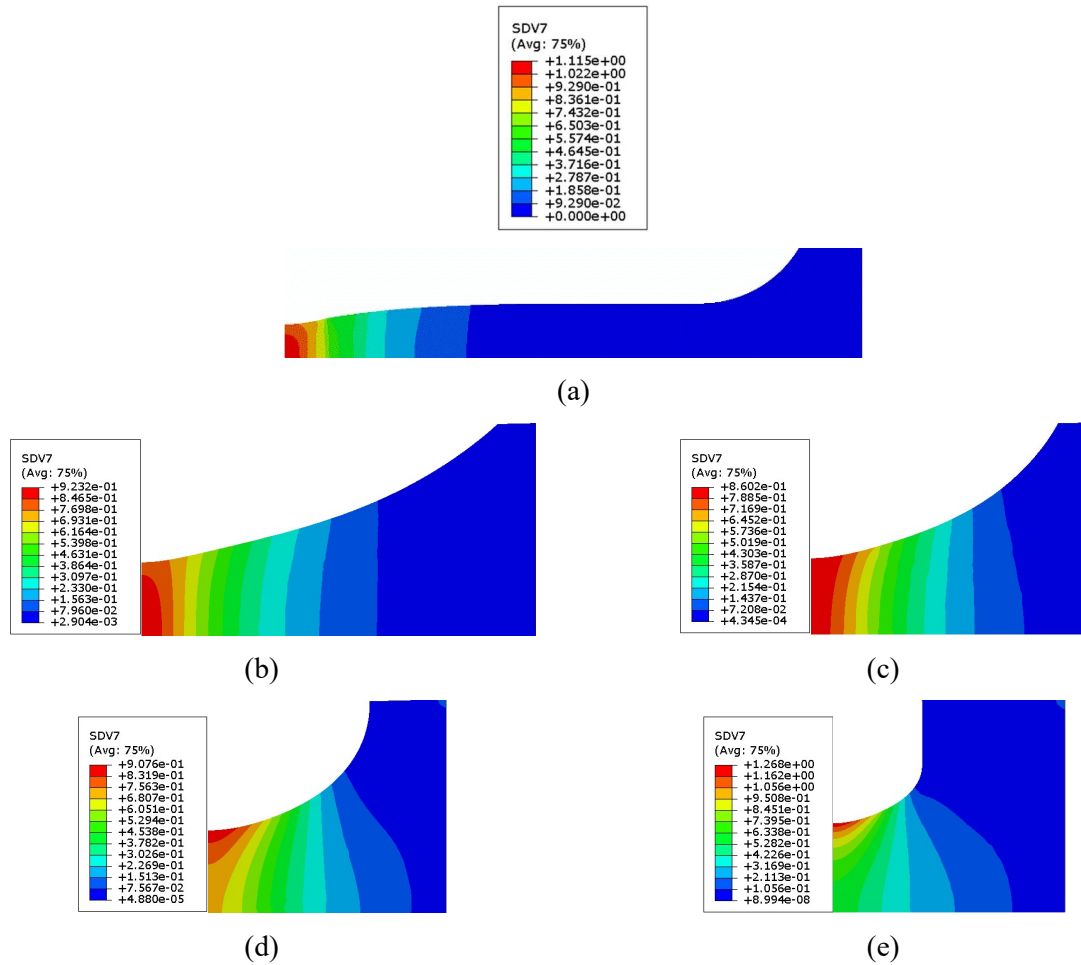
Figure IV-14 Equivalent plastic strain distribution at the instant of failure for different notched specimens: (a) UT; (b) NT20; (c) NT10; (d) NT5 and (e) NT2

The experimental and simulated force-displacement curves at 673 K and 0.001 s^{-1} and corresponding numerical equivalent plastic strain evolution for UT and three NT specimens are shown in Figure IV-15. The agreement of the predicted force-displacement curves with the experimental results gives the evidence that the employed constitutive model can describe the material behavior under different stress states. For convenience, the average experimental value of fracture displacement is calculated and taken into account for the equivalent plastic fracture strain determination.
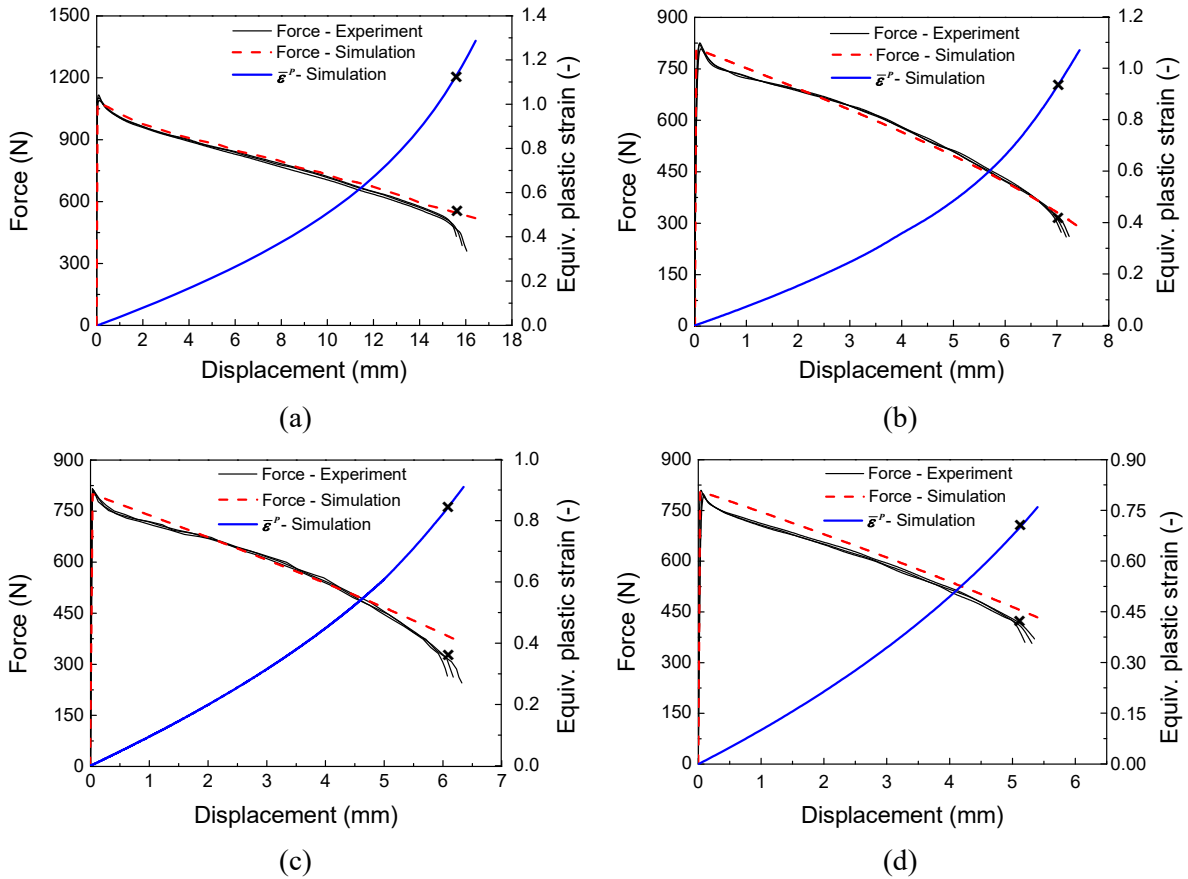
Figure IV-15 Force-displacement curves and the equivalent plastic strain evolution for tension specimens at 673 K and 0.001 s^{-1}: (a) UT; (b) NT20; (c) NT10 and (d) NT5

FB simulation at 673 K and 0.001 s^{-1}

The numerical model for FB is depicted in Figure IV-5. The boundary conditions are identical to the FB simulations at constant forming pressures. The mesh size is set to 1.0 mm due to the mesh convergence study. The experimental and predicted pressure-displacement curves are in good agreement (Figure IV-16). The evolution of equivalent plastic strain is output at the dome apex due to fracture initiation position.
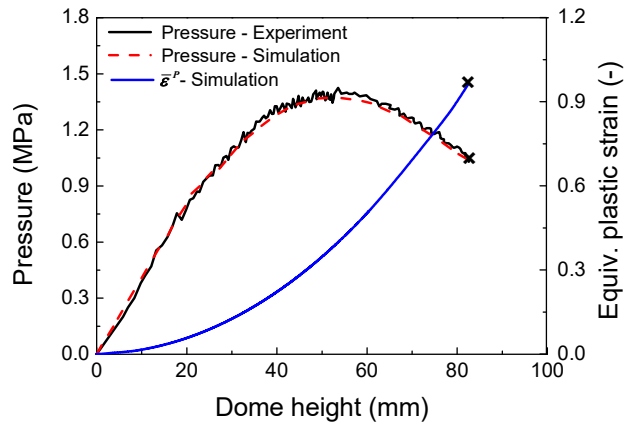
Figure IV-16 Pressure-displacement curves and evolution of equivalent plastic strain for free bulging at 673 K and 0.001 s^{-1}

NT20 simulations at different temperatures and strain rates

NT20 tests have been carried out to study the influence of temperature and strain rate on the fracture behavior. In this part, the corresponding simulations are performed to obtain the equivalent plastic strains in the studied temperature and strain rate range. The comparisons of the force-displacement curves between the experiments and simulations are presented in Figure IV-17. For all the cases, the numerical force predictions are in good agreement with the experimental ones when the displacement is larger than 1.0 mm. However, there exists an obvious difference at the initial deformation, especially for the high strain rates. The force-displacement curves are directly related to the hardening behavior of the material. Hence, the difference in the force values can be due to the fact that the composite model is identified without taking the initial peak yield stress into consideration.

(a) 673 K ; 0.0001 s^{-1}

(b) 673 K ; 0.001 s^{-1}
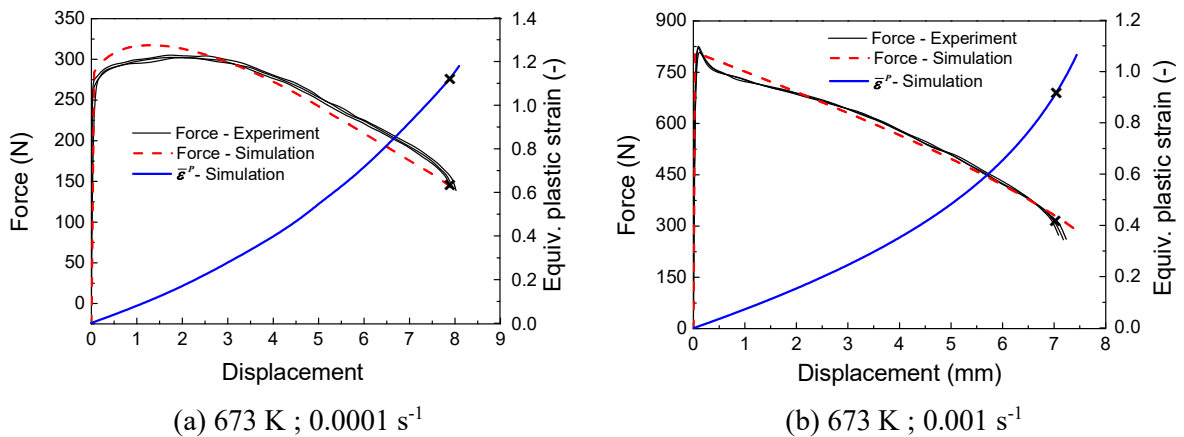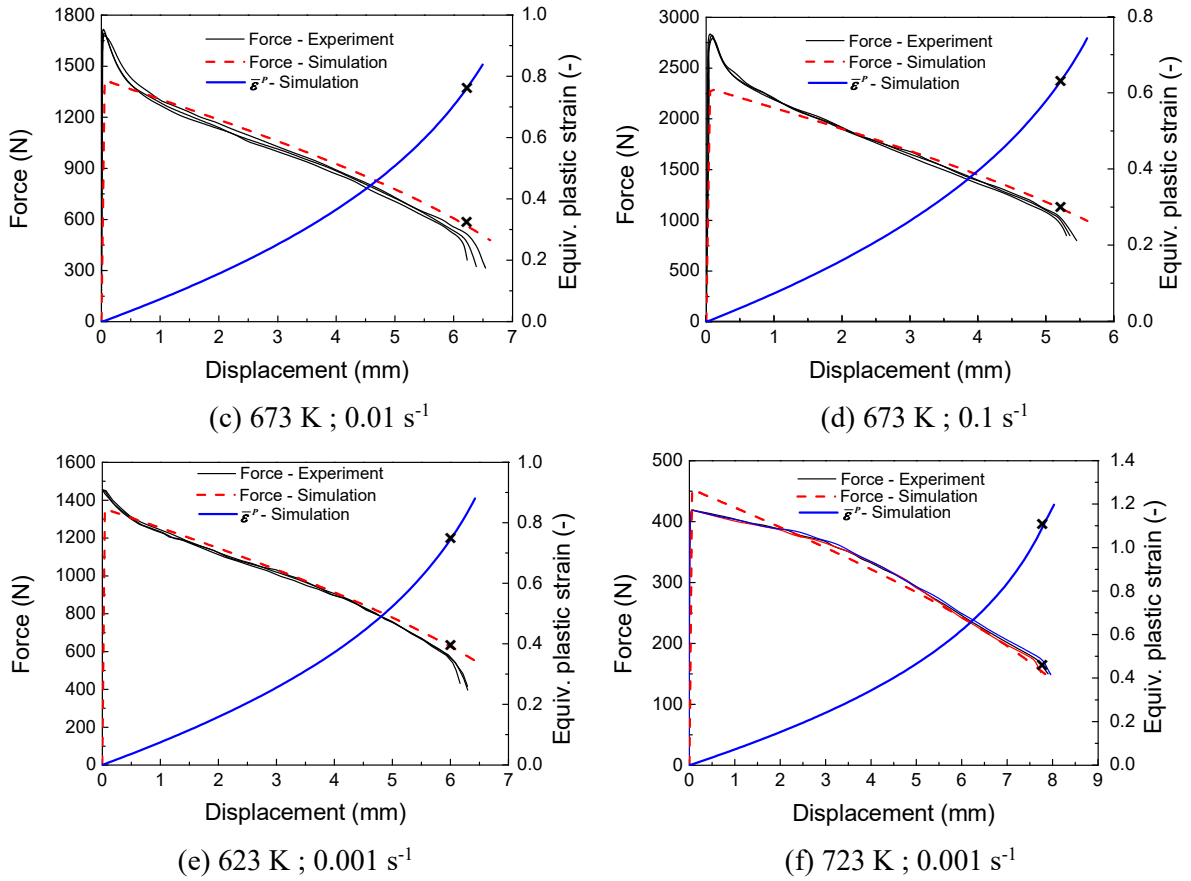
Figure IV-17 Force-displacement curves and evolution of the equivalent plastic strain for NT20 at different temperatures and strain rates

The results of simulations are summarized in Table IV-7. It could be concluded that the equivalent fracture strain strongly depends on strain rate, temperature and stress state. Indeed, it increases with the increase of temperature and decreases with the increase of strain rate.

Geometry \ Conditions	SH	UT	NT20	NT10	NT5	FB
673 K ; 0.0001 s^{-1}			1.1			
673 K ; 0.001 s^{-1}	0.59	1.12	0.93	0.84	0.71	0.96
673 K ; 0.01 s^{-1}			0.76			
673 K ; 0.1 s^{-1}			0.63			
623 K ; 0.001 s^{-1}			0.75			
723 K ; 0.001 s^{-1}			1.1			

Table IV-7 Summary of the equivalent fracture strains for different shapes and deformation temperatures and strain rates

IV.3.2 Proposed damage model

To predict the damage behavior, an uncoupled MMC criterion with the additional temperature and strain rate influence is proposed and identified based on the equivalent fracture strains obtained from numerical simulations.

IV.3.2.1 Model description

For the uncoupled damage criteria, the damage accumulation is formulated empirically by the following equation

$$\int_0^{\bar{\varepsilon}_f^P} f(\boldsymbol{\sigma}, \bar{\varepsilon}^P) d\bar{\varepsilon}^P \geq C_C \tag{IV.33}$$

where $\boldsymbol{\sigma}$, $\bar{\varepsilon}^P$ and $\bar{\varepsilon}_f^P$ are stress tensor, equivalent plastic strain and equivalent fracture strain, while C_C is the critical value. When the damage accumulation exceeds C_C, the failure is assumed to be initiated.

Based on the stress-based Mohr-Coulomb fracture criterion, Bai and Wierzbicki [113] have proposed a modified version of this damage criterion. The resulting modified Mohr-Coulomb (MMC) criterion could be written as follows

$$\bar{\varepsilon}_f^P(\eta, \bar{\theta})_{MMC} = \{\frac{A}{c_2}[c_3 + \frac{\sqrt{3}}{2-\sqrt{3}}(c_\theta^{ax} - c_3)(\sec(\frac{\bar{\theta}\pi}{6}) - 1)][\sqrt{\frac{1+c_1^2}{3}}\cos(\frac{\bar{\theta}\pi}{6}) + c_1(\eta + \frac{1}{3}\sin(\frac{\bar{\theta}\pi}{6}))]\}^{-\frac{1}{n'}} \tag{IV.34}$$

where A and n' are two power hardening coefficients, c_1, c_2 and c_3 are three fracture parameters. The value of c_θ^{ax} depends on which type of reference test is used to calibrate the strain hardening function [164]. For our case, uniaxial tension test is used, then $c_\theta^{ax} = 1$. In the special case of plane stress, the stress triaxiality and the Lode angle parameter are uniquely related through [112, 165]

$$\cos[\frac{\pi}{2}(1-\bar{\theta})] = -\frac{27}{2}\eta(\eta^2 - \frac{1}{3}) \tag{IV.35}$$

Thus, for the sheet material, the ductile fracture criterion only depends on the stress triaxiality.

The MMC criterion described above is limited to the condition of cold deformation. For the aluminum alloys deformed at elevated temperatures, both the constitutive and ductile fracture behavior are influenced by temperature and strain rate [119]. To include those influence in the MMC criterion, two methods can be used: one is to set the parameters of the original MMC criterion as function of temperature and strain rate; the other technique is to define an extension of the MMC criterion by introducing a Johnson-Cook type [166] of strain rate and temperature scale factor. In this study, the later method is used, and the MMC criterion under the plane stress condition can be extended to

$$\bar{\varepsilon}_f^P(\eta, \dot{\bar{\varepsilon}}^P, T) = \bar{\varepsilon}_f^P(\eta)_{MMC}[1 + D_1 \ln \dot{\bar{\varepsilon}}^*][1 + D_2 T^*] \tag{IV.36}$$

86

where D_1 and D_2 are two parameters, the dimensionless strain rate parameter $\dot{\bar{\varepsilon}}^*$ is the ratio between the equivalent plastic strain rate $\dot{\bar{\varepsilon}}^P$ and the reference strain rate $\dot{\bar{\varepsilon}}_{ref}$, while T^* is defined by the following equation

$$T^* = \frac{T - T_{ref}}{T_m - T_{ref}} \tag{IV.37}$$

where T is the testing temperature, T_{ref} is reference temperature and T_m is the melting temperature.

As our fracture locus is defined under monotonic loading conditions, a linear incremental relationship between the damage indicator, D, and the equivalent plastic strain is assumed here

$$D(\bar{\varepsilon}^P) = \int_0^{\bar{\varepsilon}^P} \frac{d\bar{\varepsilon}^P}{f(\eta, \dot{\bar{\varepsilon}}^P, T)} \tag{IV.38}$$

In the finite element simulation, the integration point is considered to fail when the limit of ductility is reached $\bar{\varepsilon}^P = \bar{\varepsilon}_f^P$, or $D(\bar{\varepsilon}_f^P) = D_c = 1$. Under a known stress state loading process, above equation can be integrated to give

$$\bar{\varepsilon}_f^P = \bar{\varepsilon}_f^P(\eta, \dot{\bar{\varepsilon}}^P, T) = f(\eta, \dot{\bar{\varepsilon}}^P, T) \tag{IV.39}$$

IV.3.2.2 Parameters identification process

The parameters identification process employed here is similar to the one performed by Bao and Wierzibicki [112, 115]. In most tests on various types of specimens, the stress state parameters are variable. In our research, it is proposed to determine the fracture locus based on the initial, final and average value of the stress triaxiality in the loading process. The average value is obtained from the weight loading path function

$$\eta_{av} = \frac{1}{\bar{\varepsilon}_f^P} \int_0^{\bar{\varepsilon}_f^P} \eta(\bar{\varepsilon}^P) d\bar{\varepsilon}^P \tag{IV.40}$$

where $\eta(\bar{\varepsilon}^P)$ is the stress triaxiality evolution from the numerical simulation and $\bar{\varepsilon}_f^P$ is equivalent fracture strain which has been determined in last section. For all tested specimens geometries, the $\eta(\bar{\varepsilon}^P)$ at 673 K and 0.001 s^{-1} is shown in Figure IV-18. Except the free bulging test, the stress triaxiality changes with the evolution of the equivalent plastic strain. However, the variations of triaxiality are in an accepted range.
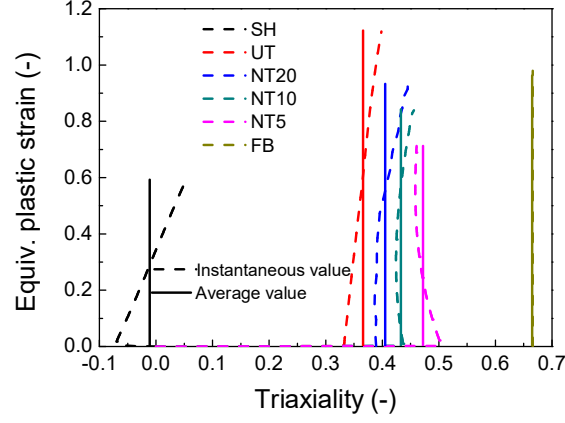
Figure IV-18 Evolution of the stress triaxiality and the corresponding average values for different shapes of specimen deformed at 673 K and 0.001 s^{-1}

MMC criterion employed in our work contains five original parameters (A, n', c_1, c_2, c_3) and two new parameters (D_1, D_2), which include the influence of strain rate and temperature. The reference strain rate is set to $\dot{\bar{\varepsilon}}_{ref} = 0.001\,\text{s}^{-1}$ and the reference temperature to $T_{ref} = 623\,\text{K}$. The criterion parameters have been calibrated by minimizing the objective function $\mathfrak{R}_D$:

$$\mathfrak{R}_D(A, c_1, c_2, c_3, n', D_1, D_2) = \sqrt{\frac{1}{N}\sum_{i=1}^{N}(^{\exp}\bar{\varepsilon}_{f,i}^{P} - ^{pre}\bar{\varepsilon}_{f,i}^{P}(\eta, \dot{\bar{\varepsilon}}^{P}, T))^2} \qquad \text{(IV.41)}$$

where N is the number of calibration experiments. For parameter identification, a genetic algorithm with 10 000 individuals, a crossover probability of 0.8 and a mutation probability of 0.02 has been used. The parameters of the MMC criterion for the AA5383 alloy are listed in Table IV-8.

A [MPa]	c_1 [-]	c_2 [MPa]	c_3 [-]	n' [-]	D_1 [-]	D_2 [-]	$\mathfrak{R}_D$ [-]
150	-0.0036	75.27	0.960	0.135	-0.069	1.106	0.057

Table IV-8 Identified parameter values of MMC criterion and the corresponding residual value

The resulting fracture locus with respect to triaxiality at 673 K and 0.001 s^{-1} is shown in Figure IV-19 (a). It could be remarked that the predictions of the fracture criterion are following the trend of the experimental data. The fracture locus is divided into three domains according to the value of triaxiality: 0~0.33, 0.33~0.6 and 0.6~0.67. In the middle range, the equivalent fracture strain decrease with the triaxiality. While there exists opposite tendency for the other two ranges. In general, the fracture locus can precisely predict the fracture strains at the deformation condition of 673 K and 0.001 s^{-1}.

The response of the criterion when varying the temperature and the strain rate is illustrated by Figure IV-19 (b, c). The calibrated model seems to predict accurately the fracture strains. The average error does not exceed 5.2%.

(a)

(b)

(c)
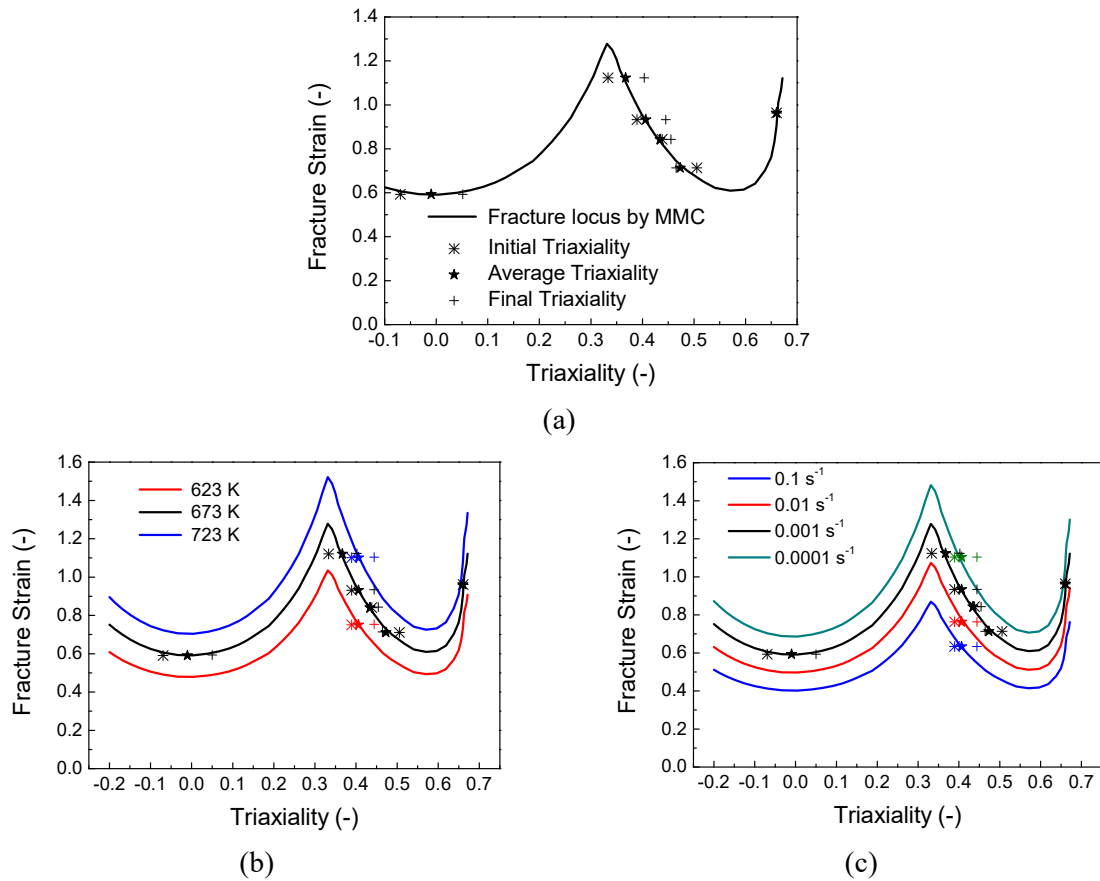
Figure IV-19 Comparison between the fracture locus against stress triaxiality obtained from the MMC criterion and the experimental data at: (a) 673 K and 0.001 s^{-1}; (b) different temperatures and (c) different strain rates

IV.3.2.3   Validation by the experiments used for parameter identification

In this part, the numerical simulations of above tests are performed again after the implementation of the identified MMC criterion. Figure IV-20 and Figure IV-21 present the experimental and numerical force-displacement curves for all the tested configurations.

For the different shapes of specimens deformed at 673 K and 0.001 s^{-1}, it is shown from Figure IV-20 that the damage model can accurately predict the fracture displacement. The largest average error is around 9.5% and it is obtained from NT5 test. While for NT20 test at different temperatures and strain rates (Figure IV-21), the largest error (around 7%) is under the condition of 673 K and 0.01 s^{-1}. The fracture displacement error is related to the predictability of MMC criterion. In generally, the proposed damage model can accurately predict the fracture displacement for all the studied conditions.
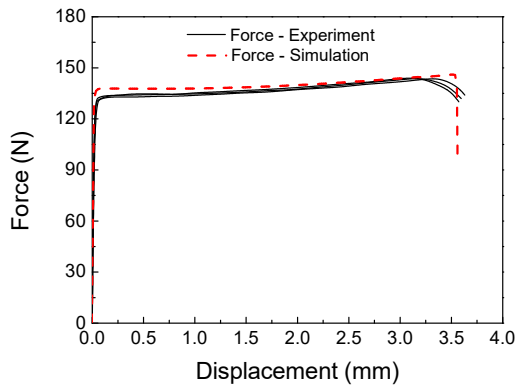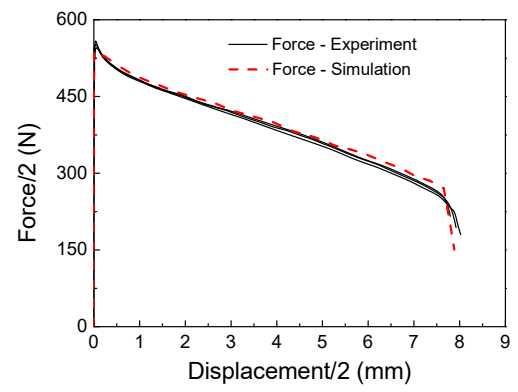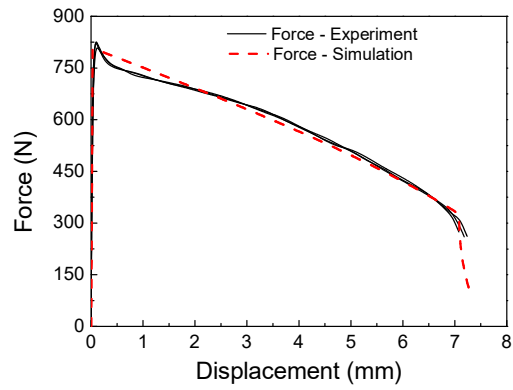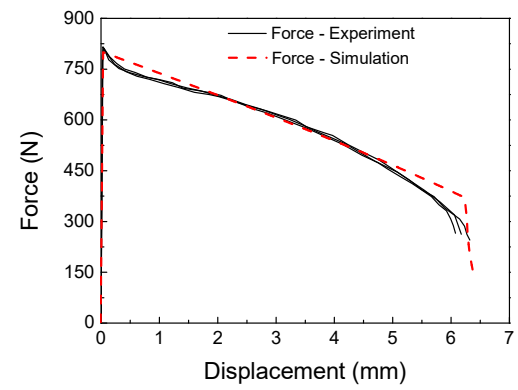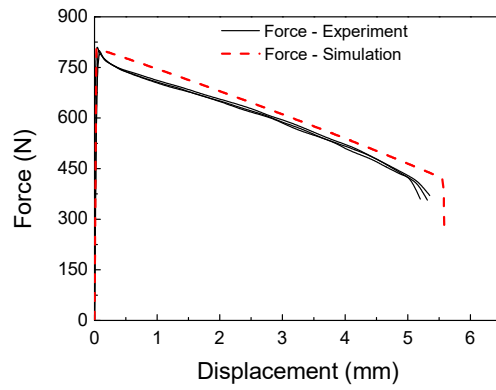
Figure IV-20 Force-displacement curves for different shapes of specimen at 673 K and 0.001 s⁻¹:
(a) SH; (b) UT; (c) NT20; (d) NT10 and (e)NT5
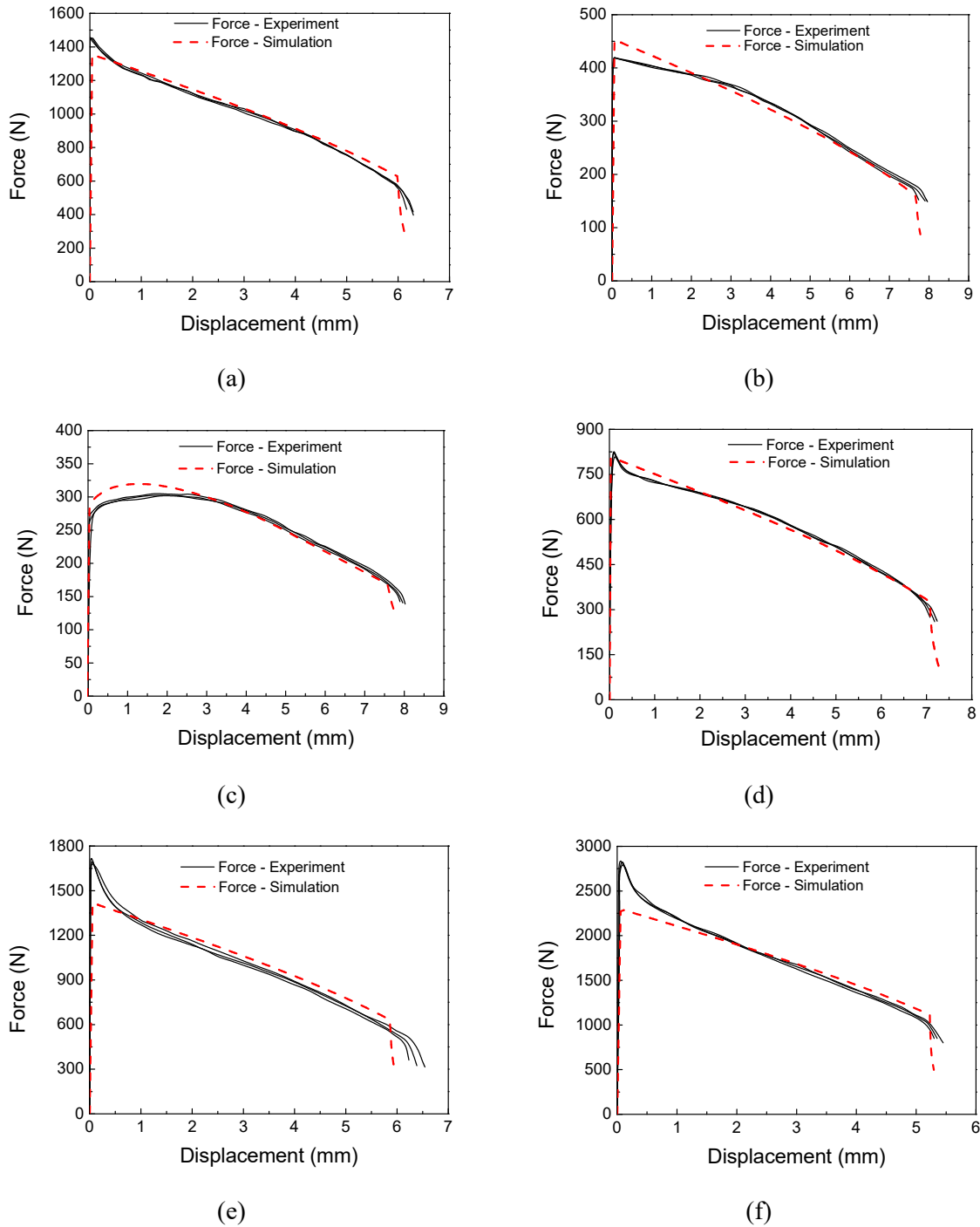
Figure IV-21 Force-displacement for NT20 at different temperatures and strain rates: (a) 623 K and 0.001 s^{-1}; (b) 723 K and 0.001 s^{-1}; (c) 673 K and 0.0001 s^{-1}; (d) 673 K and 0.001 s^{-1}; (e) 673 K and 0.01 s^{-1}; (f) 673 K and 0.1 s^{-1}

IV.3.2.4   Validation using notched specimen NT2

The notched NT2 specimen has not been used for the calibration of the MMC criterion. In this section, this test is simulated to verify the efficiency of the identified model. Full model is used in the simulation in order to compare with the experimental results. As shown in Figure IV-22 (a), the model underestimates fracture displacement by about 6.5% compared to the average of experimental results.

Figure IV-22 (b) shows that fracture is initiated from the boarder of notched as it has been observed in the experimental tests.

(a)

(b)   (c)
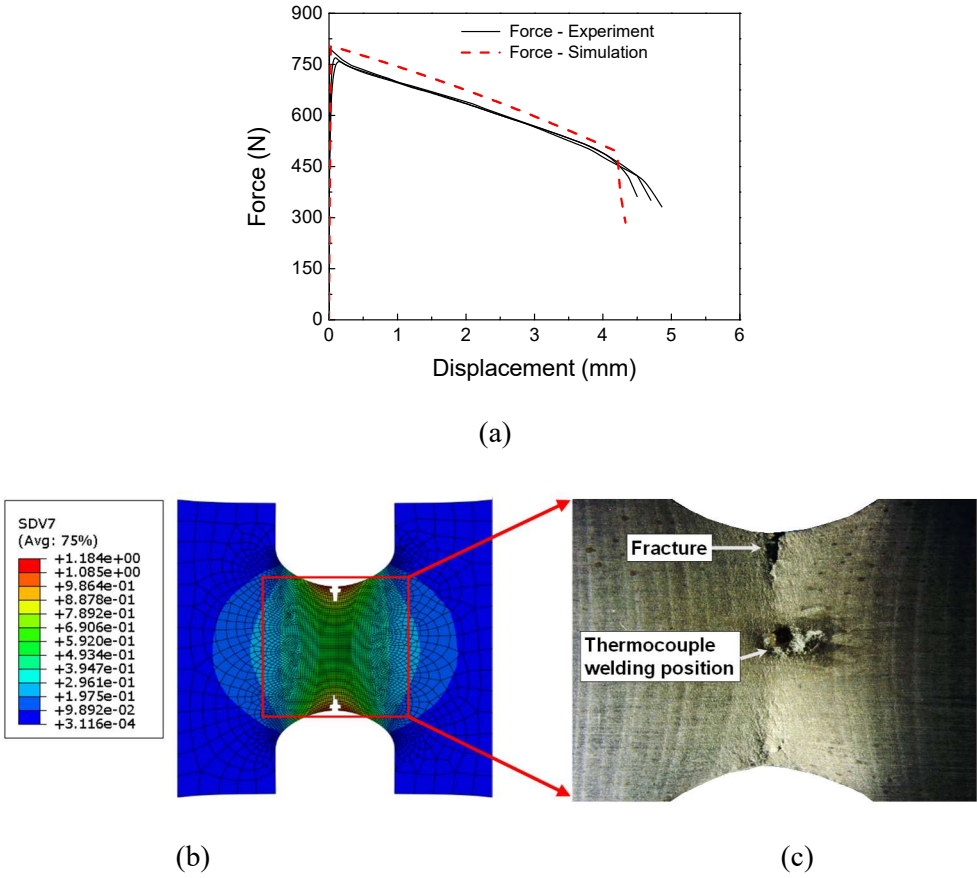
Figure IV-22 Experimental and numerical results for NT2 specimen at 673 K and 0.001 s^{-1}: (a) force-displacement curves; (b) numerical equivalent plastic strain distribution and (c) experimental specimen at the initiation of fracture

IV.4 Summary

In this chapter, constitutive and fracture models are proposed and identified to describe the hot deformation behavior of AA5383 alloy.

For the description of the flow behavior at different temperatures and strain rates, the strain-compensated Arrhenius type model and the composite model are both proposed. The composite model is chosen as the flow model due to its relative easy implementation. Based on the experimental results obtained from deformation condition of 673 K and 0.001 s^{-1}, BBC2003 yield criterion is proposed and identified. Anisotropic Hill48 yield criterion is used as a reference. It is shows that BBC2003 yield criterion can predict the experimental Lankford coefficients and yield stresses accurately, while Hill48 yield criterion exhibits a higher yield stresses in the 45° and 90° directions and a lower biaxial yield stress prediction. The models are implemented into user subroutine UMAT by a semi-implicit integration scheme.

With the identified constitutive model, the numerical simulations are performed to obtain the equivalent fracture strains at different stress states, temperatures and strain rates. As the material is deformed under the plane stress condition, the stress states is represented only by the stress triaxiality. At a fixed deformation temperature and strain rate, the equivalent plastic fracture strain is not linear with the response to the stress triaxiality. While at a fixed stress state, the equivalent plastic fracture strain generally increases with the increase of temperature and decrease of strain rate.

Finally, with the equivalent fracture strains obtained at different deformation conditions, the MMC damage model, which includes the influence of temperature and strain rate, is proposed. The parameters are identified by using genetic optimization method to minimize the root mean squared error directly. The numerical simulations, which have been used for identifying the equivalent fracture strains, are performed again by including the damage influence. It is seen that the MMC damage model can accurately predict the fracture displacement for all the studied conditions.

With above identified models, the hot forming simulations on the complex geometry of die will be performed in the next chapter to obtain the pressure law, which will be used as an input in the forming experiments.

Chapter V.
Numerical simulation and experimental forming

In this chapter, bulging of complex parts (axisymmetric die and cross shape die) is investigated. The forming experiments are carried out on the SPF instrumented demonstrator of the laboratory. The device is designed to be able control the time evolution of: *(i)* the furnace temperature and *(ii)* the forming gas pressure. The numerical simulations are performed on ABAQUS©. The thermal-mechanical behavior of AA5383 alloy is described by the identified constitutive law and the MMC damage criterion which are implemented in a user subroutine (UMAT). Specific subroutines (UEXTERNALDB, DLOAD and URDFIL) have been developed to control the forming cycle and exchange post processing data. Various strategies for adjusting the bulging pressure in relation to the strain rate are proposed and discussed. The numerical results, including the forming time, thickness distribution and fracture conditions are discussed in detail. The forming (Pressure vs Time) curve is extracted from the numerical simulations as a tabulated law. This table is then used as input to perform the gas forming of the considered shape on the SPF machine. Finally, the numerical and experimental results are compared with regarding to the maximum principal logarithmic strain, thickness evolution and the fracture initiation locus.

V.1 Numerical simulation of the forming process

V.1.1 Material models

Material model	Formulation
Flow behavior (Composite model)	$\bar{\sigma} = K(\bar{\varepsilon}^P + \bar{\varepsilon}_0^P)^{\hat{n}} \exp(-b\bar{\varepsilon}^P)(\dot{\bar{\varepsilon}}^P)^m \{1 - (\frac{T - T_{ref}}{T_m - T_{ref}})^{\hat{\beta}}\}$
Yield criterion (BBC2003)	$\bar{\sigma} = [a(\Gamma + \Psi)^{2k} + a(\Gamma - \Psi)^{2k} + (1-a)(2\Lambda)^{2k}]^{\frac{1}{2k}}$
Damage behavior (MMC criterion)	$\bar{\varepsilon}_f^P(\eta,\bar{\theta})_{MMC} = \{\frac{A}{c_2}[c_3 + \frac{\sqrt{3}}{2-\sqrt{3}}(c_\theta^{ax} - c_3)(\sec(\frac{\bar{\theta}\pi}{6}) - 1)][\sqrt{\frac{1+c_1^2}{3}}\cos(\frac{\bar{\theta}\pi}{6}) + c_1(\eta + \frac{1}{3}\sin(\frac{\bar{\theta}\pi}{6}))]\}^{-\frac{1}{n}}$ $\bar{\varepsilon}_f^P(\eta,\bar{\theta}) = \bar{\varepsilon}_f^P(\eta,\bar{\theta})_{MMC}[1 + D_1 \ln \dot{\varepsilon}^*][1 + D_2 T^*]$

Table V-1 Summary of the material models used for forming simulations

In the previous chapter, the material model suited to AA5383 alloy in the studied forming conditions has been proposed and identified. These constitutive equations, summarized in Table V-1, are used to describe the material behavior in the forming simulations.

The implementation algorithm and the values of the identified parameters can be referred to Chapter IV.

V.1.2   Simulation of the forming process

According to the experimental hot forming conditions, two types of geometries have been chosen for the process simulations: a complex axisymmetric shape and a cross-shape. The corresponding numerical models are shown in Figure V-1.

<div align="center">(a)   (b)</div>
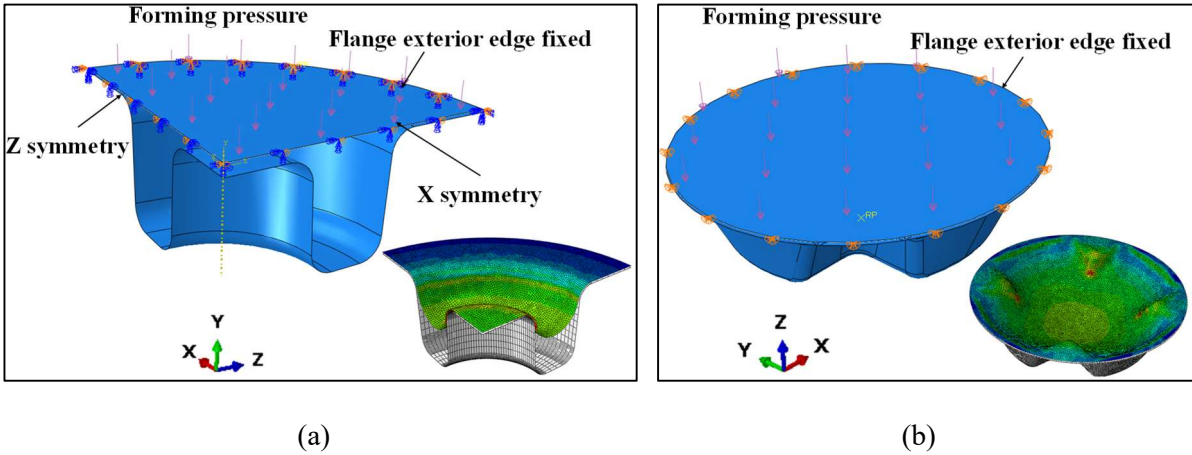
Figure V-1 Numerical models used for forming simulation. (a) Axisymmetric shape; (b) Cross-shape

For the axisymmetric case, only a quarter of the flange is used due to the geometric symmetry in order to reduce CPU time. The boundary conditions of X-symmetry and Z-symmetry are imposed. For the cross-shape, the whole part is considered due to the asymmetry of all the blend radii and clearance angles. Generally, the stress state in the deformed flange is more complex in the cross shape case compared to the axisymmetric one.

For both types of simulations:

- The general static step of ABAQUS© Standard is adopted as the time integration process.
- The proposed material law is chosen as a user material, implemented in a subroutine (UMAT) as shown in the previous chapter.
- The die is set as a discrete rigid surface with element size of 4.0 mm while the sheet as a deformable shell element (S4R with five through-thickness integration points in the ABAQUS element library) with initial thickness of 3.2 mm and global mesh size of 1.0 mm. The

selections of element size for the die and sheet are based on convergence study by using different mesh size.

- The interaction between sheet (Slave) and die (Master) is controlled by a hard contact algorithm (surface to surface) with Coulomb friction (f = 0.1).

- For the boundary conditions, the outside circle of the sheet and the reference point of the die are fixed.

- The experimental forming pressure is applied on the upper face of the sheet. The magnitude of this pressure is controlled by a user subroutine (DLOAD) according to the strain rate control strategy.

- In order to avoid the convergence problem at the beginning of each simulation, a clearance of 0.01 mm is set between the blank and the rigid die.

- An initial step with a 0.001MPa pressure for 1.0 s is imposed before the actual forming step with the controlled pressure law.

V.1.3 Forming pressure control strategies

In SPF like processes, the forming speed is commonly controlled by the bulging pressure. Generally, this forming speed is associated to the equivalent plastic strain rate, which is a major parameter of the material laws. In the forming simulation, the applied pressure P is to be varied throughout the process to maintain the real equivalent plastic strain rate $\dot{\bar{\varepsilon}}_{real}^{P}$ at the target equivalent plastic strain rate value $\dot{\bar{\varepsilon}}_{tar}^{P}$. The ratio between $\dot{\bar{\varepsilon}}_{real}^{P}$ and $\dot{\bar{\varepsilon}}_{tar}^{P}$ is defined as follow

$$\gamma_{real} = \dot{\bar{\varepsilon}}_{real}^{P} / \dot{\bar{\varepsilon}}_{tar}^{P} \tag{V.1}$$

The evolution of the forming pressure is adjusted according to the value of γ_{real} by the following function

$$\hat{P}_{n+1} / \hat{P}_{n} = f(\gamma_{real}) \tag{V.2}$$

where $\hat{P}_{n+1}$ is the new pressure value corresponding to the iteration $n+1$ and $\hat{P}_{n}$ is the old pressure value corresponding to the iteration n. Different pressure control strategies are presented as follows.

V.1.3.1 ABAQUS pressure control strategy

This pressure control algorithm was first proposed by Bellet [167] and now is implemented by default in ABAQUS©. The relation follows

$$\hat{P}_{n+1} / \hat{P}_n = \begin{cases} 2.0 & \gamma_{real} < 0.2 \\ 1.5 & 0.2 \leq \gamma_{real} < 0.5 \\ 1.2 & 0.5 \leq \gamma_{real} < 0.8 \\ 1.0 & 0.8 \leq \gamma_{real} < 1.5 \\ 1/1.2 & 1.5 \leq \gamma_{real} < 3.0 \\ 0.5 & \gamma_{real} \geq 3.0 \end{cases} \tag{V.3}$$

This controlling algorithm is simple and relatively rough. It can be used directly and generate the desired pressure time profile at a low computational cost.

V.1.3.2   Pressure control strategies developed by LAMPA

The band pressure algorithm described above can lead to the instabilities of forming strain rate, as well as the forming pressure. In order to stabilize the strain rate and pressure, Robert [168] proposed a smooth pressure control algorithm by using the third order algorithm:

$$\hat{P}_{n+1} / \hat{P}_n = -5(\gamma_{real} - 1)^3 - 0.5(\gamma_{real} - 1) + 1 \tag{V.4}$$

To take into account the response time by the forming machine, the following condition is added

$$\left| \frac{d\hat{P}}{dt} \right| \leq \left| \frac{d\hat{P}}{dt} \right|^{real} \tag{V.5}$$

To avoid setting an initial forming pressure, the forming pressure value for the first incremental is set as

$$\hat{P}_1 = dt \left| \frac{d\hat{P}}{dt} \right|^{real} \tag{V.6}$$

where dt is numerical integration step and $\left| \frac{d\hat{P}}{dt} \right|^{real}$ is the real pressure variation.

V.1.3.3   New pressure control strategy

In the presented work, the pressure algorithm is applied to simulate forming pressure for a complex part. A further modification is implemented to consider the strain rate gradient or the applying of a progressive pressure. After testing various mathematical approaches, the following equation is proposed:

$$\hat{P}_{n+1} / \hat{P}_n = \begin{cases} 2.43 & \gamma_{real} < 0.3 \\ -10\log_{10}^3(\gamma_{real}) + 1 & 0.3 \leq \gamma_{real} < 1.26 \\ 0.99 & \gamma_{real} \geq 1.26 \end{cases} \tag{V.7}$$

There are two limits for the range of γ_{real} which are used to smooth the pressure change. The pressure algorithm used in our forming pressure process is shown in Figure V-2.

This pressure algorithm is implemented in ABAQUS© using different user subroutines listed below:

- UEXTERNALBD for the external interface and the computation of the pressure law.
- UMAT for the material behavior and the controlled fields computation.
- DLOAD to apply the pressure.
- URDFIL to obtain fields values at integration points.

$$\text{Input:}\quad \left|\frac{d\hat{P}}{dt}\right|^{max} \quad\text{and}\quad \dot{\bar{\varepsilon}}^P_{tar}$$

$$\left|\frac{d\hat{P}}{dt}\right| = \left|\frac{d\hat{P}}{dt}\right|^{max}$$

Finite element calculation

$$\gamma_{real} = \dot{\bar{\varepsilon}}^P_{real} / \dot{\bar{\varepsilon}}^P_{tar} \qquad \hat{P}_{n+1}/\hat{P}_n = \begin{cases} 2.43 & \gamma_{real} < 0.3 \\ -10\log_{10}{}^3(\gamma_{real})+1 & 0.3 \le \gamma_{real} < 1.26 \\ 0.99 & \gamma_{real} \ge 1.26 \end{cases}$$

$$\left|\frac{d\hat{P}}{dt}\right| > \left|\frac{d\hat{P}}{dt}\right|^{max}$$ No

Yes

$$\frac{d\hat{P}}{dt} = sign(\frac{d\hat{P}}{dt})\left|\frac{d\hat{P}}{dt}\right|^{max}$$

Finite element calculation
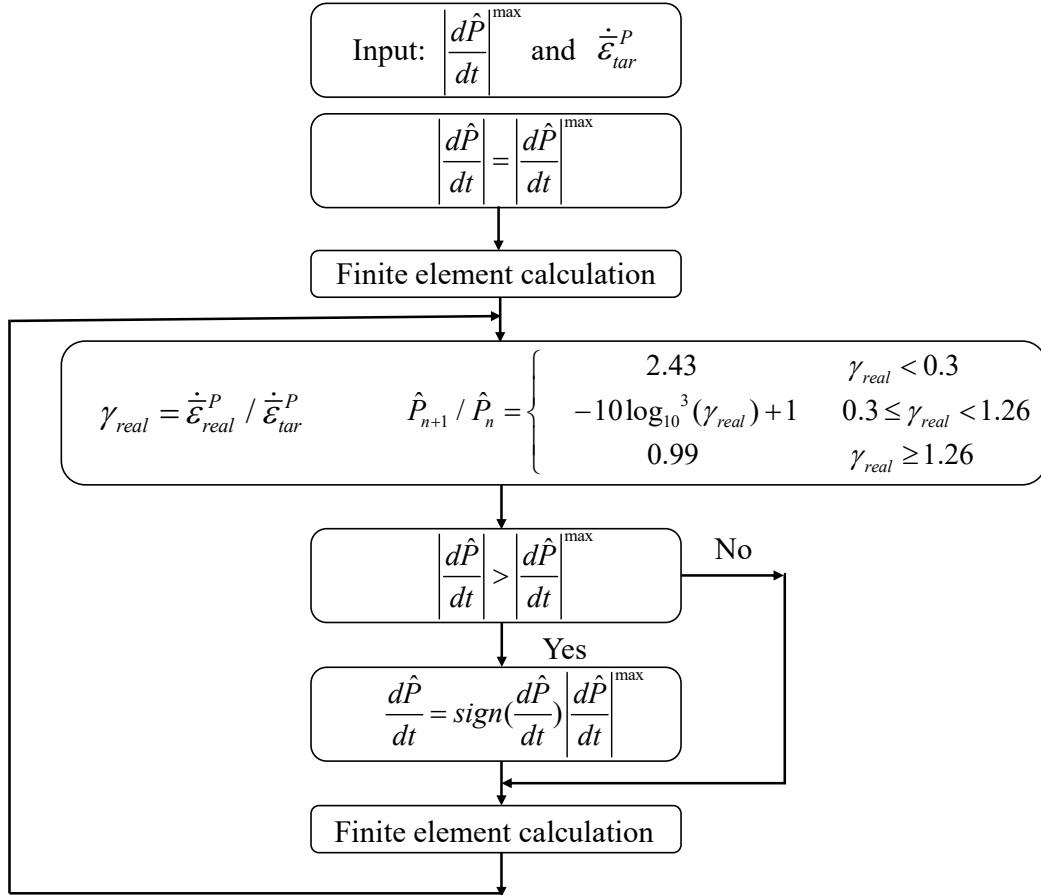
Figure V-2 Pressure algorithm

V.1.3.4   Pressure control influence

In this section, the effect of above three different pressure control strategies is studied. All the forming simulations are performed on the axisymmetric shape at 673 K with a constant target equivalent plastic strain rate $\dot{\bar{\varepsilon}}^P_{tar} = 1\times10^{-3}\ s^{-1}$. The effect of the different forming strategies is shown in Figure V-3. The pressure curves exhibit different shape, being ABAQUS© curve the roughest. The other two pressure control strategies show a smooth change before the forming time of 1000 s. After the forming time of 1000 s, the third order pressure control algorithm exhibits more instability. By using the new strategy, the pressure is smooth and stable throughout the whole deformation range.

The same pattern is visible in the Figure V-3(b) where are presented the strain rate ratios for the same simulations. The ABAQUS© pressure control strategy shows a quite rough answer. While the third order pressure control strategy gives a good strain rate control only in the middle of the time range. The strain rate ratio is quite stable and always near to one for almost whole forming simulation range when we use the new pressure control strategy. The only unstable of strain rate happens at the beginning of deformation, which is due to the initial contact between the sheet and the die.

Based on the above analysis for the output pressure and strain rate ratio evolution as the function of time, the new smooth pressure forming strategy is chosen for all forming simulations.

(a)   (b)
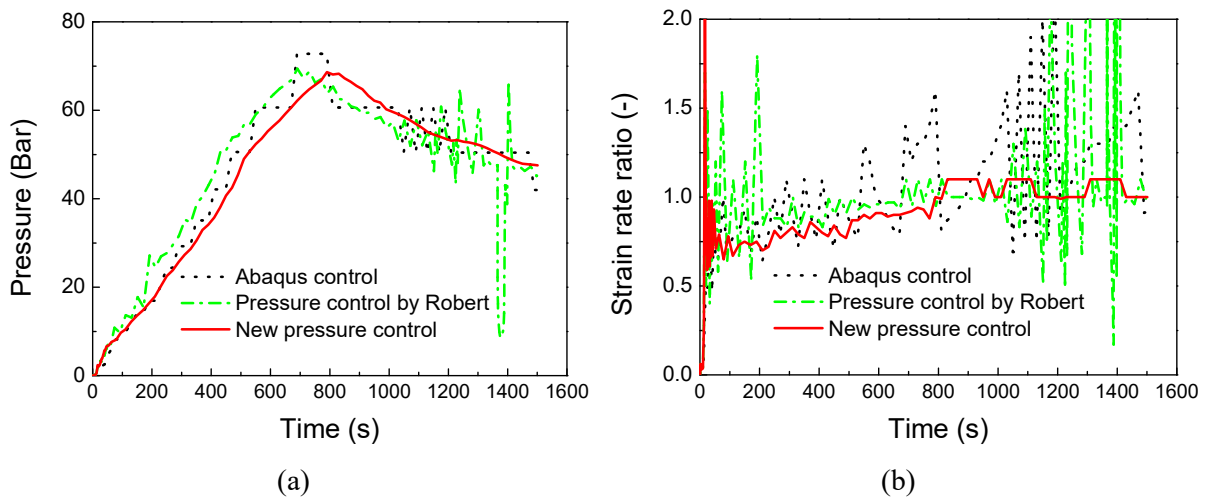
Figure V-3 Comparison of different pressure control schemes for (a) pressure evolution and (b) strain rate ratio evolution

V.1.4 Different integration point number selections

The most common method to estimate the real strain rate is to use maximum strain rate of the whole numerical model which is obtained at only one integration point. In the case of a complex shape forming, the computed pressure would be quite low due to the strain rate concentration. In this section, the real strain rate is extracted at a defined series of integration points, and the target equivalent plastic strain rate is fixed at $\dot{\bar{\varepsilon}}_{tar}^{P} = 1 \times 10^{-3}\ s^{-1}$. User subroutine URDFIL is used to read strain rate components and calculate the equivalent strain rate for every integration point and average it. Then a percentage of integration points with the highest values of equivalent strain rate is at first chosen, while rejecting the points at maximum values. The new pressure law control strategy is used and the simulations are performed with different integration point number selections [169] as proposed by Jarrar et al. [170]:

- One integration point (classical method)
- 0.5 % integration points (25 integration points in current case) and rejecting the 0.05% with the highest strain rate values (2 integration points)

99

- 2 % integration points (101 integration points in current case) and rejecting the 0.5% with the highest strain rate values (25 integration points)
- 5 % integration points (254 integration points in current case) and rejecting the 1 % with the highest strain rate values (50 integration points)

The computed pressure curve for the above cases is shown in Figure V-4. It can be seen that the pressure obtained by using the maximum strain rate from one integration point is obviously lower than the one obtained from other conditions. This can be explained by the fact that the strain rate is highly concentrated in the first contact region between the sheet and the axisymmetric die. As the deformation continues, the high strain rate region moves to the un-contact region and distributes more homogenous. When increase the chosen percentage of the element to calculate the real strain rate, the forming pressure at the beginning also increases and the total forming time decreases. The sudden increase of pressure at the end of the simulation indicates the full contact of sheet with the die. The full contact time for different integration points number selection changes also severely. For example, the full contact time for 5 % integration points is around 2500 s while for 2 % integration points is around 4000 s.

The results obtained in this section showed that the use of several integration points technique changes the pressure-times curves significantly. In the forming simulation of Jarrar et al. [170], a 20 % of integration points average and the main 5 % integration points rejection is used, which would be an excessive approach in our forming simulation.
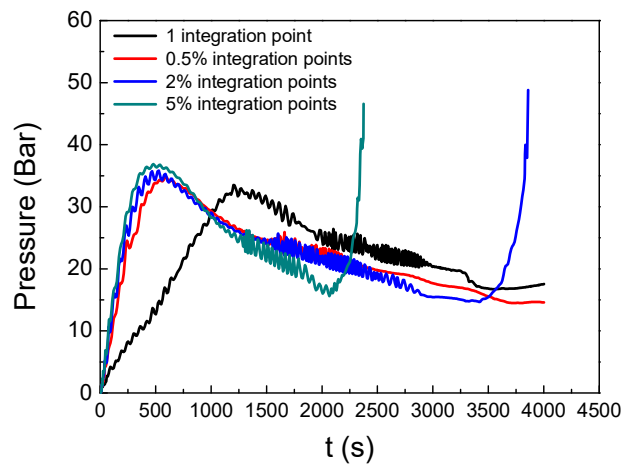
Figure V-4 Pressure time curves obtained by new pressure control strategy with different integration point numbers for obtaining the targeting strain rate

With the discussion above, we can see that the pressure-time profiles can be modified in several ways. It also would be interesting to avoid the effect of distorted integration points in the controlled scheme. During this work for the axisymmetric shape forming, the new pressure control strategy with an average strain rate (obtained from 2 % of integration points) is used to compute the pressure vs time curves. For the cross-shape forming simulation, the same method is adopted. It's found that the new pressure control strategy with 5% of integration point average can have a good result.

V.1.5 Different strain rate approaches

The main objective of this thesis is to reduce the forming time without sacrificing the part quality. In this section, the numerical simulations with different aimed strain rate evolution are performed at the homogenous temperature of 673 K. The axisymmetric shape forming is chosen due to an easier result comparison. The detailed aimed strain rate evolution is listed in Table V-2. The new pressure control strategy with the average of 2 % of integration points is used. Three simulations for different target strain rate are performed until the vertical displacement of 35.2 mm, as shown in Figure V-5 (a). The total forming time for high constant strain rate, changed strain rate and low constant strain rate simulations are 1274 s, 5001 s and 11718 s, respectively. The maximum principal logarithmic strain and thickness are measured on the node points from the center to the board along the rolling direction and the detailed values are shown in Figure V-5 (c, d). For the most deformed area, the maximum principal real strain for the high constant strain rate forming is obviously higher than the other two forming conditions, while the thickness evolve in the opposite way. When compared the results between the changed strain rate forming and the low constant strain rate forming, there exists a limited difference for the whole deformed area. Thus, from the numerical simulation point, the changed strain rate strategy can reduce the forming time around 57% without sacrificing the forming part quality compared to the constant low forming strain rate strategy.

Strain rate strategy	Strain rate values
High constant strain rate	$\dot{\bar{\varepsilon}}^P = 0.001\,s^{-1}$
Changed strain rate	$\dot{\bar{\varepsilon}}^P = \begin{cases} = 0.01\,s^{-1} & \bar{\varepsilon}^P < 0.5 \\ = 0.001\,s^{-1} & 0.5 \le \bar{\varepsilon}^P < 0.9 \\ = 0.0001\,s^{-1} & \bar{\varepsilon}^P \ge 0.9 \end{cases}$
Low constant strain rate	$\dot{\bar{\varepsilon}}^P = 0.0001\,s^{-1}$

Table V-2 Different aimed strain rate control strategies
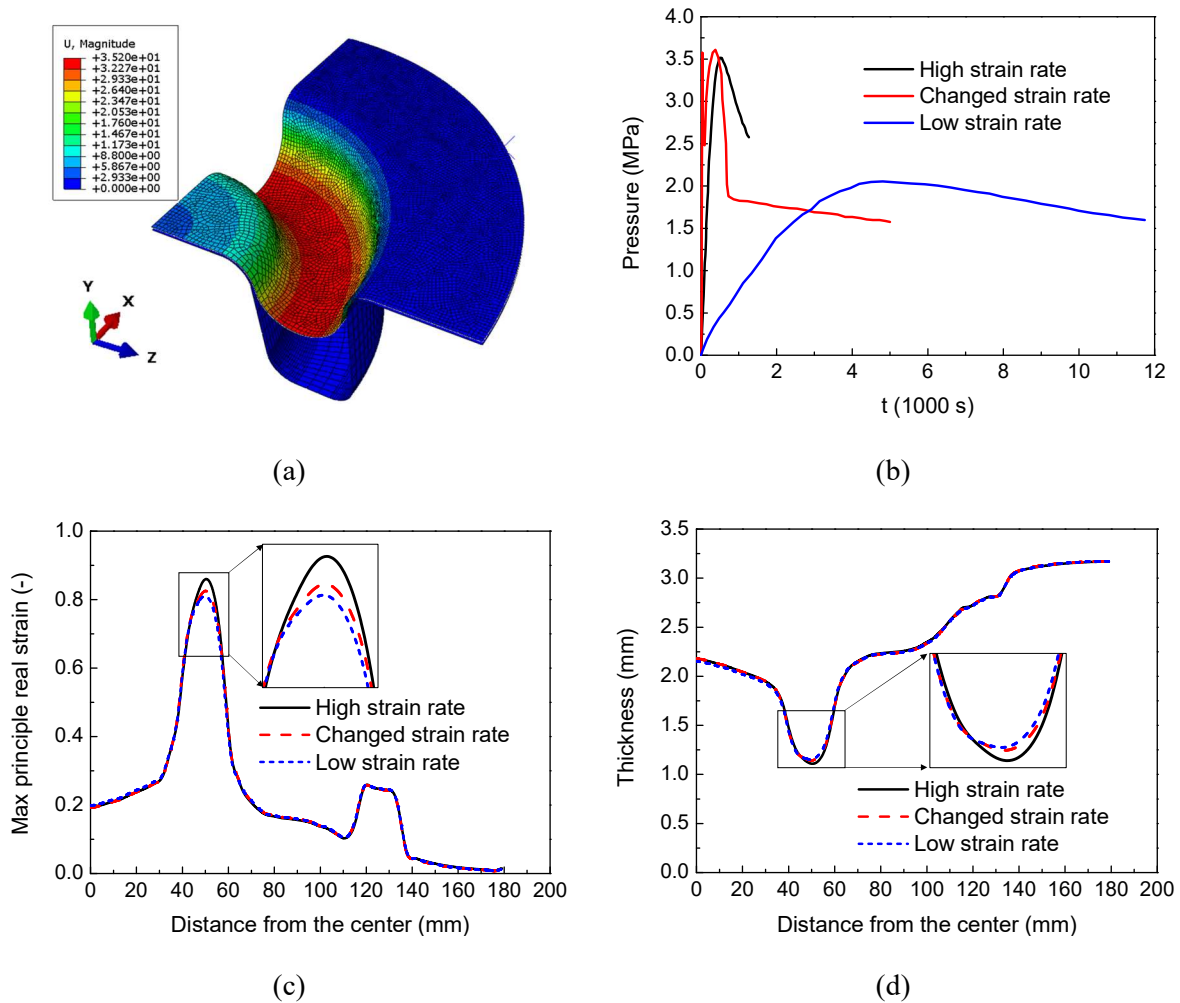
Figure V-5 Comparison of three different strain rate simulations for axisymmetric shape forming: (a) deformed specimen; (b) pressure evolution; (c) maximum principal real strain and (d) thickness distribution.

V.2 Experimental bulging tests

V.2.1 Experimental forming conditions

The configuration of the gas forming machine and the pressure scheme has been introduced in Chapter III. While the details of the operation order for the machine and the system of controlling the experimental temperature and gas pressure can be seen in the thesis of Yang [171]. Unlike the free bulging forming, two types of die (Figure V-6) are put inside the furnace to form flanges into the designed shapes. The initial flange is a round shape sheet of AA5383 alloy with the diameter of 290 mm and the thickness of 3.2 mm which is placed on the die upper face. After closing the furnace, the atmosphere inside is full of argon in order to avoid oxidation at the high temperature. Before the gas forming, the furnace is heated to the aimed temperature and kept for one hour to ensure the homogenous temperature distribution in the whole sheet. The thermal sensor is used to measure the temperature inside the furnace.

(a)   (b)

(c)
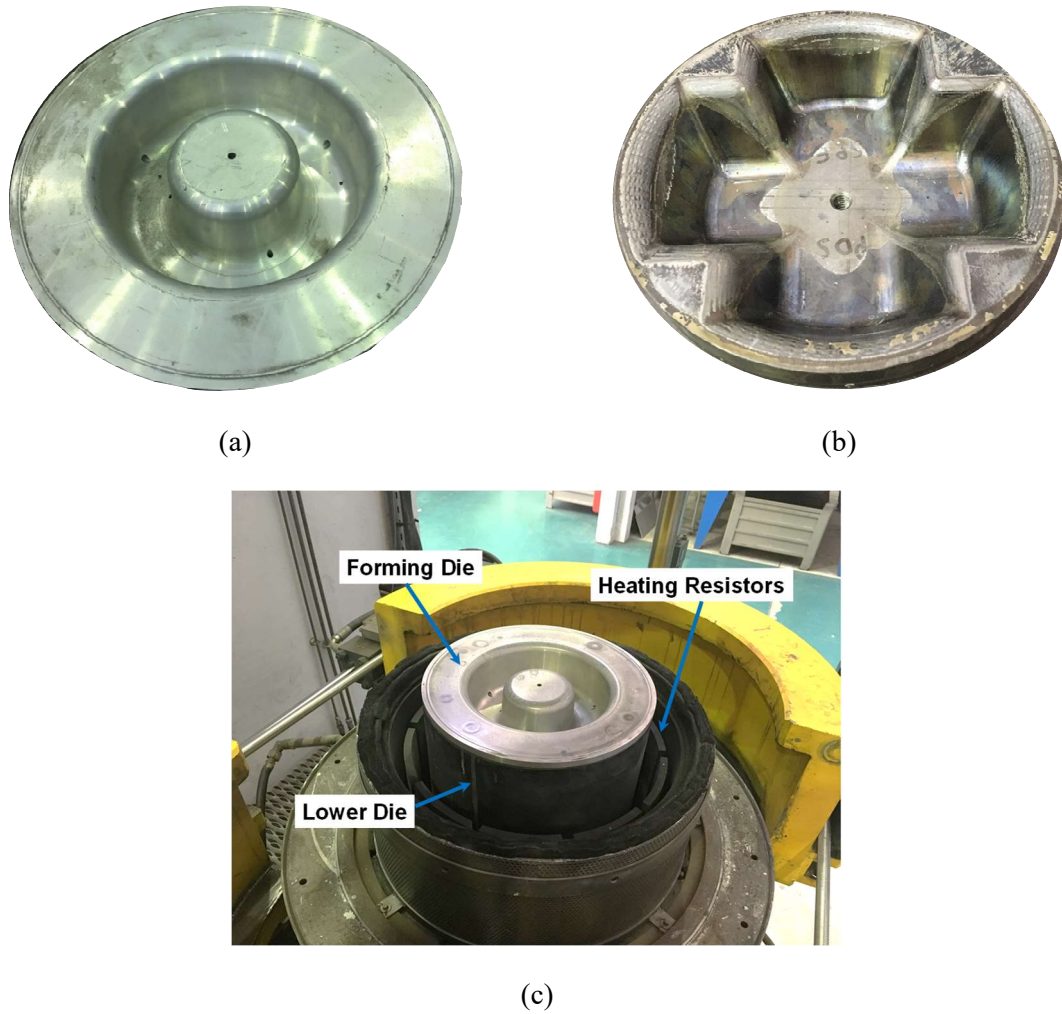
Figure V-6 (a) Axisymmetric die; (b) Cross Die and (c) Configuration for forming experiment

V.2.2   Experimental results

In order to measure the surface strain after bulging, Boron nitride white painter and a black painter have been put on the sheet surface. For the forming experiments, one test is carried out for the axisymmetric shape and two tests for the cross-shape. A GOM measurement system is used to obtain the maximum principal logarithmic strain and thickness distribution of the deformed parts.

V.2.2.1   Axisymmetric shape forming

In order to verify the performances of the proposed material laws, the axisymmetric shape forming is carried out at the constant target strain rate of 0.001 s^{-1} prior to the phenomenon of fracture. The input pressure law for the bulging test is computed from the numerical simulation. The comparison between the input pressure and the real pressure imposed on the flange is shown in Figure V-7 (a). The real pressure evolution can generally follow the input pressure except for the highest pressure level due to the machine limitation. The two sides of the deformed shape are shown in Figure V-7 (b).
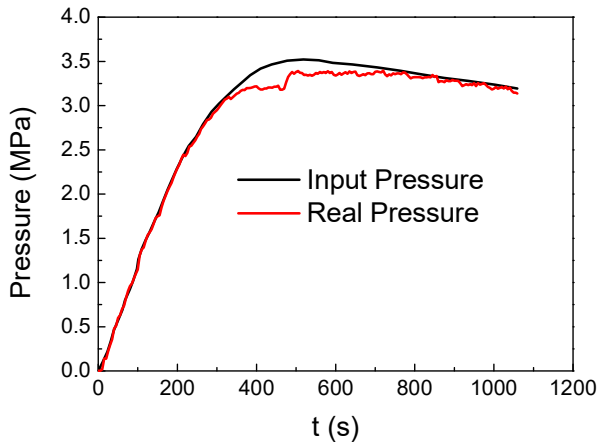
<div align="center">(a)   (b)</div>

Figure V-7 (a) Experimental pressure evolution and (b) the deformation for the axisymmetric shape

With the aid of GOM system, the maximum principal logarithmic strain is measured and the corresponding distribution is shown in Figure V-8 (a). The maximum strain is concentrated on inner edge area. We have to notice that as the painter at some points is got off during the forming experiment, the measured strain is not continuous for the whole studied area. The measured strain in the discontinuous region is not correct. Thus, the strain distribution, as well as the thickness evolution are measured along a line, which avoids the discontinuous area from the center to the board. As shown in Figure V-8 (b, c), the maximum value of the principal logarithmic strain is 0.42 while the thinnest thickness is 1.63 mm, which both are located at 40 mm away from the center point.

<div align="center">(a)</div>
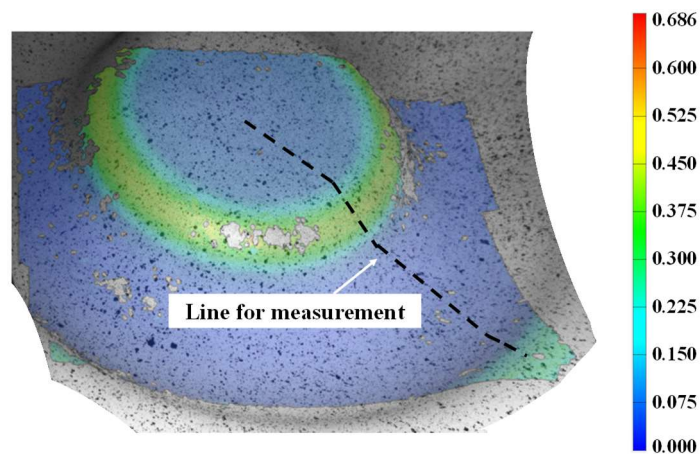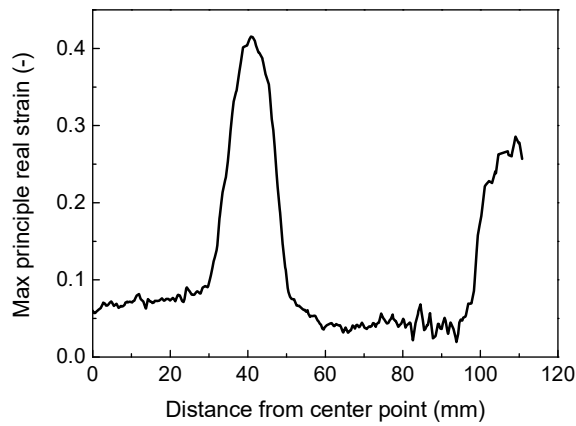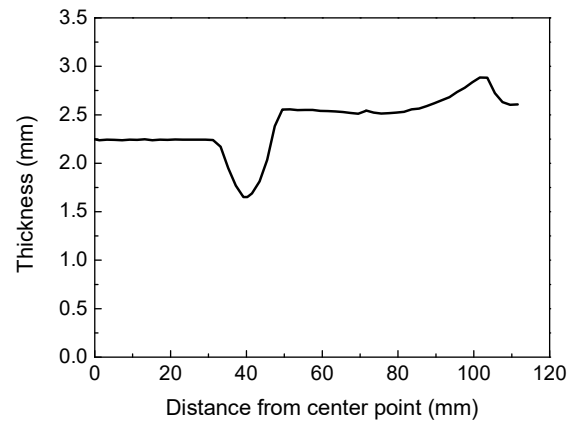
Figure V-8 Experimental results for axisymmetric forming measured by GOM software. (a) Maximum principal real strain field distribution; (b) Maximum principal real strain and (c) Thickness from the center point to the board

V.2.2.2　Cross shape forming

The aim of the cross shape forming is to experimentally study the influence of strain rate strategy on the part quality. Two cross shape forming tests are performed: low constant strain rate forming at $0.0001 \ s^{-1}$ and changed strain rate forming from $0.01 \ s^{-1}$ to $0.0001 \ s^{-1}$.

Low constant strain rate at $0.0001 \ s^{-1}$

Similar to the axisymmetric shape forming, the pressure evolution computed from the numerical simulation is used as an input in the machine, while the real pressure can precisely follow the input pressure (Figure V-9 (a)). The total forming time for low constant strain rate forming is around 15000 s. As the geometry of the cross-shape die is voluntary asymmetric, the strain and the thickness evolution exhibit different values for four corners. The minimum thickness, whose value is 0.99 mm, is located at corner where the fracture happens. As shown in Figure V-9 (b), there exists a crack at one corner for the deformed part.
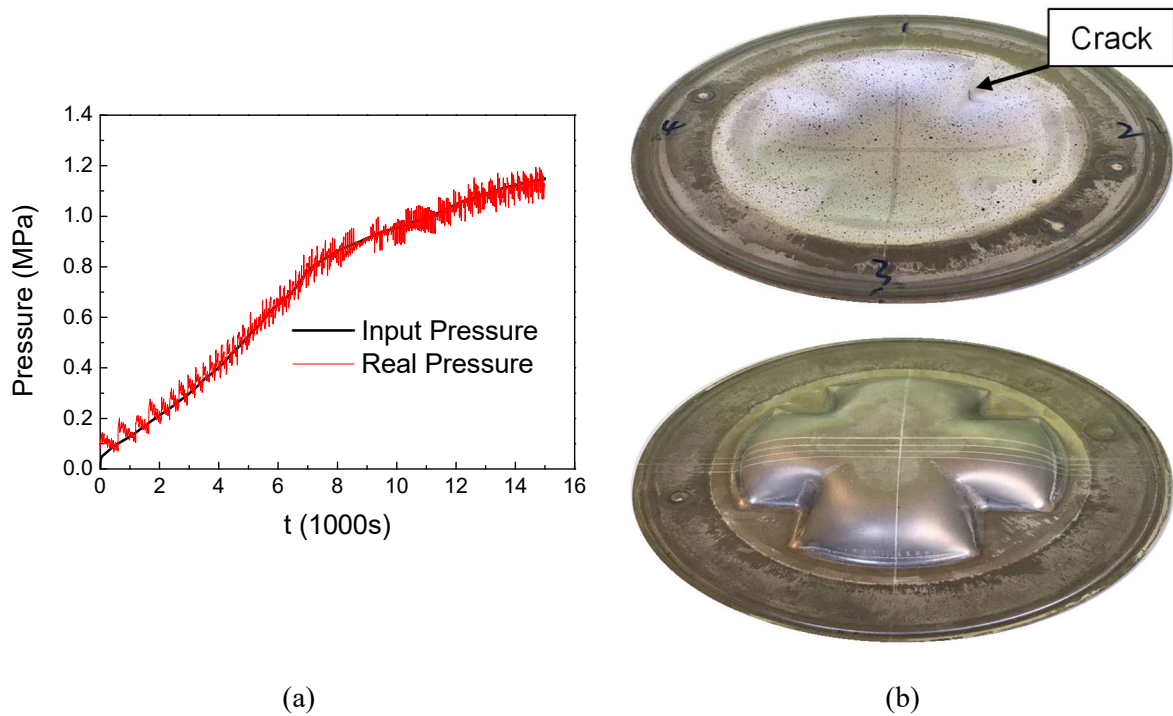
Figure V-9 (a) Experimental pressure evolution and (b) the deformed plate for the cross die deformed at constant low strain rate

The major principal logarithmic strains and thickness evolution in the center part of the deformed specimen are checked by GOM software. Their evolutions are plotted against the position in the bottom area of the deformed part, as shown in Figure V-10. The major principal logarithmic strain is the lowest in the center region and increases progressively when the position is shifted to the board. The thickness has its largest value at the center position. The average values for logarithmic strain and thickness at the bottom part are 0.14 and 2.5 mm, respectively. For the corners areas of the deformed part, the GOM software cannot measure the logarithmic strain due to the peeling of painter during the bulging deformation. In the next section, which talk about comparison between experiment and simulation, the strain distribution will only be investigated in the bottom of deformed part. While for the analysis of other area, only thickness distribution will be discussed.

(a)

(b)

(c)
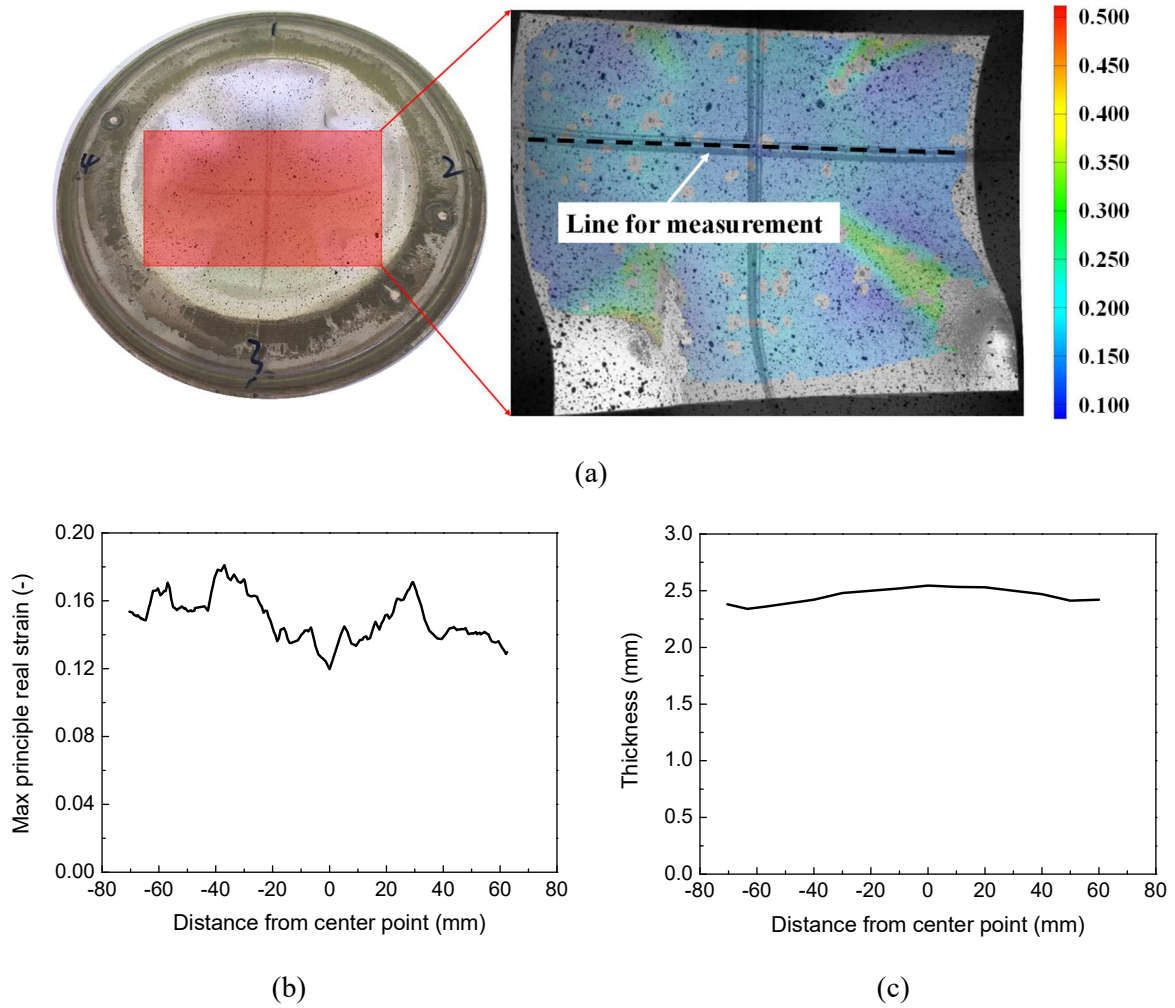
Figure V-10 Experimental results for cross shape forming measured by GOM software. (a) Maximum principal real strain field distribution; (b) maximum principal logarithmic strain and (c) thickness evolution at the bottom of deformed part

Changed strain rate from 0.01 s⁻¹ to 0.0001 s⁻¹

Seen above, there exists a crack when the sheet fulfills the die at constant low strain rate forming for the temperature of 673 K. Having seen the results from the axisymmetric shape forming simulations at different strain rates, the formed part quality between the changed forming strain rate and low constant forming strain rate can be neglected. In this section, the second experiment for the cross shape is carried out to a large deformation without damage, using changed strain rate strategy. The input pressure law is obtained from the numerical simulation, in which the strain rate evolution follows

$$\dot{\bar{\varepsilon}}^P = \begin{cases} = 0.01\,s^{-1} & \bar{\varepsilon}^P < 0.4 \\ = 0.001\,s^{-1} & 0.4 \leq \bar{\varepsilon}^P < 0.9 \\ = 0.0001\,s^{-1} & \bar{\varepsilon}^P \geq 0.9 \end{cases} \qquad (V.8)$$

As shown in Figure V-11 (a), the input pressure suddenly dropped around the forming time of 500 s due to the change of forming strain rate. While real forming pressure cannot change in large scale immediately due to the limitation of the machine. Thus, in the forming time between 500 s and 1000 s,

the real forming pressure is bigger than input pressure. However, the real forming pressure generally follows the input pressure in the whole forming range. The whole forming time is 6000 s. No fracture exists on the deformed flange under these bulging conditions, seen in Figure V-11 (b). By checking the thickness of the whole deformed part, it is found the minimum thickness, whose value is 1.17 mm, is located in the same of corner as the fracture occurs for the low constant strain rate forming. Thus, the strain concentration position is the same for different strain rate forming strategies.

(a)	(b)
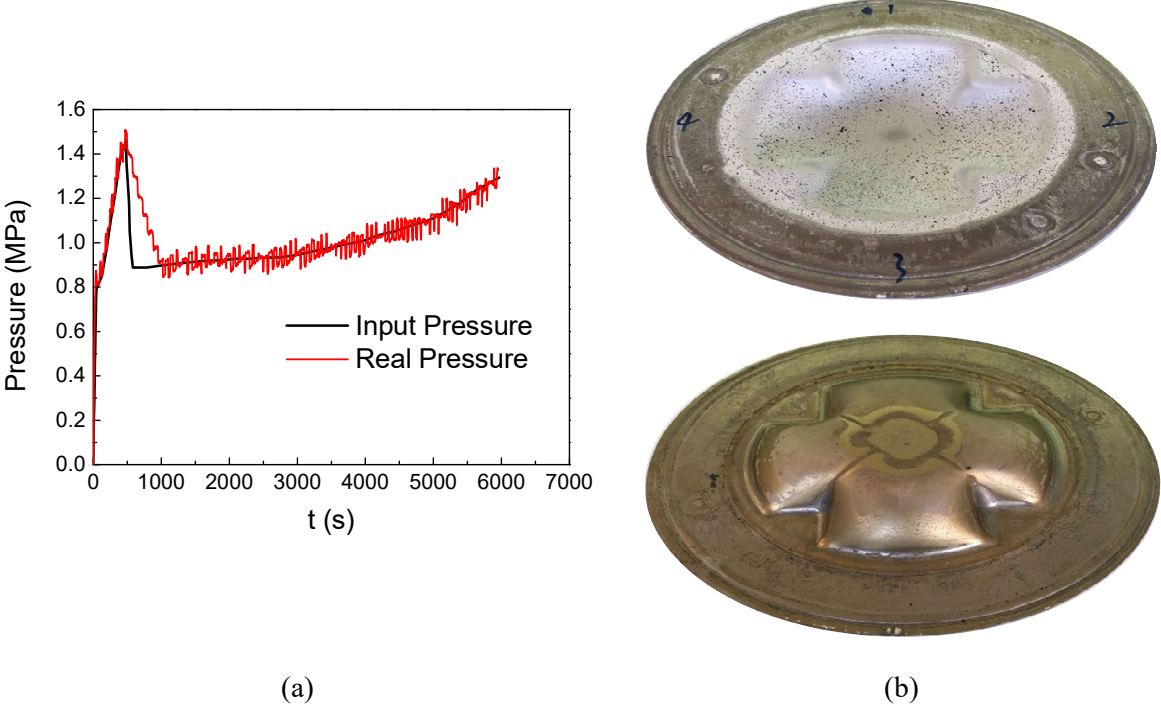
Figure V-11 (a) Experimental pressure evolution and (b) the deformed plate for the cross die deformed at changed strain rate

The strain field and thickness evolution in the middle area of the deformed part are presented in Figure V-12. Same reason as cross shape forming at low constant strain rate, we can only see a part of maximum principal logarithmic strain in the bottom of the deformed specimen. The average value in the checked area is around 0.1, which is lower than the one observed at low constant strain rate.
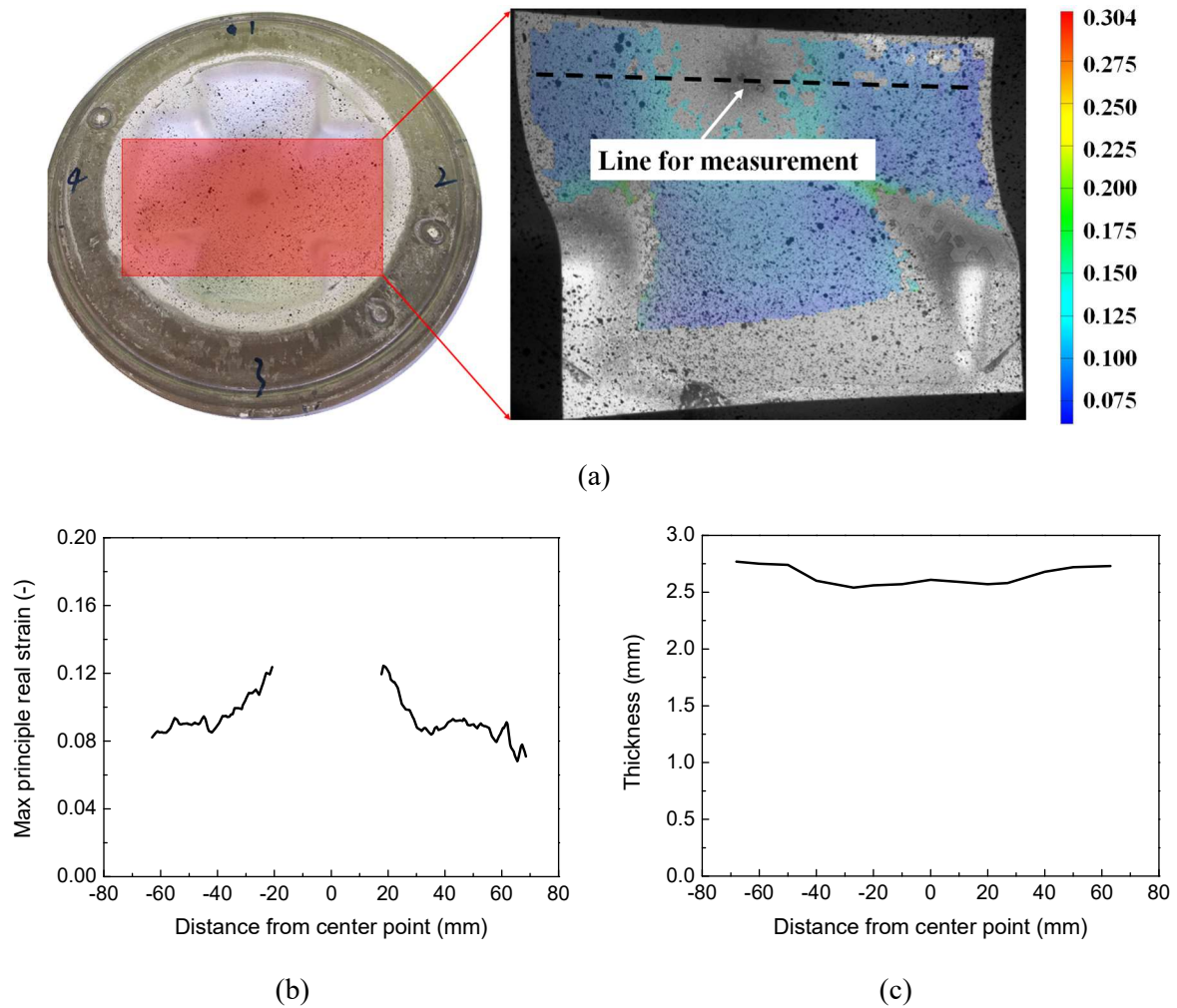
Figure V-12 Experimental results for cross-shape forming measured by GOM software. (a) Maximum principal real strain field distribution; (b) maximum principal logarithmic strain and (c) thickness evolution from the center point to the board

V.3 Comparison between forming experiments and simulations

In this part, the experimental and simulated results for the forming of axisymmetric shape and cross shape are compared. The axisymmetric shape forming is mainly used to verify the predictability of the proposed constitutive law. While the cross-shape forming at low constant strain rate is dedicated to the verification of damage model. The two cross-piece forming tests allow to verify the interest of the changed strain rate strategy which can significantly reduce the forming time without sacrificing the quality of the part.

V.3.1 Axisymmetric shape forming

The real experimental bulging pressure is imposed on the axisymmetric shape forming simulation. The material models and boundary conditions are kept the same. The comparison between the

experiment and simulation regarding to the principal logarithmic strain and the thickness distribution is shown in Figure V-13. For a better comparison, the simulation results obtained from the Hill48 yield criterion for the same deformation displacement are also presented. It is found that the Hill48 yield criterion overestimates the logarithmic strain in the center part and underestimates the value in the most deformed area. For the thickness distribution, the difference between the experiment and numerical simulation from Hill48 is quite significant in the sever deformed zone. While by using the BBC2003 yield criterion, the simulation can generally predict the experimental results both in the logarithmic strain and thickness distribution. The predicted error for the principal logarithmic strain and thickness at the 40 mm distance from center point is 4.3% and 7.9%, respectively. Thus, the BBC2003 yield criterion can be used to describe the constitutive behavior under complex forming conditions.

(a)   (b)
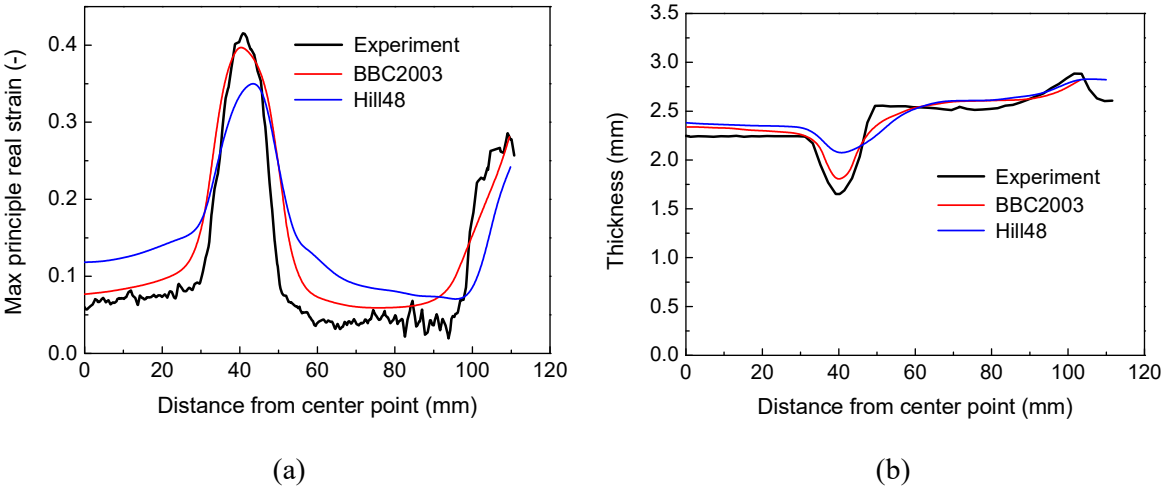
Figure V-13 Comparison between experiment and simulation for axisymmetric shape forming regarding (a) principal logarithmic strain and (b) thickness distribution

V.3.2 Cross shape forming

In this section, two numerical simulations are performed on cross shape die with different strain rate control strategies: low constant strain rate and changed strain rate. The pressure evolutions are the same as in the experimental conditions. The identified composite flow law with BBC2003 yield criterion and the MMC damage criterion are used to describe the material behavior in the simulations. The board of the deformable sheet is fixed as the boundary condition. While the pressure laws input on the flange surface are the real forming pressure evolution. The integration points are considered to fail and are deleted when the damage indicator value in the simulation is greater than 0.99.
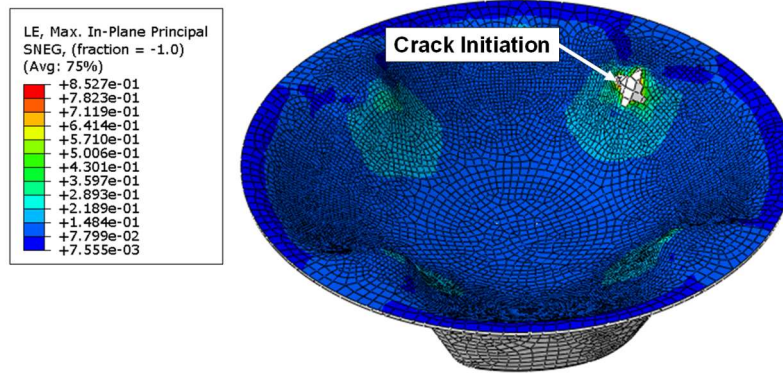
Figure V-14 Numerical cross shape forming at the low constant strain rate

Figure V-14 shows the crack initiation position in the numerical cross shape forming at low constant strain rate, which coincides with the experimental failure locus. Thus, the identified MMC damage model can give, for this forming case, a good failure prediction. While for the cross shape forming using the changed strain rate strategy, the damage indicators for all the integration points are lower than 0.99, showing no failure for these forming conditions. The comparison between the experimental and numerical results, concerning maximum logarithmic strain and thickness evolution, are compared in Figure V-15. The simulated strain and thickness evolution for both two cross-shape forming can predict the corresponding experimental results precisely, indicating the constitutive model can also predict the material behavior for cross-shape forming at different strain rate strategies.

(a)   (b)
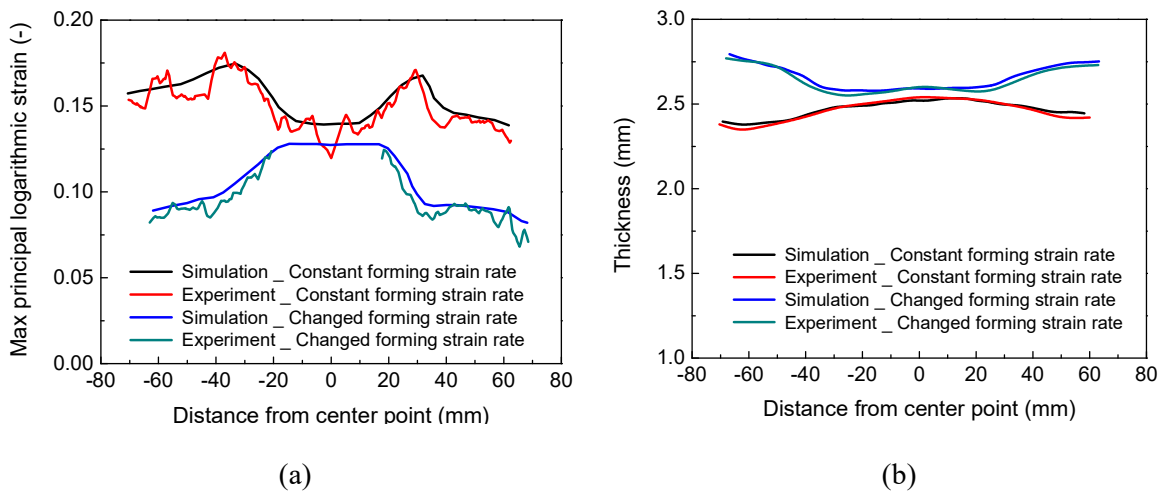
Figure V-15 Comparison for cross shape forming between experiment and simulation : (a) maximum principal logarithmic strain and (b) thickness

As discussed in Chapter III, the forming limit of AA5383 alloy at high temperatures increase with the decrease of forming strain rate. In the cross forming experiment, though the forming strain rate is low, namely at 0.0001 s^{-1}, there exists a crack when the flange fulfills the die. This is due to the inherent ductility limitation of the material. Improving the ductility of material by sever plastic deformation or performing the forming at higher temperature will be discussed in the future.

Different from the low constant forming strain rate, the cross-shape test is also performed at changed forming strain rate to bulge the deformed flange without failure. Seen in Figure V-15, the cross deformed part from the changed strain rate strategy exhibits less strain level compared to the part deformed from the low constant strain rate.

The simulations are performed on the cross-shape die to obtain the same extend of deformation, by using two different strain rate strategies control. Shown in Figure V-16, the total forming time for the cross-shape forming with the changed strain rate strategy is about 54% less than the one with the low constant forming strain rate. Thus, changed strain rate forming strategy can be used to reduce the forming time without sacrificing the part quality. In the future, we can propose some methods to increase the material hot deformation ductility in order to fulfill the sheet into the cross-shape die by using the changed strain rate control strategy without failure.
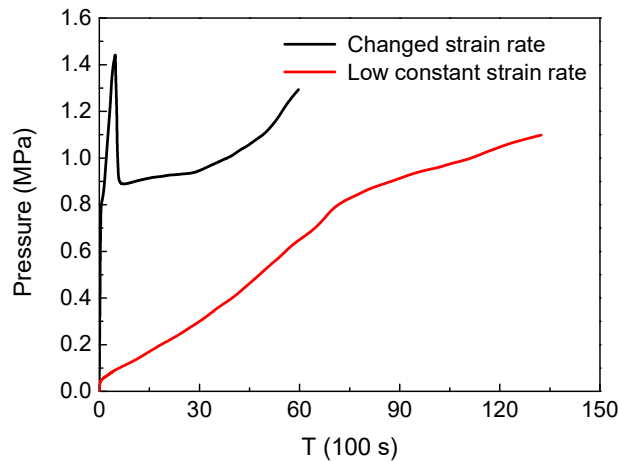
Figure V-16 Pressure evolution for cross-shape forming by using changed strain rate and low constant strain rate strategies

V.4 Summary

In this chapter, two types of forming simulations, axisymmetric shape and cross shape, are carried out by using the identified material models. The Subroutine UEXTERNALDB, DLOAD and URDFIL are chosen to perform loading cycle to control the forming strain rate. After comparing three different pressure control strategies, it is found the new developed strategy can better follow the aimed strain rate. Thus, this method is used for all the forming simulations. The integration point number selection is also an important issue. This pressure control strategy can avoid strain rate concentration effects, for complex shapes forming. The classic one maximum strain rate selection would lead to a quite low forming pressure. It is found that 2% of integration point average for axisymmetric shape bulging while 5% of integration point average for cross shape forming can have a quite good result. From the numerical point, the changed strain rate strategy can reduce the forming time while keep the part quality when compared to the low constant strain rate approach.

Three forming experiments are carried out at the temperature of 673 K: an axisymmetric shape forming test at constant equivalent plastic strain rate of 0.001 s^{-1}; a cross shape forming test at a constant equivalent plastic strain rate of 0.0001 s^{-1} and a changed strain rate, respectively. The axisymmetric shape forming is performed to verify the identified material models. BBC2003 yield criterion exhibits a better prediction for the principal logarithmic stress and the thickness distribution compared to Hill48 yield criterion. For the two cross shape tests, the simulated principal logarithmic strain can track the experimental results in the bottom area of deformed sheet. The fracture initiation position for the low constant equivalent plastic strain rate of 0.0001 s^{-1} is quite well predicted by the numerical simulation. In the case of cross-shape forming, from both experimental and simulation results, the changed strain rate strategy can reduce the forming time significantly without sacrificing the part quality.

Due to the inherent limitation of high temperature ductility, the sheet cannot fulfill the die without damage for our testing conditions. Two method in the future can solve this problem: enhance the forming temperatures to have higher ductility or use some techniques (like sever plastic deformation) to improve the initial mechanical properties.

Conclusion and perspectives

Conclusion

This section describes the conclusions of this research. The main objective of the work is to reduce the forming time without sacrificing part quality. The major stages to achieve this goal are distinguished:

Material characterization: The present study focuses on the AA5383 aluminum-magnesium alloy. This alloy has been microstructurally and mechanically characterized. For the as-received state, because of the rolling process, the microstructure is composed of elongated grains along the rolling direction. The crystallographic texture is quite pronounced, with an important brass component. In the present work, the AA5383 is heat-treated at 623 K for 5 min prior to any deformation to increase the ductility. As a result of this treatment, grains are equiaxed and the brass component of the crystallographic texture is largely attenuated. The mechanical characterization of AA5383 alloy has been carried out in wide range of temperature, strain rate and stress state. The main conclusions of these tests follow:

- First, some uniaxial and biaxial tests have been performed to evaluate the <u>flow behavior</u> and <u>yield criterion</u>. As expected, the flow stress is largely influenced by strain rate and temperature. The material exhibits a hardening behavior at low strain rates while slight softening occurs for high strain rates. The softening phenomenon is related to dynamic recrystallization. Also, uniaxial tension tests for different angles with respect to rolling direction have been employed to study the anisotropic properties at 673 K and 0.001 s^{-1}. The yield stress along the rolling direction is a little higher than the ones for the 45° and 90° directions.

- Second, to characterize the <u>fracture behavior</u> under hot deformation, uniaxial tension speicmen, four notched tension specimens, a shear specimen, together with a free bulging, are used to study the influence of stress state, temperature and strain rate on the forming limit. For a fixed deformation temperature and strain rate, the fracture displacement decreases with the decrease of radius value for notched specimens. Also, for a fixed stress state, the maximum displacement increases with an increasing temperature and a decreasing strain rate. The corresponding results allow determining the parameters of ductile fracture.

Model identification and implementation: material models, including a constitutive model and a damage model, are proposed to describe the thermo-mechanical behavior of AA5383 alloy. The main conclusions are summarized:

- <u>Flow behavior</u>. To describe the flow behavior, the strain-compensated Arrhenius type model and the composite model are proposed. The composite model is selected as the flow model due to its easier implementation and lower relative error.

- <u>Yield criterion</u>. Based on the experimental results obtained from deformation condition of 673 K and 0.001 s^{-1}, BBC2003 yield criterion is proposed and identified. Anisotropic Hill48 yield

criterion is used as a reference. It is shows that BBC2003 yield criterion can predict the experimental Lankford coefficients and yield stresses accurately, while Hill48 yield criterion exhibits a higher yield stresses in the 45° and 90° directions and a lower biaxial yield stress prediction. The models are implemented into user subroutine UMAT by a semi-implicit integration scheme.

- Damage behavior. The MMC damage model, which includes the influence of temperature and strain rate, is proposed. The parameters are identified by using genetic optimization method to minimize the root mean squared error directly. The numerical simulations, which have been used for identifying the equivalent fracture strains, are performed again by including the damage influence. It is seen that the MMC damage model can accurately predict the fracture displacement for all the studied conditions.

Numerical simulation and experimental forming: two types of forming simulations, axisymmetric shape and cross shape, are carried out by using the identified material models. The subroutine UEXTERNALDB, DLOAD and URDFIL are chosen to perform loading cycle to control the forming strain rate.

- The new proposed pressure control strategy allows to follow the aimed strain rate. For the integration point number selection, 2% of integration point average for axisymmetric shape bulging while 5% of integration point average for cross shape forming can have a quite good result.
- For axisymmetric shape test, BBC2003 yield criterion exhibits a better prediction for the principal logarithmic stress and the thickness distribution compared to Hill48 yield criterion.
- The simulated principal logarithmic strain can track the experimental results in the bottom area of deformed sheet. The fracture initiation position of cross-shape forming at the low constant equivalent plastic strain rate of 0.0001 s^{-1} is quite well predicted by the numerical simulation.
- In the case of cross-shape forming, from both experimental and simulation results, the changed strain rate strategy can reduce the forming time significantly without sacrificing the part quality.

Perspectives

The present dissertation has proposed the material models to accurately describe the hot deformation behaviors of material. However, some works could still be done in the future regarding to perfect our existing results and to try other techniques.

For perfecting the existing results:

- In the numerical simulation part, we have used two assumptions to predict material hot deformation behavior. In the future work, the Lankford coefficients at different temperatures and strain rates could be measured to verify if those values are appropriate to be regarded as a

constant. While fracture strains of more than one type of specimen can be checked to verify the fracture locus.

- To predict the damage behavior, some couple damage models can also be proposed and compared with the results obtained by the MMC criterion

- In the experimental forming part, only the influence of strain rate on final part quality has been exclusively studied. While testing temperature is also an important factor for sheet metal forming. Thus, the temperature influence on the damage localization and initiation would be investigated in our studied temperature range.

- GOM software can be used in the Gleeble machine to measure the evolution of strain field during the hot temperature deformation directly. In our study, the fracture strains have been obtained by using inverse method. The experimental failure strains can be regarded as a method to compare and verify the simulated results. Also, the whole surface strain field of deformed parts in the forming tests could be measured by using the GOM software and be compared with corresponding numerical results.

For trying other techniques:

- Other forming chaining techniques would be tried to reduce the total forming time. In our study, all the complex forming processes have been realized by gas forming. In the future, the pre-deform step could also be tried by hot stamping.

- Some techniques, like constrained groove pressing, could be used to improve its initial mechanical properties. Seen in the cross shape forming, no matter the strain rate, there exists a failure when the sheet full contacts with the die. Thus, by increasing the initial ductile properties, the sheet can fulfill the die without damage with the same processing conditions.

- The deformed specimen obtained from the gas forming in our research could be compared to the one obtained from the incremental forming. It would be interesting to compare the part quality of the parts obtained from different forming techniques.

Appendix

Appendix A. Flow rule associated with BBC2003 yield criterion

The flow direction $\boldsymbol{n}$ is given by

$$\boldsymbol{n} = \frac{\partial \Phi}{\partial \boldsymbol{\sigma}} = \frac{\partial \bar{\sigma}(\sigma_{ij})}{\partial \boldsymbol{\sigma}} = \frac{\partial \bar{\sigma}}{\partial \sigma_{11}} e_1 \otimes e_1 + \frac{\partial \bar{\sigma}}{\partial \sigma_{22}} e_2 \otimes e_2 + \frac{\partial \bar{\sigma}}{\partial \sigma_{12}} e_1 \otimes e_2 + \frac{\partial \bar{\sigma}}{\partial \sigma_{21}} e_1 \otimes e_2 \qquad (A.1)$$

The following system of equations obtained

$$\begin{cases} \dfrac{\partial \bar{\sigma}}{\partial \sigma_{11}} = \dfrac{\partial \bar{\sigma}}{\partial \Gamma} \dfrac{\partial \Gamma}{\partial \sigma_{11}} + \dfrac{\partial \bar{\sigma}}{\partial \Psi} \dfrac{\partial \Psi}{\partial \sigma_{11}} + \dfrac{\partial \bar{\sigma}}{\partial \Lambda} \dfrac{\partial \Lambda}{\partial \sigma_{11}} \\[2mm] \dfrac{\partial \bar{\sigma}}{\partial \sigma_{22}} = \dfrac{\partial \bar{\sigma}}{\partial \Gamma} \dfrac{\partial \Gamma}{\partial \sigma_{22}} + \dfrac{\partial \bar{\sigma}}{\partial \Psi} \dfrac{\partial \Psi}{\partial \sigma_{22}} + \dfrac{\partial \bar{\sigma}}{\partial \Lambda} \dfrac{\partial \Lambda}{\partial \sigma_{22}} \\[2mm] \dfrac{\partial \bar{\sigma}}{\partial \sigma_{12}} = \dfrac{\partial \bar{\sigma}}{\partial \Gamma} \dfrac{\partial \Gamma}{\partial \sigma_{12}} + \dfrac{\partial \bar{\sigma}}{\partial \Psi} \dfrac{\partial \Psi}{\partial \sigma_{12}} + \dfrac{\partial \bar{\sigma}}{\partial \Lambda} \dfrac{\partial \Lambda}{\partial \sigma_{12}} \\[2mm] \dfrac{\partial \bar{\sigma}}{\partial \sigma_{21}} = \dfrac{\partial \bar{\sigma}}{\partial \Gamma} \dfrac{\partial \Gamma}{\partial \sigma_{21}} + \dfrac{\partial \bar{\sigma}}{\partial \Psi} \dfrac{\partial \Psi}{\partial \sigma_{21}} + \dfrac{\partial \bar{\sigma}}{\partial \Lambda} \dfrac{\partial \Lambda}{\partial \sigma_{21}} \end{cases} \qquad (A.2)$$

where

$$\frac{\partial \bar{\sigma}}{\partial \Gamma} = \frac{a}{\bar{\sigma}^{2k-1}} [(\Gamma + \Psi)^{2k-1} + (\Gamma - \Psi)^{2k-1}]$$

$$\frac{\partial \bar{\sigma}}{\partial \Psi} = \frac{a}{\bar{\sigma}^{2k-1}} [(\Gamma + \Psi)^{2k-1} - (\Gamma - \Psi)^{2k-1}] \qquad (A.3)$$

$$\frac{\partial \bar{\sigma}}{\partial \Lambda} == \frac{2(1-a)}{\bar{\sigma}^{2k-1}} [(2\Lambda)^{2k-1}]$$

And other terms

$$\frac{\partial \Gamma}{\partial \sigma_{11}} = \frac{1}{2}; \quad \frac{\partial \Gamma}{\partial \sigma_{22}} = \frac{M}{2}; \quad \frac{\partial \Gamma}{\partial \sigma_{12}} = \frac{\partial \Gamma}{\partial \sigma_{21}} = 0 \qquad (A.4)$$

$$\frac{\partial \Psi}{\partial \sigma_{11}} = \frac{\frac{1}{4}(N\sigma_{11} - P\sigma_{22})N}{\sqrt{\frac{1}{4}(N\sigma_{11} - P\sigma_{22})^2 + Q^2 \sigma_{12}\sigma_{21}}}$$

$$\frac{\partial \Psi}{\partial \sigma_{22}} = \frac{\frac{1}{4}(N\sigma_{11} - P\sigma_{22})(-P)}{\sqrt{\frac{1}{4}(N\sigma_{11} - P\sigma_{22})^2 + Q^2 \sigma_{12}\sigma_{21}}} \qquad (A.5)$$

$$\frac{\partial \Psi}{\partial \sigma_{12}} = \frac{Q^2 \sigma_{21}}{2 \cdot \sqrt{\frac{1}{4}(N\sigma_{11} - P\sigma_{22})^2 + Q^2 \sigma_{12}\sigma_{21}}}$$

$$\frac{\partial \Psi}{\partial \sigma_{21}} = \frac{Q^2 \sigma_{12}}{2 \cdot \sqrt{\frac{1}{4}(N\sigma_{11} - P\sigma_{22})^2 + Q^2 \sigma_{12}\sigma_{21}}}$$

$$\frac{\partial \Lambda}{\partial \sigma_{11}} = \frac{\frac{1}{4}(R\sigma_{11} - S\sigma_{22})R}{\sqrt{\frac{1}{4}(R\sigma_{11} - S\sigma_{22})^2 + T^2\sigma_{12}\sigma_{21}}}$$

$$\frac{\partial \Lambda}{\partial \sigma_{22}} = \frac{\frac{1}{4}(R\sigma_{11} - S\sigma_{22})(-S)}{\sqrt{\frac{1}{4}(R\sigma_{11} - S\sigma_{22})^2 + T^2\sigma_{12}\sigma_{21}}} \qquad (A.6)$$

$$\frac{\partial \Lambda}{\partial \sigma_{12}} = \frac{T^2\sigma_{21}}{2 \cdot \sqrt{\frac{1}{4}(R\sigma_{11} - S\sigma_{22})^2 + T^2\sigma_{12}\sigma_{21}}}$$

$$\frac{\partial \Lambda}{\partial \sigma_{21}} = \frac{T^2\sigma_{12}}{2 \cdot \sqrt{\frac{1}{4}(R\sigma_{11} - S\sigma_{22})^2 + T^2\sigma_{12}\sigma_{21}}}$$

References

[1] Heinz, A., et al., Recent development in aluminium alloys for aerospace applications. *Materials Science and Engineering: A*, 2000. 280(1): p. 102-107.

[2] Xing, H.L., et al., Recent development in the mechanics of superplasticity and its applications. *Journal of Materials Processing Technology*, 2004. 151(1): p. 196-202.

[3] Sotoudeh, K. and P. Bate, Diffusion creep and superplasticity in aluminium alloys. *Acta Materialia*, 2010. 58(6): p. 1909-1920.

[4] Grimes, R., 11 - Superplastic forming of aluminium alloys, in *Superplastic Forming of Advanced Metallic Materials*, G. Giuliano, Editor. 2011, Woodhead Publishing. p. 247-271.

[5] Friedman, P. and W. Copple, Superplastic response in Al-Mg sheet alloys. *Journal of materials engineering and performance*, 2004. 13(3): p. 335-347.

[6] Chatterjee, R. and J. Mukhopadhyay, A Review of Super plastic forming. *Materials Today: Proceedings*, 2018. 5(2, Part 1): p. 4452-4459.

[7] Bonet, J., et al., Simulating superplastic forming. *Computer Methods in Applied Mechanics and Engineering*, 2006. 195(48): p. 6580-6603.

[8] Fong, K.S., et al., Enabling wider use of Magnesium Alloys for lightweight applications by improving the formability by Groove Pressing. *Procedia CIRP*, 2015. 26: p. 449-454.

[9] Luo, Y., et al., Development of an advanced superplastic forming process utilizing a mechanical pre-forming operation. *International Journal of Machine Tools and Manufacture*, 2008. 48(12): p. 1509-1518.

[10] Liu, J., et al., Superplastic-like forming of non-superplastic AA5083 combined with mechanical pre-forming. *The International Journal of Advanced Manufacturing Technology*, 2011. 52(1): p. 123-129.

[11] Jeswiet, J., et al., Asymmetric Single Point Incremental Forming of Sheet Metal. *CIRP Annals*, 2005. 54(2): p. 88-114.

[12] Miller, W.S., et al., Recent development in aluminium alloys for the automotive industry. *Materials Science and Engineering: A*, 2000. 280(1): p. 37-49.

[13] Wanhill, R.J.H., Chapter 15 - Aerospace Applications of Aluminum–Lithium Alloys, in *Aluminum-lithium Alloys*. 2014, Butterworth-Heinemann: Boston. p. 503-535.

[14] Bariani, P.F., et al., Hot stamping of AA5083 aluminium alloy sheets. *CIRP Annals*, 2013. 62(1): p. 251-254.

[15] Mahabunphachai, S. and M. Koç, Investigations on forming of aluminum 5052 and 6061 sheet alloys at warm temperatures. *Materials & Design (1980-2015)*, 2010. 31(5): p. 2422-2434.

[16]   Abedrabbo, N., F. Pourboghrat, and J. Carsley, Forming of aluminum alloys at elevated temperatures – Part 1: Material characterization. *International Journal of Plasticity*, 2006. 22(2): p. 314-341.

[17]   Kim, H.S. and M. Koç, Numerical investigations on springback characteristics of aluminum sheet metal alloys in warm forming conditions. *Journal of Materials Processing Technology*, 2008. 204(1): p. 370-383.

[18]   Takuda, H., et al., Finite element simulation of warm deep drawing of aluminium alloy sheet when accounting for heat conduction. *Journal of Materials Processing Technology*, 2002. 120(1): p. 412-418.

[19]   Harrison, N.R., P.A. Friedman, and J. Pan, Warm forming die design, Part III: Design and validation of a warm forming die. *Journal of Manufacturing Processes*, 2015. 20: p. 356-366.

[20]   Shi, Z., et al. An investigation, using standard experimental techniques, to determine FLCs at elevated temperature for aluminium alloys. in: *Proceedings of the 3rd International Conference on New Forming Technology*. China. 2012.

[21]   Lin, J., R.P. Garrett, and A.D. Foster. Process for forming metal alloy sheet components. in: *T.u.o. Birmingham (Ed.)*. United Kingdom. 2008.

[22]   Maeno, T., K.-i. Mori, and R. Yachi, Hot stamping of high-strength aluminium alloy aircraft parts using quick heating. *CIRP Annals*, 2017. 66(1): p. 269-272.

[23]   Zhang, S.H. and J. Danckert, Development of hydro-mechanical deep drawing. *Journal of Materials Processing Technology*, 1998. 83(1): p. 14-25.

[24]   Lang, L., et al., Pressure rate controlled unified constitutive equations based on microstructure evolution for warm hydroforming. *Journal of Alloys and Compounds*, 2013. 574: p. 41-48.

[25]   Palumbo, G., et al., Warm HydroForming of the heat treatable aluminium alloy AC170PX. *Journal of Manufacturing Processes*, 2015. 20: p. 24-32.

[26]   Palumbo, G., et al., Evaluation of the optimal working conditions for the warm sheet HydroForming taking into account the yielding condition. *Materials & Design*, 2016. 91: p. 411-423.

[27]   Matsubara, S., Incremental backward bulge forming of a sheet metal with a hemispherical head tool-a study of a numerical control forming system II. *Journal of the Japan society for technology of plasticity*, 1994. 35(406): p. 1311-1316.

[28]   Jackson, K. and J. Allwood, The mechanics of incremental sheet forming. *Journal of Materials Processing Technology*, 2009. 209(3): p. 1158-1174.

[29]   Ji, Y.H. and J.J. Park, Formability of magnesium AZ31 sheet in the incremental forming at warm temperature. *Journal of Materials Processing Technology*, 2008. 201(1): p. 354-358.

[30]   Duflou, J.R., et al., Laser Assisted Incremental Forming: Formability and Accuracy Improvement. *CIRP Annals*, 2007. 56(1): p. 273-276.

[31] Fan, G., et al., Electric hot incremental forming: A novel technique. *International Journal of Machine Tools and Manufacture*, 2008. 48(15): p. 1688-1692.

[32] Chokshi, A.H., A.K. Mukherjee, and T.G. Langdon, Superplasticity in advanced materials. *Materials Science and Engineering: R: Reports*, 1993. 10(6): p. 237-274.

[33] Chandra, N., Constitutive behavior of superplastic materials. *International Journal of Non-Linear Mechanics*, 2002. 37(3): p. 461-484.

[34] Barnes, A., Superplastic forming 40 years and still growing. *Journal of Materials Engineering and performance*, 2007. 16(4): p. 440-454.

[35] Boude, S. Maîtrise du procédé de formage superplastique et réalisation d'une installation pilote. *PhD thesis*. Université de Nantes. 1994.

[36] Hwang, Y.M. and H.S. Lay, Study on superplastic blow-forming in a rectangular closed-die. *Journal of Materials Processing Technology*, 2003. 140(1): p. 426-431.

[37] Kawasaki, M. and T.G. Langdon, achieving superplasticity in metals processed by high-pressure torsion. *Journal of materials science*, 2014. 49(19): p. 6487-6496.

[38] Shin, D.H., et al., Constrained groove pressing and its application to grain refinement of aluminum. *Materials Science and Engineering: A*, 2002. 328(1): p. 98-103.

[39] Krishnaiah, A., U. Chakkingal, and P. Venugopal, Applicability of the groove pressing technique for grain refinement in commercial purity copper. *Materials Science and Engineering: A*, 2005. 410-411: p. 337-340.

[40] Khodabakhshi, F., M. Kazeminezhad, and A.H. Kokabi, Constrained groove pressing of low carbon steel: Nano-structure and mechanical properties. *Materials Science and Engineering: A*, 2010. 527(16): p. 4043-4049.

[41] Furushima, T. and K. Manabe, 14 - Superplastic micro-tubes fabricated by dieless drawing processes A2 - Giuliano, Gillo, in *Superplastic Forming of Advanced Metallic Materials*. 2011, Woodhead Publishing. p. 327-360.

[42] Krajewski, P.E. and J.G. Schroth, 12 - Quick Plastic Forming of aluminium alloys A2 - Giuliano, Gillo, in *Superplastic Forming of Advanced Metallic Materials*. 2011, Woodhead Publishing. p. 272-303.

[43] Krajewski, P.E. and J.G. Schroth, Overview of Quick Plastic Forming Technology. *Materials Science Forum*, 2007. 551-552: p. 3-12.

[44] Friedman, P.A., *Method and apparatus for superplastic forming*. 2003, Google Patents.

[45] Liu, J., et al., Superplastic-like forming of Ti-6Al-4V alloy. *The International Journal of Advanced Manufacturing Technology*, 2013. 69(5-8): p. 1097-1104.

[46] Wu, H.-Y., et al., Modified male die rapid gas blow forming of fine-grained Mg alloy AZ31B thin sheet. *The International Journal of Advanced Manufacturing Technology*, 2015. 80(5-8): p. 1241-1252.

[47] Liu, J., et al., Process optimization and microstructural development during superplastic-like forming of AA5083. *The International Journal of Advanced Manufacturing Technology*, 2013. 69(9-12): p. 2415-2422.

[48] Boissiere, R., et al. Quick-plastic forming: Similarities and differences with super-plastic forming. in: *EuroSPF08*. France. 2008.

[49] Johnson, G.R. and W.H. Cook. A constitutive model and data for materials subjected to large strains, high strain rates, and high temperatures. in: *Proceedings of Seventh International Symposium on Ballistics*. Netherlands. 1983.

[50] Lin, Y.C., X.-M. Chen, and G. Liu, A modified Johnson–Cook model for tensile behaviors of typical high-strength alloy steel. *Materials Science and Engineering: A*, 2010. 527(26): p. 6980-6986.

[51] Chen, L., G. Zhao, and J. Yu, Hot deformation behavior and constitutive modeling of homogenized 6026 aluminum alloy. *Materials & Design*, 2015. 74: p. 25-35.

[52] Hou, Q.Y. and J.T. Wang, A modified Johnson–Cook constitutive model for Mg–Gd–Y alloy extended to a wide range of temperatures. *Computational Materials Science*, 2010. 50(1): p. 147-152.

[53] Zhang, H., W. Wen, and H. Cui, Behaviors of IC10 alloy over a wide range of strain rates and temperatures: Experiments and modeling. *Materials Science and Engineering: A*, 2009. 504(1-2): p. 99-103.

[54] Lin, Y.C. and X.-M. Chen, A combined Johnson–Cook and Zerilli–Armstrong model for hot compressed typical high-strength alloy steel. *Computational Materials Science*, 2010. 49(3): p. 628-633.

[55] Lin, Y.C. and X.-M. Chen, A critical review of experimental results and constitutive descriptions for metals and alloys in hot working. *Materials & Design*, 2011. 32(4): p. 1733-1759.

[56] Zener, C. and J.H. Hollomon, Effect of strain rate upon plastic flow of steel. *Journal of Applied physics*, 1944. 15(1): p. 22-32.

[57] Li, J., et al., Comparative investigation on the modified Zerilli–Armstrong model and Arrhenius-type model to predict the elevated-temperature flow behaviour of 7050 aluminium alloy. *Computational Materials Science*, 2013. 71: p. 56-65.

[58] Ji, G., et al., Comparative study of phenomenological constitutive equations for an as-rolled M50NiL steel during hot deformation. *Journal of Alloys and Compounds*, 2017. 695(Supplement C): p. 2389-2399.

[59] Ashtiani, H.R.R. and P. Shahsavari, A comparative study on the phenomenological and artificial neural network models to predict hot deformation behavior of AlCuMgPb alloy. *Journal of Alloys and Compounds*, 2016. 687: p. 263-273.

[60] Rezaei Ashtiani, H.R., M.H. Parsa, and H. Bisadi, Constitutive equations for elevated temperature flow behavior of commercial purity aluminum. *Materials Science and Engineering: A*, 2012. 545: p. 61-67.

[61] Cai, Z., F. Chen, and J. Guo, Constitutive model for elevated temperature flow stress of AZ41M magnesium alloy considering the compensation of strain. *Journal of Alloys and Compounds*, 2015. 648: p. 215-222.

[62] Li, H.Y., et al., Constitutive modeling for hot deformation behavior of ZA27 alloy. *Journal of Materials Science*, 2012. 47(14): p. 5411-5418.

[63] Wu, H.-Y., et al., Hot deformation characteristics and strain-dependent constitutive analysis of Inconel 600 superalloy. *Journal of Materials Science*, 2012. 47(9): p. 3971-3981.

[64] Wang, Y., et al., Modeling and application of constitutive model considering the compensation of strain during hot deformation. *Journal of Alloys and Compounds*, 2016. 681: p. 455-470.

[65] Ashtiani, H.R.R. and P. Shahsavari, Strain-dependent constitutive equations to predict high temperature flow behavior of AA2030 aluminum alloy. *Mechanics of Materials*, 2016. 100: p. 209-218.

[66] Lin, Y.C., M.-S. Chen, and J. Zhong, Constitutive modeling for elevated temperature flow behavior of 42CrMo steel. *Computational Materials Science*, 2008. 42(3): p. 470-477.

[67] Mandal, S., et al., Constitutive equations to predict high temperature flow stress in a Ti-modified austenitic stainless steel. *Materials Science and Engineering: A*, 2009. 500(1-2): p. 114-121.

[68] Sung, J.H., J.H. Kim, and R.H. Wagoner, A plastic constitutive equation incorporating strain, strain-rate, and temperature. *International Journal of Plasticity*, 2010. 26(12): p. 1746-1771.

[69] Zerilli, F.J. and R.W. Armstrong, Dislocation‐mechanics‐based constitutive relations for material dynamics calculations. *Journal of Applied Physics*, 1987. 61(5): p. 1816-1825.

[70] Lin, Y.C., M.-S. Chen, and J. Zhong, Prediction of 42CrMo steel flow stress at high temperature and strain rate. *Mechanics Research Communications*, 2008. 35(3): p. 142-150.

[71] Voyiadjis, G.Z. and F.H. Abed, Microstructural based models for bcc and fcc metals with temperature and strain rate dependency. *Mechanics of Materials*, 2005. 37(2): p. 355-378.

[72] Wang, S., et al., Physically based constitutive analysis and microstructural evolution of AA7050 aluminum alloy during hot compression. *Materials & Design*, 2016. 107: p. 277-289.

[73] Vilamosa, V., et al., A physically-based constitutive model applied to AA6082 aluminium alloy at large strains, high strain rates and elevated temperatures. *Materials & Design*, 2016. 103: p. 391-405.

[74] Lin, Y.C., et al., A physically-based constitutive model for a typical nickel-based superalloy. *Computational Materials Science*, 2014. 83: p. 282-289.

[75] Lin, J., A set of unified constitutive equations for modelling microstructure evolution in hot deformation. *Journal of Materials Processing Technology*, 2003. 143-144: p. 281-285.

[76]   Zhang, H., et al., A modified Zerilli–Armstrong model for alloy IC10 over a wide range of temperatures and strain rates. *Materials Science and Engineering: A*, 2009. 527(1-2): p. 328-333.

[77]   Gao, C.Y. and L.C. Zhang, A constitutive model for dynamic plasticity of FCC metals. *Materials Science and Engineering: A*, 2010. 527(13-14): p. 3138-3143.

[78]   Abed, F.H. and G.Z. Voyiadjis, A consistent modified Zerilli-Armstrong flow stress model for BCC and FCC metals for elevated temperatures. *Acta Mechanica*, 2005. 175(1-4): p. 1-18.

[79]   Lee, W.-S. and C.-Y. Liu, The effects of temperature and strain rate on the dynamic flow behaviour of different steels. *Materials Science and Engineering: A*, 2006. 426(1-2): p. 101-113.

[80]   Özel, T. and Y. Karpat, Identification of Constitutive Material Model Parameters for High-Strain Rate Metal Cutting Conditions Using Evolutionary Computational Algorithms. *Materials and Manufacturing Processes*, 2007. 22(5): p. 659-667.

[81]   Samantaray, D., et al., A thermo-viscoplastic constitutive model to predict elevated-temperature flow behaviour in a titanium-modified austenitic stainless steel. *Materials Science and Engineering: A*, 2009. 526(1): p. 1-6.

[82]   He, A., et al., A modified Zerilli–Armstrong constitutive model to predict hot deformation behavior of 20CrMo alloy steel. *Materials & Design (1980-2015)*, 2014. 56: p. 122-127.

[83]   Zhang, H., et al., A physically-based constitutive modelling of a high strength aluminum alloy at hot working conditions. *Journal of Alloys and Compounds*, 2018. 743: p. 283-293.

[84]   Lu, Z., et al., Artificial neural network prediction to the hot compressive deformation behavior of Al–Cu–Mg–Ag heat-resistant aluminum alloy. *Mechanics Research Communications*, 2011. 38(3): p. 192-197.

[85]   Lin, Y.C., J. Zhang, and J. Zhong, Application of neural networks to predict the elevated temperature flow behavior of a low alloy steel. *Computational Materials Science*, 2008. 43(4): p. 752-758.

[86]   Quan, G., et al., A characterization for the flow behavior of 42CrMo steel. *Computational Materials Science*, 2010. 50(1): p. 167-171.

[87]   Sheikh, H. and S. Serajzadeh, Estimation of flow stress behavior of AA5083 using artificial neural networks with regard to dynamic strain ageing effect. *Journal of Materials Processing Technology*, 2008. 196(1-3): p. 115-119.

[88]   Toros, S. and F. Ozturk, Flow curve prediction of Al–Mg alloys under warm forming conditions at various strain rates by ANN. *Applied Soft Computing*, 2011. 11(2): p. 1891-1898.

[89]   Langford, W., S. Snyder, and J. Bausch, New Criteria for Predicting the Press Performance of Deep Drawing Steels. *Transaction of American Society Metals*, 1950. 42: p. 1197-1232.

[90]   Banabic, D. and S. Wagner, Anisotropic behaviour of aluminium alloys sheets. *Aluminium*, 2002. 78(10): p. 926-930.

[91]   Hill, R., A theory of the yielding and plastic flow of anisotropic metals. *Proceedings of the Royal Society of London. Series A, Mathematical and Physical*, 1948. 193(1033): p. 281-297.

[92]   Chen, Z. and X. Dong, The GTN damage model based on Hill'48 anisotropic yield criterion and its application in sheet metal forming. *Computational Materials Science*, 2009. 44(3): p. 1013-1021.

[93]   Woodthorpe, J. and R. Pearce, The anomalous behaviour of aluminium sheet under balanced biaxial tension. *International Journal of Mechanical Sciences*, 1970. 12(4): p. 341-347.

[94]   Banabic, D. Determination of yield loci cross tensile tests assuming various kinds of yield criteria. in: *proceedings of the 20th Biennial [IDDRG] Congress*. Belgium. 2000.

[95]   Banabic, D., An improved analytical description of orthotropy in metallic sheets. *International Journal of Plasticity*, 2005. 21(3): p. 493-512.

[96]   Banabic, D., Plastic behaviour of sheet metal, in *Sheet Metal Forming Processes*. 2010, Springer. p. 27-140.

[97]   Ahmadi, S., A.R. Eivani, and A. Akbarzadeh, An experimental and theoretical study on the prediction of forming limit diagrams using new BBC yield criteria and M–K analysis. *Computational Materials Science*, 2009. 44(4): p. 1272-1280.

[98]   Izadpanah, S., S.H. Ghaderi, and M. Gerdooei, Material parameters identification procedure for BBC2003 yield criterion and earing prediction in deep drawing. *International Journal of Mechanical Sciences*, 2016. 115-116: p. 552-563.

[99]   Banabic, D. and K. Siegert, Anisotropy and formability of AA5182-0 aluminium alloy sheets. *CIRP Annals*, 2004. 53(1): p. 219-222.

[100]   Oyane, M., Criteria of Ductile Fracture Strain. *Bulletin of JSME*, 1972. 15(90): p. 1507-1513.

[101]   McClintock, F.A., A criterion for ductile fracture by the growth of holes. *Journal of applied mechanics*, 1968. 35(2): p. 363-371.

[102]   Rice, J.R. and D.M. Tracey, On the ductile enlargement of voids in triaxial stress fields. *Journal of the Mechanics and Physics of Solids*, 1969. 17(3): p. 201-217.

[103]   Gurson, A.L., Continuum theory of ductile rupture by void nucleation and growth: Part I—Yield criteria and flow rules for porous ductile media. *Journal of engineering materials and technology*, 1977. 99(1): p. 2-15.

[104]   Oyane, M., et al., Criteria for ductile fracture and their applications. *Journal of Mechanical Working Technology*, 1980. 4(1): p. 65-81.

[105]   Chaboche, J.L., M. Boudifa, and K. Saanouni, A CDM Approach of Ductile Damage with Plastic Compressibility. *International Journal of Fracture*, 2006. 137(1): p. 51-75.

[106]   Tvergaard, V. and A. Needleman, Analysis of the cup-cone fracture in a round tensile bar. *Acta metallurgica*, 1984. 32(1): p. 157-169.

[107]   Pardoen, T. and J. Hutchinson, An extended model for void growth and coalescence. *Journal of the Mechanics and Physics of Solids*, 2000. 48(12): p. 2467-2512.

[108]   Benzerga, A., J. Besson, and A. Pineau, Anisotropic ductile fracture: Part I: experiments. *Acta Materialia*, 2004. 52(15): p. 4623-4638.

[109]   Nahshon, K. and J. Hutchinson, Modification of the Gurson model for shear failure. *European Journal of Mechanics-A/Solids*, 2008. 27(1): p. 1-17.

[110]   Cockcroft, M. and D. Latham, Ductility and the workability of metals. *Journal of the Institute of Metals*, 1968. 96(1): p. 33-39.

[111]   Karafillis, A.P. and M.C. Boyce, A general anisotropic yield criterion using bounds and a transformation weighting tensor. *Journal of the Mechanics and Physics of Solids*, 1993. 41(12): p. 1859-1886.

[112]   Wierzbicki, T., et al., Calibration and evaluation of seven fracture models. *International Journal of Mechanical Sciences*, 2005. 47(4): p. 719-743.

[113]   Bai, Y. and T. Wierzbicki, Application of extended Mohr–Coulomb criterion to ductile fracture. *International Journal of Fracture*, 2010. 161(1): p. 1.

[114]   Wierzbicki, T. and L. Xue, On the effect of the third invariant of the stress deviator on ductile fracture. *Impact and Crashworthiness Laboratory, Technical Report*, 2005. 136.

[115]   Bao, Y. and T. Wierzbicki, On fracture locus in the equivalent strain and stress triaxiality space. *International Journal of Mechanical Sciences*, 2004. 46(1): p. 81-98.

[116]   Palchik, V., Application of Mohr–Coulomb failure theory to very porous sandy shales. *International Journal of Rock Mechanics and Mining Sciences*, 2006. 7(43): p. 1153-1162.

[117]   Luo, M., M. Dunand, and D. Mohr, Experiments and modeling of anisotropic aluminum extrusions under multi-axial loading – Part II: Ductile fracture. *International Journal of Plasticity*, 2012. 32-33: p. 36-58.

[118]   Papasidero, J., V. Doquet, and D. Mohr, Determination of the Effect of Stress State on the Onset of Ductile Fracture Through Tension-Torsion Experiments. *Experimental Mechanics*, 2013. 54(2): p. 137-151.

[119]   Sjöberg, T., J. Kajberg, and M. Oldenburg, Fracture behaviour of Alloy 718 at high strain rates, elevated temperatures, and various stress triaxialities. *Engineering Fracture Mechanics*, 2017. 178: p. 231-242.

[120]   Valoppi, B., S. Bruschi, and A. Ghiotti, Modelling of Fracture Onset in Ti6Al4V Sheets Deformed at Elevated Temperature. *Procedia Manufacturing*, 2016. 5: p. 248-258.

[121]   Clausen, A.H., et al., Flow and fracture characteristics of aluminium alloy AA5083–H116 as function of strain rate, temperature and triaxiality. *Materials Science and Engineering: A*, 2004. 364(1): p. 260-272.

[122]   Valoppi, B., et al., Johnson-Cook based criterion incorporating stress triaxiality and deviatoric effect for predicting elevated temperature ductility of titanium alloy sheets. *International Journal of Mechanical Sciences*, 2017. 123: p. 94-105.

[123] Novella, M.F., et al., Ductile damage modeling at elevated temperature applied to the cross wedge rolling of AA6082-T6 bars. *Journal of Materials Processing Technology*, 2015. 222: p. 259-267.

[124] Khan, A.S. and H. Liu, Strain rate and temperature dependent fracture criteria for isotropic and anisotropic metals. *International Journal of Plasticity*, 2012. 37: p. 1-15.

[125] Zhu, Y., et al., A new methodology for prediction of fracture initiation in hot compression of Ti40 titanium alloy. *Materials Science and Engineering: A*, 2012. 553: p. 112-118.

[126] Lemaitre, J., Local approach of fracture. *Engineering Fracture Mechanics*, 1986. 25(5): p. 523-537.

[127] Cao, T.S., et al., A Lode-dependent enhanced Lemaitre model for ductile fracture prediction at low stress triaxiality. *Engineering Fracture Mechanics*, 2014. 124-125: p. 80-96.

[128] Lian, J., Y. Feng, and S. Münstermann, A Modified Lemaitre Damage Model Phenomenologically Accounting for the Lode Angle Effect on Ductile Fracture. *Procedia Materials Science*, 2014. 3: p. 1841-1847.

[129] Naka, T. and F. Yoshida, Deep drawability of type 5083 aluminium–magnesium alloy sheet under various conditions of temperature and forming speed. *Journal of Materials Processing Technology*, 1999. 89-90: p. 19-23.

[130] Ayres, R.A., Alloying aluminum with magnesium for ductility at warm temperatures (25 to 250 C). *Metallurgical Transactions A*, 1979. 10(7): p. 849-854.

[131] Ayres, R.A. and M.L. Wenner, Strain and strain-rate hardening effects in punch stretching of 5182-0 aluminum at elevated temperatures. *Metallurgical Transactions A*, 1979. 10(1): p. 41-46.

[132] Naka, T., et al., The effects of temperature and forming speed on the forming limit diagram for type 5083 aluminum–magnesium alloy sheet. *Journal of Materials Processing Technology*, 2001. 113(1): p. 648-653.

[133] Verma, R., et al., Grain refinement and superplasticity in 5083 Al. *Materials Science and Engineering: A*, 1995. 191(1-2): p. 143-150.

[134] Friedman, P. and A. Ghosh, Microstructural evolution and superplastic deformation behavior of fine grain 5083Al. *Metallurgical and Materials Transactions A*, 1996. 27(12): p. 3827-3839.

[135] Verma, R., et al., Characterization of superplastic deformation behavior of a fine grain 5083 Al alloy sheet. *Metallurgical and Materials Transactions A*, 1996. 27(7): p. 1889-1898.

[136] Martin, C., J. Blandin, and L. Salvo, Variations in microstructure and texture during high temperature deformation of Al–Mg alloy. *Materials Science and Engineering: A*, 2001. 297(1-2): p. 212-222.

[137] McNelley, T.R., et al., Characteristics of the Transition from Grain-Boundary Sliding to Solute Drag Creep in Superplastic AA5083. *Metallurgical and Materials Transactions A*, 2007. 39(1): p. 50-64.

[138] Singh, D., et al., Effect of initial grain size on microstructure and mechanical behavior of cryorolled AA 5083. *Materials Today: Proceedings*, 2017. 4(8): p. 7609-7617.

[139] Cho, J., et al., A study on the hot-deformation behavior and dynamic recrystallization of Al–5 wt.% Mg alloy. *Journal of Materials Processing Technology*, 2001. 118(1-3): p. 356-361.

[140] Hosseinipour, S.J., An investigation into hot deformation of aluminum alloy 5083. *Materials & Design*, 2009. 30(2): p. 319-322.

[141] Meng, G., et al., Hot deformation and processing maps of an Al–5.7wt.%Mg alloy with erbium. *Materials Science and Engineering: A*, 2009. 517(1-2): p. 132-137.

[142] Mostafaei, M.A. and M. Kazeminezhad, Hot deformation behavior of hot extruded Al–6Mg alloy. *Materials Science and Engineering: A*, 2012. 535: p. 216-221.

[143] Senthilkumar, V., A. Balaji, and R. Narayanasamy, Analysis of hot deformation behavior of Al 5083–TiC nanocomposite using constitutive and dynamic material models. *Materials & Design*, 2012. 37: p. 102-110.

[144] Varela, F., et al., The harmonic method: A new procedure to obtain wall periodic cross response factors. *International Journal of Thermal Sciences*, 2012. 58: p. 20-28.

[145] Alizadeh, R., et al., Microstructural evolution and superplasticity in an Mg–Gd–Y–Zr alloy after processing by different SPD techniques. *Materials Science and Engineering: A*, 2017. 682: p. 577-585.

[146] Peirs, J., P. Verleysen, and J. Degrieck, Novel Technique for Static and Dynamic Shear Testing of Ti6Al4V Sheet. *Experimental Mechanics*, 2012. 52(7): p. 729-741.

[147] Liu, X.Y., et al., Flow behavior and microstructural evolution of Al–Cu–Mg–Ag alloy during hot compression deformation. *Materials Science and Engineering: A*, 2009. 500(1): p. 150-154.

[148] Liu, W., et al., Hot deformation behavior of AA7085 aluminum alloy during isothermal compression at elevated temperature. *Materials Science and Engineering: A*, 2014. 596: p. 176-182.

[149] Yang, Q., et al., Hot deformation behavior and microstructure of AA2195 alloy under plane strain compression. *Materials Characterization*, 2017. 131: p. 500-507.

[150] Driver, J. and O. Engler, Design of aluminum rolling processes for foil, sheet, and plate. *Materials Engineering*, 2004. 24: p. 69-114.

[151] Naka, T., et al., Effects of temperature on yield locus for 5083 aluminum alloy sheet. *Journal of Materials Processing Technology*, 2003. 140(1-3): p. 494-499.

[152] Aksenov, S.A., A.V. Kolesnikov, and A.V. Mikhaylovskaya, Design of a gas forming technology using the material constants obtained by tensile and free bulging testing. *Journal of Materials Processing Technology*, 2016. 237: p. 88-95.

[153] Abedini, A., C. Butcher, and M.J. Worswick, Fracture Characterization of Rolled Sheet Alloys in Shear Loading: Studies of Specimen Geometry, Anisotropy, and Rate Sensitivity. *Experimental Mechanics*, 2017. 57(1): p. 75-88.

[154] Majzoobi, G.H., et al., Damage characterization of aluminum 2024 thin sheet for different stress triaxialities. *Archives of Civil and Mechanical Engineering*, 2018. 18(3): p. 702-712.

[155] Gao, X., et al., On stress-state dependent plasticity modeling: Significance of the hydrostatic stress, the third invariant of stress deviator and the non-associated flow rule. *International Journal of Plasticity*, 2011. 27(2): p. 217-231.

[156] Li, Y., et al., Mixed mode stable tearing of thin sheet AI 6061-T6 specimens: experimental measurements and finite element simulations using a modified Mohr-Coulomb fracture criterion. *International Journal of Fracture*, 2010. 168(1): p. 53-71.

[157] Kang, J., et al., Hot Deformation Characteristics of 304 Stainless Steels by Tensile Test. *International Journal of Applied Engineering Research*, 2017. 12(22): p. 12415-12420.

[158] Taleff, E.M., et al., Warm-temperature tensile ductility in Al− Mg alloys. *Metallurgical and Materials Transactions A*, 1998. 29(13): p. 1081-1091.

[159] Chen, G., et al., Application of genetic algorithms for optimizing the Johnson–Cook constitutive model parameters when simulating the titanium alloy Ti-6Al-4V machining process. *Proceedings of the Institution of Mechanical Engineers, Part B: Journal of Engineering Manufacture*, 2012. 226(8): p. 1287-1297.

[160] Nazzal, M.A., M.K. Khraisheh, and B.M. Darras, Finite element modeling and optimization of superplastic forming using variable strain rate approach. *Journal of Materials Engineering and Performance*, 2004. 13(6): p. 691-699.

[161] Taleff, E.M., et al., Material Models for Simulation of Superplastic Mg Alloy Sheet Forming. *Journal of Materials Engineering and Performance*, 2010. 19(4): p. 488-494.

[162] de Souza Neto, E.A., D. Peric, and D.R. Owen, *Computational methods for plasticity: theory and applications*. 2011: John Wiley & Sons.

[163] Choung, J., et al., Failure strain formulation via average stress triaxiality of an EH36 high strength steel. *Ocean Engineering*, 2014. 91: p. 218-226.

[164] Bai, Y. and T. Wierzbicki, A new model of metal plasticity and fracture with pressure and Lode dependence. *International Journal of Plasticity*, 2008. 24(6): p. 1071-1096.

[165] Li, Y., et al., Prediction of shear-induced fracture in sheet metal forming. *Journal of Materials Processing Technology*, 2010. 210(14): p. 1858-1869.

[166] Johnson, G.R. and W.H. Cook, Fracture characteristics of three metals subjected to various strains, strain rates, temperatures and pressures. *Engineering Fracture Mechanics*, 1985. 21(1): p. 31-48.

[167] Bellet, M. Modélisation numérique du formage superplastique de tôles. *Phd thesis*. École Nationale Supérieure des Mines de Paris. 1988.

[168] Robert, C. Contribution à la simulation numérique des procédés de mise en forme-Application au formage incrémental et au formage superplastique. *PhD thesis* Arts et Métiers ParisTech. 2009.

[169]   Martinez, N.O. Optimization of superplastic forming production of Al-5083-SPF parts via finite element analysis. *PhD thesis*. Mondragon University. 2012.

[170]   Jarrar, F.S., et al., New approach to gas pressure profile prediction for high temperature AA5083 sheet forming. *Journal of Materials Processing Technology*, 2010. 210(6): p. 825-834.

[171]   Yang, J. Étude expérimentale et modélisation du formage superplastiqued'un alliage d'aluminium Al7475. *PhD thesis*. Arts et Métiers ParisTech. 2014.

MISE EN FORME A CHAUD DE TOLES FINES EN ALLIAGE AA5383 : APPROCHES EXPERIMENTALES ET NUMERIQUES

RESUME : Les alliages d'aluminium ont été largement utilisés dans l'industrie automobile et maritimes en raison des avantages d'une faible densité, d'une bonne résistance à la corrosion. Les travaux présentés dans ce mémoire de thèse s'intéressent à la mise en forme à chaud de tôles minces en alliage d'aluminium AA5383. L'objectif principal est de réduire le temps de formage sans sacrifier l'intégrité de la pièce. Tout d'abord, le comportement à la déformation à chaud de l'alliage AA5383 est caractérisé expérimentalement. Une campagne expérimentale comprenant d'essais de traction uniaxiale, de traction entaillées, de cisaillement et de gonflement libre est réalisée pour couvrir une plage importante de températures (623~723 K) et de vitesses de déformation (10^{-4}~10^{-1} s^{-1}). Ensuite, les modèles de matériau, tels qu'une règle de flux composite avec le critère de plasticité BBC2003 et le critère de dommage Mohr Coulomb Modifié, sont développés et mis en œuvre dans ABAQUS à l'aide du sous-programme utilisateur. Enfin, les simulations numériques des processus de formation de gaz sont effectuées et comparées aux résultats expérimentaux correspondants.

Mots-clés : Alliage AA5383, comportement à haute température, critère de plasticité BBC2003, critère d'endommagement MMC, formation de gaz chaud

FORMING OF DEEP-PARTS IN AA5383 ALLOY: EXPERIMENTAL AND NUMERICAL APPROACH

ABSTRACT: Aluminum alloys have been extensively used in the automotive and marine industry due to the advantages of low density, high strength to weight ratio and good corrosion resistance. Major challenge of their application lies in the ability to form deep-drawing shapes. Superplastic Forming is widely used to produce this type of parts. However, high forming cycle time due to the low forming strain rate limits their wide application. The present dissertation focuses on hot forming strategies to produce deep drawing parts from AA5383 aluminum thin sheets. The main objective is to reduce the forming time without sacrificing the part integrity. Firstly, the hot deformation behavior of the AA5383 alloy is experimentally characterized. An experimental campaign, including uniaxial tension, notched tension, shear and free bulging tests, is performed to cover an important range of temperatures (623~723 K) and strain rates (10^{-4}~10^{-1} s^{-1}). Then, the material models, such as a composite flow rule with the BBC2003 anisotropic yield criterion and the modified Mohr-Coulomb damage criterion, are developed and implemented in ABAQUS by using user subroutine. Finally, the numerical simulations of the gas forming processes are performed and compared with the corresponding experimental results.

Keywords: AA5383 alloy, high temperature behavior, BBC 2003 yield function, MMC damage criterion, hot gas forming

Arts et Métiers Sciences et Technologies

HESAM UNIVERSITÉ